気象庁
Japan Meteorological Agency

CLIMATE CHANGE MONITORING REPORT 2023

June 2024

Published by the
Japan Meteorological Agency

3-6-9 Toranomon, Minato City, Tokyo 105-8431, Japan

E-mail iao-jma@met.kishou.go.jp

CLIMATE CHANGE MONITORING REPORT
2023

June 2024

JAPAN METEOROLOGICAL AGENCY

Preface

The Japan Meteorological Agency (JMA) has published annual summaries under the title *Climate Change Monitoring Report* since 1996. The content provides up-to-date information on climate change factors affecting societal and economic activity based on JMA's observation and monitoring of international atmospheric and oceanic conditions.

The year 2023 was unprecedentedly hot, yielding the highest annual global average temperature since records began. Extremely high temperatures were observed in many parts of the world, and record monthly and seasonal averages were reported by numerous countries. The annual average in Japan was also the highest ever recorded. In particular, record-high temperatures were observed in northern/eastern Japan and elsewhere from the second half of July to August. Studies reveal that global warming contributed to these levels.

The Intergovernmental Panel on Climate Change (IPCC) Sixth Assessment Report (AR6) emphasizes that the frequency and intensity of extreme weather events are already increasing, and are expected to rise further with every additional increment of global warming. Immediate response to climate change is required, with United Nations Secretary-General Guterres expressing a strong sense of urgency with the words, "The era of global boiling has arrived." Worldwide efforts to deal with climate change include the Paris Agreement (an international treaty aimed at reducing greenhouse gas emissions) and the Climate Change Adaptation Act (a Japanese domestic law aimed at enhancing and strengthening adaptation in response to the effects of climate change).

Following this background, JMA published a report titled *Climate Change in Japan 2020* in 2020 to share fundamental scientific expertise on climate change countermeasures in Japan, and contribute to the effective promotion of such countermeasures, in conjunction with Japan's Ministry of Education, Culture, Sports, Science and Technology (MEXT). The report covers climate change in Japan, including differences observed and projections for global average temperature changes as detailed in the RCP 2.6 and 8.5 scenarios (referred to as the "2°C and 4°C warming scenarios" in the report). An updated version titled *Climate Change in Japan 2025* is currently in production for publication in March 2025.

In contrast, this report focuses on changes observed to date based on the latest observational data. It is intended for reference in conjunction with *Climate Change in Japan 2020*, which comprehensively details related scientific findings. Additionally, JMA and MEXT provided climate prediction dataset developed by various organizations and its guidebook in December 2022. The compilation is designed for detailed assessment of climate change effects and promotion of climate change mitigation/adaptation in conjunction with appropriate understanding of scientific findings in the field.

The content provided here is intended to raise awareness of climate change, and is expected to be particularly useful to related organizations and stakeholders internationally for climate change response.

Takashi Mori

MORI Takashi
Director-General
Japan Meteorological Agency

Index

News

I Record-high temperatures in Japan from mid-July to August 2023

○ The summer 2023 national average temperature in Japan was unprecedentedly high. In particular, record-highs were observed in northern/eastern Japan and elsewhere from mid-July onward. The average temperature for northern Japan in late July was the highest for the region since 1946, and that for eastern Japan was the second highest. The average temperature for the Sea of Japan side of eastern and western Japan in early August was also the highest ever.

○ These high temperatures in the second half of July are primarily attributed to active cumulus convection including typhoons near the Philippines, which caused the upper-level subtropical jet stream (STJ) to shift significantly northward and a warm anticyclone to cover Japan, and to a record strengthening in the extension of the low-level North Pacific Subtropical High toward the country. In addition to the STJ shift, typhoons Khanun and Lan continued to bring southerly warm, moist air to Japan in the first half of August, and the influence of Foehn phenomena added to the record-high temperatures on the Sea of Japan side.

I.1 Climate conditions

From mid-July to August 2023, the North Pacific Subtropical High extended to Japan's main island of Honshu, resulting in record-high temperatures in northern Japan and elsewhere (Figure I.1). The average temperature anomaly in late July was +3.9°C in northern Japan, making it the highest since 1946, and that in eastern Japan was +1.9°C, which was the second highest. In early August the North Pacific Subtropical High retreated east of Japan, but warm humid air continued to flow along the edge of the high-pressure area with the slow-moving typhoons Khanun and Lan. As a result, temperatures remained significantly higher than normal in northern Japan and on the Sea of Japan side of eastern and western Japan. Due to the influence of Foehn phenomena caused by inflows of moist air from the south, a temperature of 40.0°C was observed in Komatsu in Ishikawa Prefecture on August 10. Temperatures did not drop at night, and the daily minimum temperature in Itoigawa in Niigata Prefecture on August 10 was a nationwide record-high 31.4°C. These two prefectures are located on the Sea of Japan side, on the leeward side of mountain ranges. Average temperature anomalies in early August were significantly high in northern, eastern and western Japan, with those on the Sea of Japan sides of eastern and western Japan reaching +3.4 and +2.1°C, respectively – again the highest since 1946. In Tokyo there were 13 extremely hot days (daily-maximum temperatures higher than 35°C) in July, significantly exceeding the 7 days of 2001, and the highest number ever observed in July.

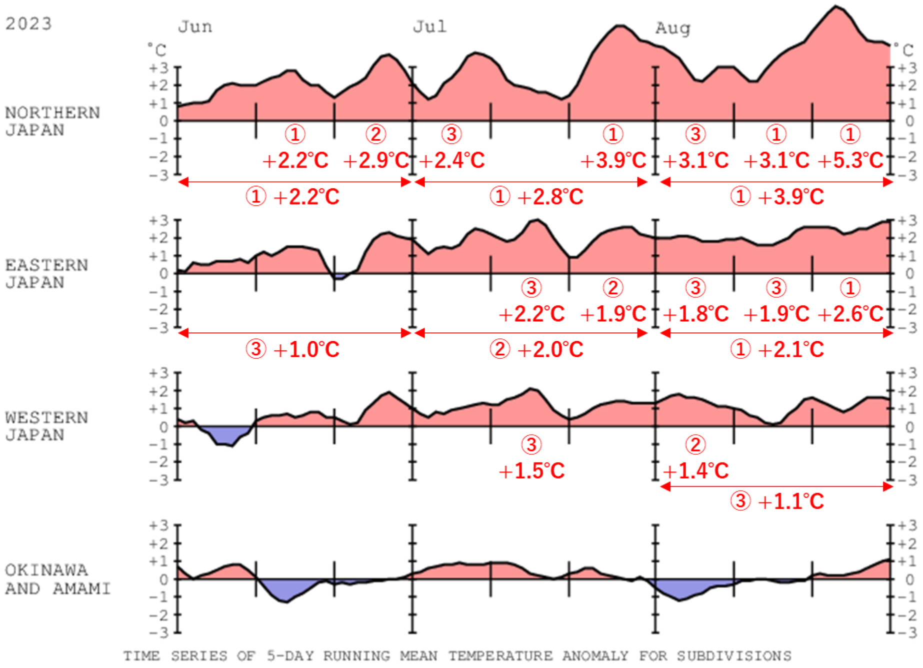

Figure I.1 Time-series representations of 5-day running mean temperature anomalies [°C] in northern, eastern and western Japan and Okinawa/Amami for June – August 2023

The base period for the normal is 1991 – 2020. The red circled numbers and values indicate rankings from the highest average temperatures since 1946 and anomalies for each month and ten-day period (up to the top three).

I.2 Characteristics of large-scale atmospheric circulation

The Japan Meteorological Agency (JMA), in conjunction with the Tokyo Climate Center Advisory Panel on Extreme Climatic Events (a JMA body staffed by prominent academics and researchers in the field of climate science), investigated and summarized factors considered to have contributed to the record-high temperatures as described below.

The high temperatures observed in the second half of July are primarily attributed to active cumulus convection including typhoons near the Philippines (Figure I.2 (a)), which caused the upper-level subtropical jet stream (STJ) to shift northward and a warm anticyclone to cover Japan (known as the Pacific – Japan (PJ) pattern), and to a Japan-record strengthening in the extension of the low-level North Pacific Subtropical High toward the country (Figure I.2 (b)). These conditions may be attributable to weaker-than-normal cumulus convective activity over the tropical Indian Ocean due to the La Niña event that ended in winter 2022/2023. The northward shift of the STJ near Japan may also have been associated with the meandering of the jet stream over Europe and the Mediterranean.

In addition to the pronounced northward shift of the STJ, typhoons Khanun and Lan continued to bring southerly warm moist air to Japan in the first half of August (Figure I.3 (a)), and the influence of Foehn phenomena added to the record-high temperatures on the Sea of Japan side (Figure I.3 (b)).

The high temperatures observed during summer are also attributed to a worldwide tendency of temperature increase associated with persistent global warming. The sea surface temperature (SST) around northern Japan also reached a record high, especially off the eastern coast, where the Kuroshio Extension was displaced far northward and temperatures remained remarkably high from the surface to the ocean interior. High SSTs hindered lower-atmosphere cooling in the northern part of the Sea of Japan and off the eastern coast, which may have contributed to the record-high temperatures in northern Japan.

The large-scale atmospheric circulation characteristics of the record-high temperatures are summarized in Figure I.4.

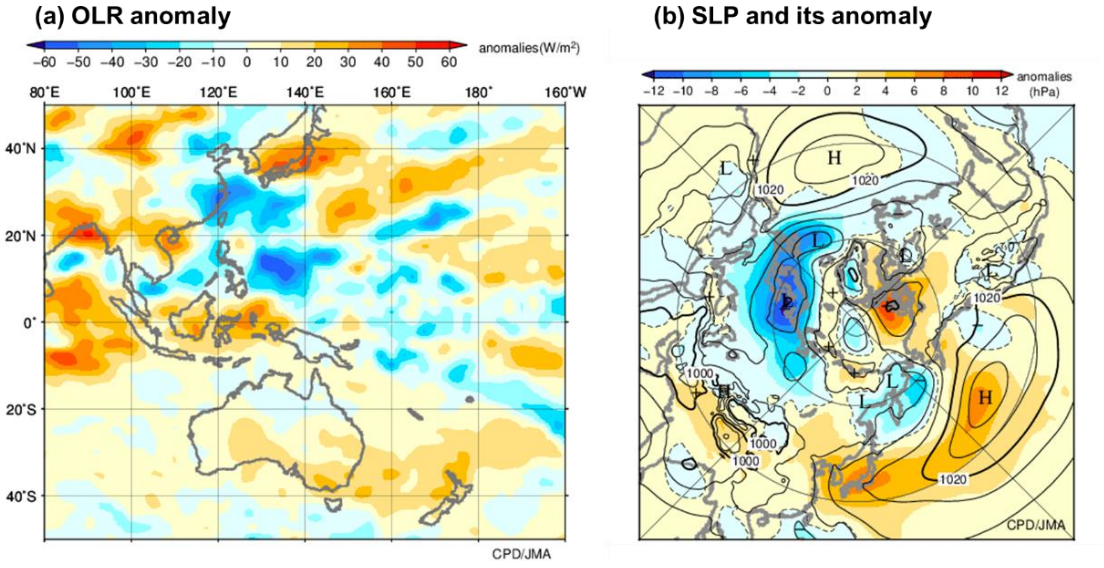
(a) OLR anomaly

(b) SLP and its anomaly

Figure I.2 (a) Outgoing longwave radiation (OLR) anomalies, and (b) sea level pressure (contours) and anomalies (shading) averaged for late July 2023

Units are (a) W/m^2 and (b) hPa. The base period for the normal is 1991 – 2020. (a) is based on the OLR dataset from the National Oceanic and Atmospheric Administration (NOAA), and (b) is based on the Japanese Reanalysis for Three Quarters of a Century (JRA-3Q) dataset.

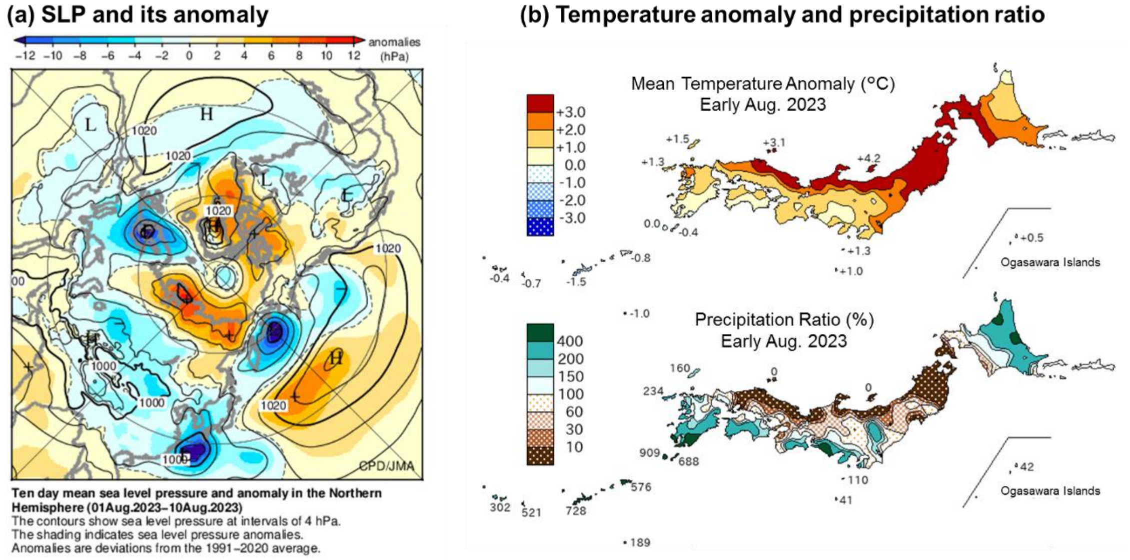
(a) SLP and its anomaly

(b) Temperature anomaly and precipitation ratio

Ten day mean sea level pressure and anomaly in the Northern Hemisphere (01Aug.2023–10Aug.2023)
The contours show sea level pressure at intervals of 4 hPa.
The shading indicates sea level pressure anomalies.
Anomalies are deviations from the 1991–2020 average.

Figure I.3 (a) sea level pressure (contours) and anomalies (shading), and (b) mean temperature anomalies and precipitation ratios averaged for early August 2023

Units are (a) hPa and (b) °C for temperature anomalies and % for precipitation ratios. The base period for the normal is 1991 – 2020. (a) is based on the Japanese Reanalysis for Three Quarters of a Century (JRA-3Q) dataset.

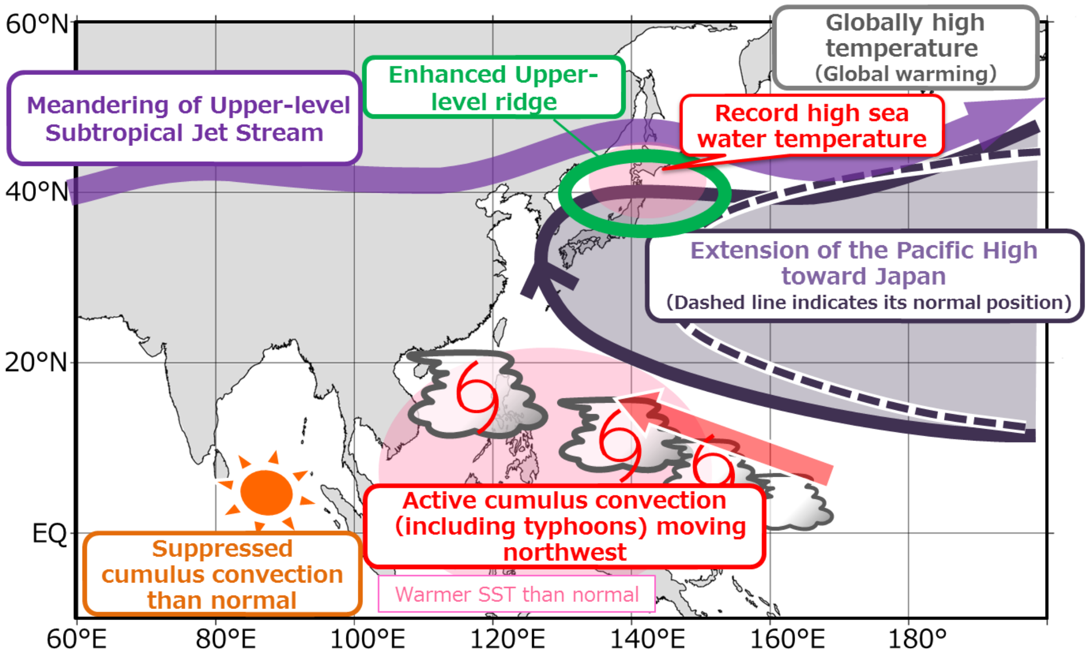

Figure I.4 **Characteristics of large-scale atmospheric circulation bringing extremely high temperatures in late July 2023**

II Record-high sea surface temperatures around Japan in 2023

○ Sea surface temperatures (SSTs) around Japan were above normal throughout 2023, and continued at record-high levels southeast of Hokkaido and east of Honshu. Annual mean SSTs around Japan were the highest since 1908.

The Japan Meteorological Agency (JMA) monitors global SSTs around Japan and elsewhere using observation data from satellites, ships, buoys and other sources. Values around Japan were above normal throughout 2023, with monthly means at their highest from August to December since 1982. The monthly SST anomaly around Japan was the highest for the year (+1.6°C) in September, with values exceeding +4°C southeast of Hokkaido and east of Honshu, and +3°C in the Sea of Japan (Figure II.1). SST anomalies in six of the ten monitoring areas were the highest for September since 1982 (Table II.1). Based on JMA's SST dataset compiled using over a century of in-situ observation data from sources such as ships and buoys, the annual mean SST anomaly in 2023 was +1.10°C, making it the highest since 1908 (Figure II.2 and Section 2.8).

A factor behind these record-highs was warm air coverage; the annual mean surface air temperature for the country in 2023 was the highest since 1898.

Warm subsurface waters associated with a northward shift of the Kuroshio Extension up to the area off the Sanriku region from spring onward also contributed to the record-high values east of Japan. JMA's Ryofu Maru research vessel observed subsurface water temperatures approximately +10°C higher than normal in July 2023 (Figure II.3 middle, right).

In addition, fewer tropical cyclone passages contributed to higher-than-normal SSTs around Japan, thereby lowering the effects of cooling SSTs.

Table II.1 Monthly mean SST anomalies (top) and rankings by month (bottom) for September 2023

Area numbers are as indicated in Figure II.1

Area	1	2	3	4	5	6	7	8	9	10
Anomaly (°C)	+2.5	+3.7	+2.7	+2.5	+1.8	+0.9	+0.8	+1.2	+0.7	+0.4
Ranking	1	1	1	1	1	3	3	1	6	8

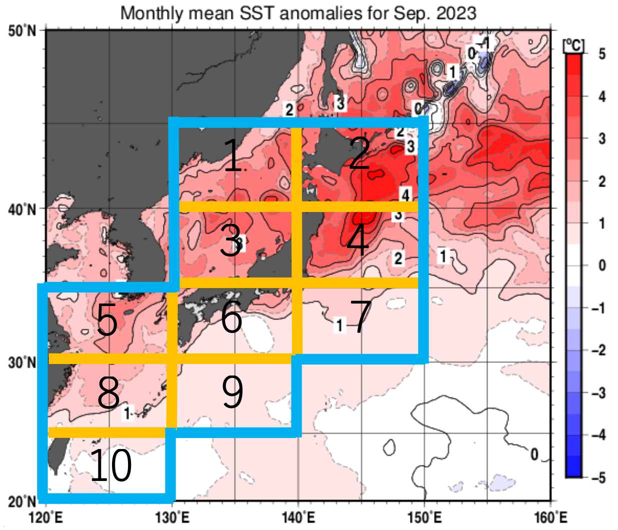

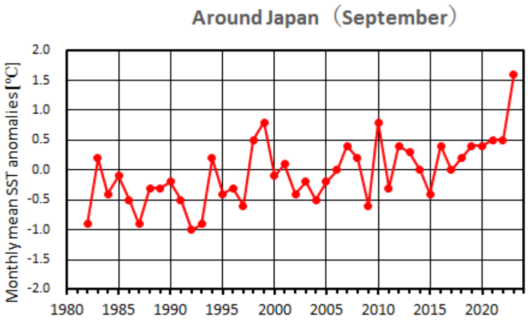

Figure Ⅱ.1 Distribution of monthly mean SST anomalies in September 2023 (left) and SST anomalies for September since 1982

The blue frame indicates areas defined as "around Japan." Normals are averages from 1991 to 2020.

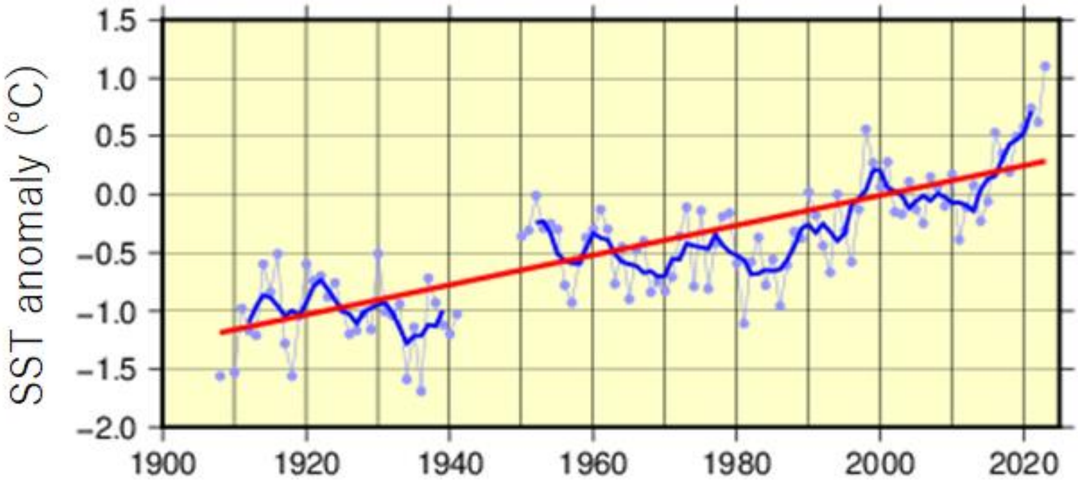

Figure Ⅱ.2 Annual mean SST anomalies from 1908 to 2023

The blue dots, blue lines and red line indicate annual anomalies, the five-year running mean and the long-term linear trend, respectively. Normals are averages from 1991 to 2020.

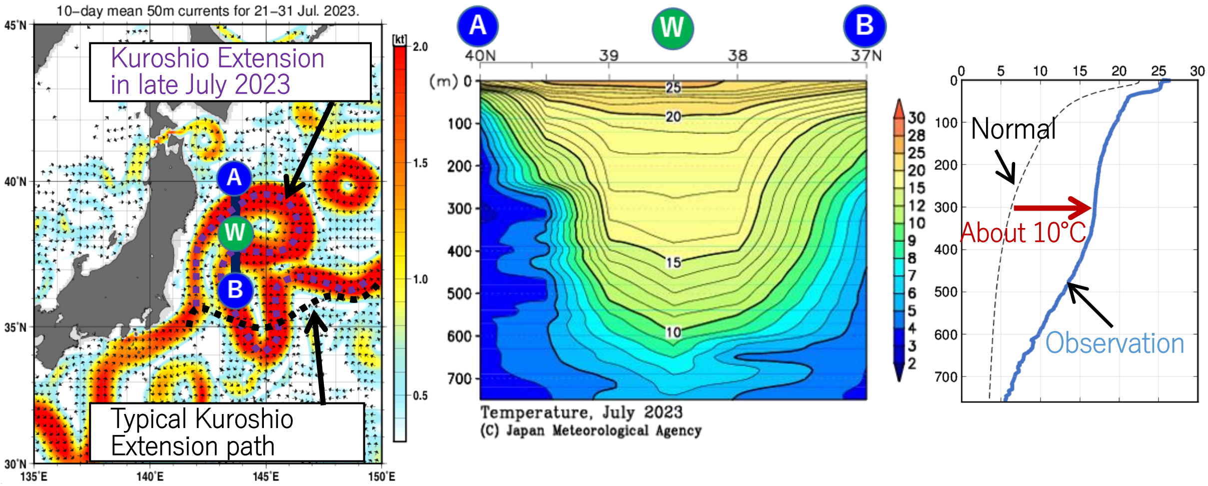

Figure Ⅱ.3 Left: 10-day mean 50 m currents for 21 – 31 July 2023 and JMA's Ryofu Maru research vessel observation line (A – B) in July 2023; middle: temperature distribution along A – B; right: observed and normal (1993 – 2017 mean) temperature profiles for Station W

Chapter 1 Climate in 2023

1.1 Global climate summary

○ Extremely high temperatures were frequently observed over wide areas of the world. Record monthly and seasonal mean temperatures were reported by various countries, and new national maximum temperatures were recorded in Vietnam, China and Brazil.

○ Disaster conditions resulting in extensive fatalities were caused by heavy rain in Libya in September and in the area from Somalia to Cameroon from March to May and from October to December, and by a cyclone in the area from Madagascar to Malawi from February to March.

Major extreme climate events[1] and weather-related disasters in 2023 are shown in Figure 1.1-1 and Table 1.1-1.

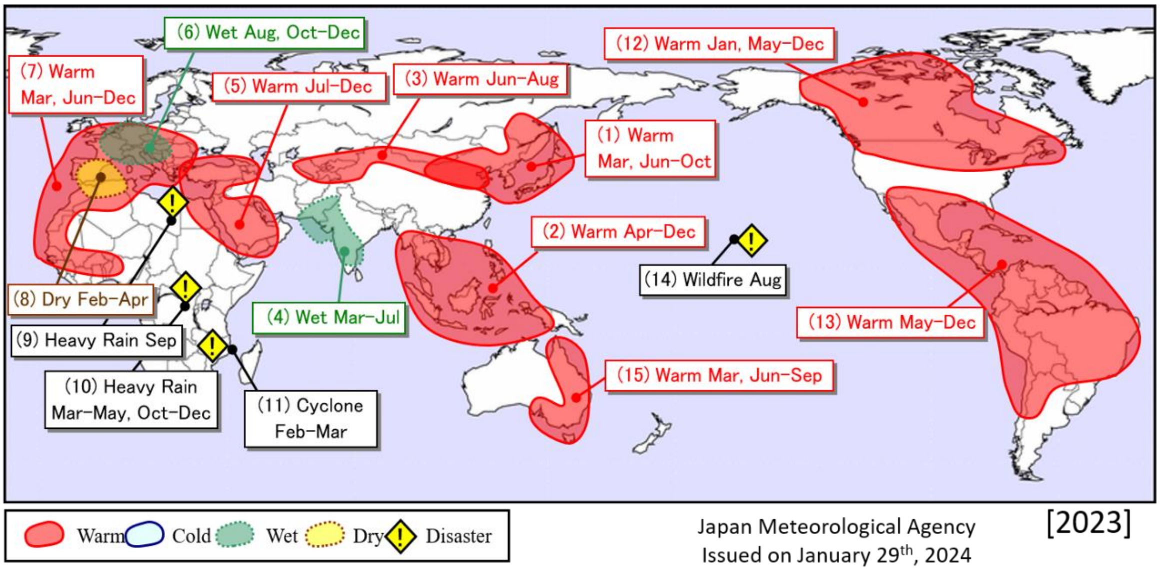

Figure 1.1-1 Major extreme events and weather-related disasters observed in 2023[2]
"Warm," "Cold," "Wet" and "Dry" indicate extreme climate events with particularly significant effects. JMA defines extreme events as phenomena likely to occur with a 30-year periodicity. Disaster effects are evaluated from EM-DAT information, United Nations reports and government data.
EM-DAT: The Emergency Events Database - Université Catholique de Louvain (UCL) - CRED, D. Guha-Sapir - www.emdat.be, Brussels, Belgium.

Extremely high temperatures ((1), (2), (3), (5), (7), (12), (13) and (15) in Figure 1.1-1) were frequently observed over wide areas of the world.

Extremely high temperatures were observed in and around eastern East Asia and in Southeast Asia, mostly from boreal spring to autumn ((1) and (2) in Figure 1.1-1). Record monthly and seasonal means were reported in Japan, Korea and China (sources: Japan Meteorological Agency, Korea Meteorological Administration, China Meteorological Administration). In northern Vietnam, a new national maximum of 44.2°C was recorded at Nghean on 7 May (source: Vietnam Meteorological and Hydrological Administration).

---

[1] Extreme climate events are defined by anomalies or ratios to climatological normals. Normals represent mean climate conditions at given sites, and are currently based on a 30-year mean covering the period from 1991-2020.

[2] Information on major extreme climatic events and weather-related disasters since 2008 is provided on JMA's website at https://www.data.jma.go.jp/tcc/tcc/products/climate/annual/index.html

Extremely high temperatures were observed in summer from eastern China to southern Central Asia ((3) in Figure 1.1-1). In China's Xinjiang province, a new national maximum of 52.2°C was recorded at Turpan on 16 July (source: China Meteorological Administration).

Extremely high temperatures were observed, mostly from July to December, in the area from Turkey to the Arabian Peninsula and from central Europe to Western Africa ((5) and (7) in Figure 1.1-1). Record-high monthly values were reported in Turkey, Bahrain and various European countries (sources: Turkish State Meteorological Service, Bahrain Meteorological Directorate, UK Met Office, State Meteorological Agency (Spain), Deutscher Wetterdienst (Germany), Meteo France).

Extremely high temperatures were observed, mostly from May to December, in the area from northern to central North America and from southern North America to central South America ((12) and (13) in Figure 1.1-1). In southeastern Brazil, a new national maximum of 44.8°C was recorded at Aracuai on 19 November (source: Instituto Nacional de Meteorologia, Brazil).

Extremely high temperatures were observed in March and from June to September in the area from northern to southeastern Australia ((15) in Figure 1.1-1). The seasonal mean winter temperature in the country (from June to August) was the highest on record since 1910 (Bureau of Meteorology, Australia).

Extremely high precipitation levels were observed from March to July in the area from central India to Pakistan ((4) in Figure 1.1-1). It was reported that heavy rain from June to August caused at least 1,010 fatalities in the area from Afghanistan to India (source: EM-DAT).

Extremely heavy rain was observed in central Europe in August and from October to December ((6) in Figure 1.1-1), and extremely low precipitation levels were observed from Spain to northern Algeria from February to April ((8) in Figure 1.1-1).

Immense damage was brought by heavy rain in Africa ((9) and (10) in Figure 1.1-1), with Storm Daniel causing more than 12,350 fatalities in Libya (source: EM-DAT). Heavy rain from March to May and from October to December caused more than 3,970 fatalities in the area from Somalia to Cameroon (sources: EM-DAT, OCHA). Cyclone Freddy caused at least 860 fatalities in the area from Madagascar to Malawi from February to March ((11) in Figure 1.1-1) (source: EM-DAT).

Hot, dry conditions also caused socio-economic damage. It was reported that wildfires in 2023 affected approximately 185,000 square kilometers in Canada – the largest yearly area since 1983 (source: Canadian Interagency Forest Fire Center Inc.). Wildfires in August caused at least 120 fatalities in Hawaii, USA ((14) in Figure 1.1-1) (source: EM-DAT).

Annual mean temperatures were above normal in most parts of the world, and were very high in the area from East Asia to Southeast Asia, from Central Asia to the northern part of Northern Africa, in northern North America, from eastern to southern North America, and in central South America (Figure 1.1-2).

Annual precipitation amounts were above normal from northwestern Central Asia to the Arabian Peninsula and from central to western Europe, and were below normal in southwestern Central Asia and from southwestern Europe to western Northern Africa (Figure 1.1-3).

Table 1.1-1 Major extreme climatic events and weather-related disasters worldwide in 2023

No.	Type	Period	Area
(1)	Warm	March, June-October	In and around eastern East Asia
(2)	Warm	April-December	Southeast Asia
(3)	Warm	June-August	From eastern China to southern Central Asia
(4)	Wet	March-July	From central India to Pakistan
(5)	Warm	July-December	From Turkey to the Arabian Peninsula
(6)	Wet	August, October-December	Central Europe
(7)	Warm	March, June-December	From central Europe to Western Africa
(8)	Dry	February-April	From Spain to northern Algeria
(9)	Heavy Rain	September	Libya
(10)	Heavy Rain	March-May, October-December	From Somalia to Cameroon
(11)	Cyclone	February-March	From Madagascar to Malawi
(12)	Warm	January, May-December	From northern to central North America
(13)	Warm	May-December	From southern North America to central South America
(14)	Wildfire	August	The state of Hawaii, USA
(15)	Warm	March, June-September	From northern to southeastern Australia

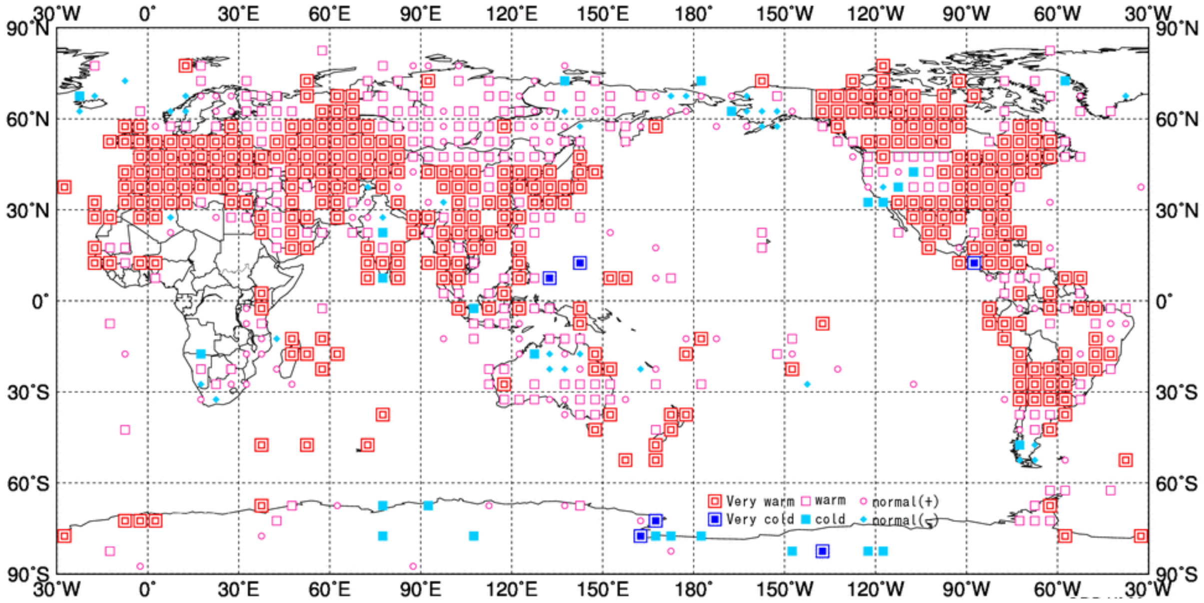

Figure 1.1-2 Normalized annual mean temperature anomalies for 2023[3]

Categories are defined by the annual mean temperature anomaly against the normal divided by its standard deviation and averaged in 5° × 5° grid boxes. Red/blue marks indicate values above/below the normal calculated for the period from 1991 to 2020. The thresholds of each category are –1.28, –0.44, 0, +0.44 and +1.28[4]. Land areas without graphics represent regions for which the observation data sample is insufficient or normal data are unavailable.

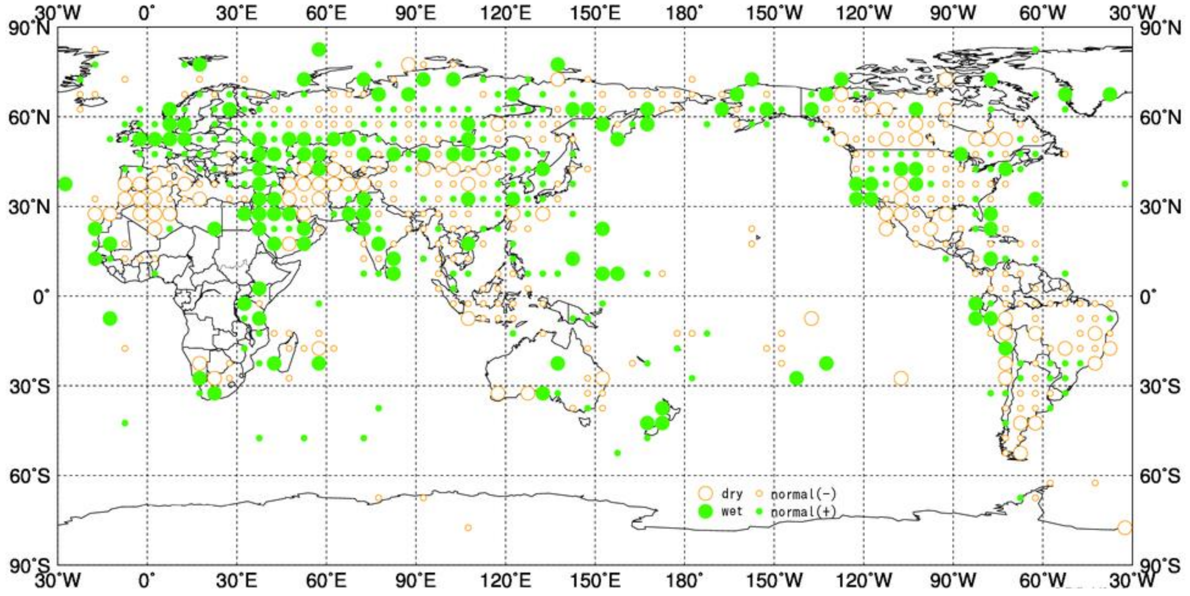

Figure 1.1-3 Annual total precipitation amount ratios for 2023[3]

Categories are defined by the annual precipitation ratio to the normal averaged in 5° × 5° grid boxes. Green/yellow marks indicate values above/below the thresholds. The thresholds of each category are 70, 100 and 120% of the normal calculated for the period from 1991 to 2020. Land areas without graphics represent regions for which the observation data sample is insufficient or normal data are unavailable.

---

[3] Normalized annual mean temperature anomalies and annual total precipitation amount ratios since 2008 are provided on JMA's website at https://www.data.jma.go.jp/tcc/tcc/products/climate/annual/index.html

[4] In normal distribution, values of 1.28 and 0.44 correspond to occurrence probabilities of less than 10 and 33.3%, respectively.

1.2 Climate in Japan[5]

- ○ Temperatures were above normal from spring to autumn (except for a few short spells with below-normal values), resulting in annual mean temperatures that were significantly above normal in northern, eastern and western Japan and above normal in Okinawa/Amami. Annual mean temperatures were the highest since 1946 in northern and eastern Japan, and tied with 1998 as the highest since 1946 in western Japan.
- ○ Autumn sunshine durations were significantly above normal and precipitation amounts were significantly below normal on the Pacific side of eastern and western Japan and in Okinawa/Amami, largely because the frequency of typhoons and other low-pressure systems affecting these regions was lower than normal. Sunshine durations on the Pacific side of western Japan were the highest and precipitation was the lowest for autumn.

1.2.1 Annual characteristics

The annual climate anomaly/ratio for Japan in 2023 is shown in Figure 1.2-1.

- ○ Annual mean temperatures were significantly above normal in northern, eastern and western Japan and above normal in Okinawa/Amami.
- ○ Annual precipitation amounts were above normal on the Sea of Japan side of northern Japan. Values were below normal on the Pacific side of northern and eastern Japan and in Okinawa/Amami.
- ○ Annual sunshine durations were significantly above normal on the Sea of Japan side of northern, eastern and western Japan and on the Pacific side of northern and eastern Japan, and above normal on the Pacific side of western Japan and in Okinawa/Amami.

---

[5] The term significantly above normal is used for cases in which observed mean temperatures or precipitation amounts exceed the 90th percentile for the base period (1991 – 2020), and significantly below normal is used when the corresponding figures fall below the 10th percentile.

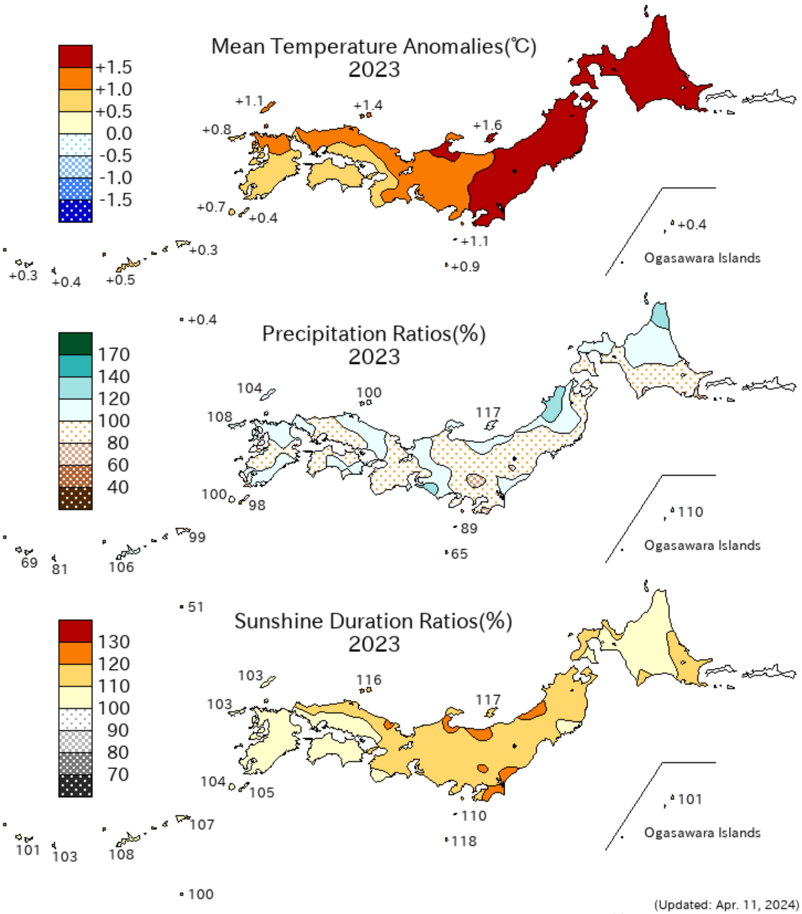

(Updated: Apr. 11, 2024)
All rights reserved. Copyright(c) Japan Meteorological Agency

Figure 1.2-1 Annual climate anomaly/ratio for Japan in 2023
The base period for the normal is 1991 – 2020.

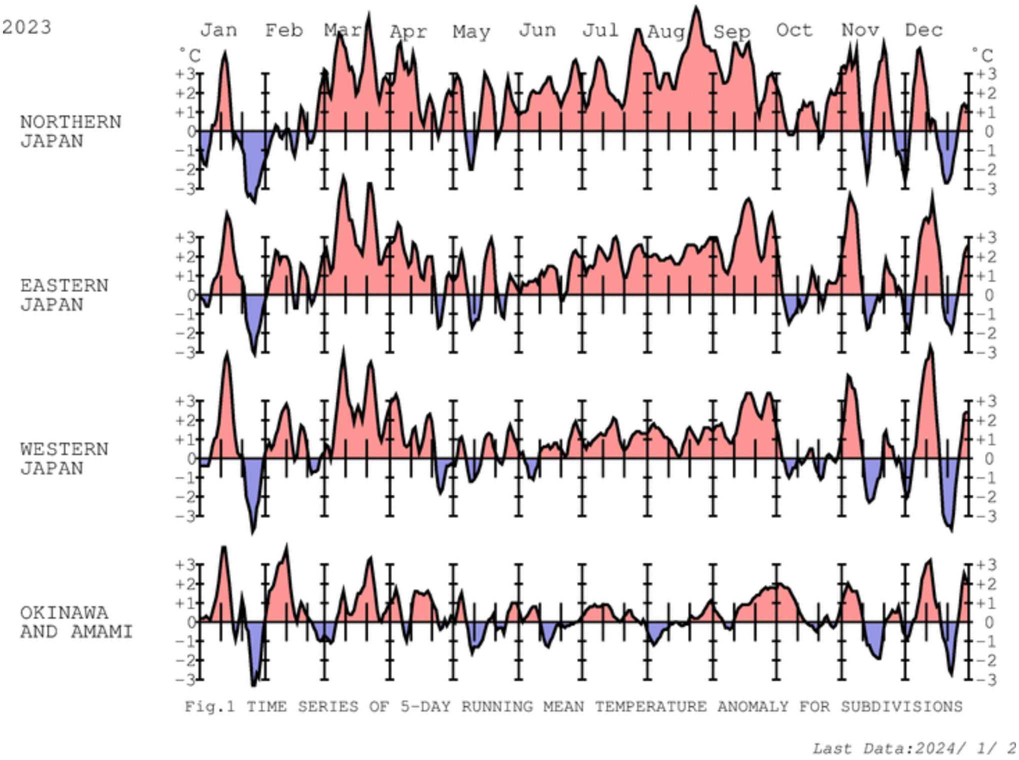

Figure 1.2-2 Five-day running mean temperature anomaly for subdivisions (January – December 2023)
The base period for the normal is 1991 – 2020.

1.2.2 Seasonal characteristics

Five-day running mean temperature anomalies for subdivisions (January – December 2023) are shown in Figure 1.2-2, and seasonal anomalies/ratios for Japan in 2023 are shown in Figure 1.2-3. Numbers of observatories reporting record of monthly mean temperatures, precipitation amounts and sunshine durations (2023) are shown in Table 1.2-1.

(1) Winter (December 2022 – February 2023)

- Seasonal mean temperatures were above normal in Okinawa/Amami. Values were below normal in northern Japan.
- Seasonal precipitation amounts were above normal on the Sea of Japan side of eastern Japan. Values were below normal on the Pacific side of northern, eastern and western Japan and on the Sea of Japan side of western Japan.
- Seasonal sunshine durations were above normal on the Sea of Japan side and the Pacific side of western Japan.

Periodic masses of cold air flowed in over the main islands of Japan, and further cold-air inflows caused below-normal seasonal mean temperatures in northern Japan. Seasonal precipitation amounts were above normal on the Sea of Japan side of eastern Japan, where northwest monsoon conditions brought more rain and snow. Seasonal mean temperatures were above normal in Okinawa/Amami, which was often covered by warm-air masses.

Seasonal precipitation amounts were below normal on the Pacific side of northern, eastern and western Japan and the Sea of Japan side of western Japan in association with reduced effects from low-pressure systems and fronts. High-pressure systems frequently covered the area around western Japan, causing above-normal seasonal sunshine durations on the Sea of Japan side and the Pacific side of western Japan.

(2) Spring (March – May 2023)

- Seasonal mean temperatures were significantly above normal in northern, eastern and western Japan and above normal in Okinawa/Amami.
- Seasonal precipitation amounts were significantly above normal on the Sea of Japan side of western Japan, and above normal on the Sea of Japan side of eastern Japan and the Pacific side of western Japan. Values were below normal in Okinawa/Amami.
- Seasonal sunshine durations were significantly above normal on the Sea of Japan side of northern and eastern Japan and above normal on the Sea of Japan side of western Japan, on the Pacific side of northern, eastern and western Japan, and in Okinawa/Amami.

Seasonal mean temperatures were significantly above normal in northern, eastern and western Japan and above normal in Okinawa/Amami in association with warm-air masses that frequently covered the country. Spring values for northern and eastern Japan were the highest since 1946.

Seasonal sunshine durations were above normal nationwide due to frequent high-pressure systems coverage. Values on the Sea of Japan side of eastern Japan tied with 2019 as the highest since 1946. Seasonal precipitation amounts were below normal in Okinawa/Amami in association with reduced effects from low-pressure systems and fronts. Low-pressure systems and fronts temporarily brought heavy rain to western Japan and the Sea of Japan side of eastern Japan, causing significantly above-normal seasonal precipitation on the

Sea of Japan side of western Japan, and above-normal seasonal precipitation on the Sea of Japan side of eastern Japan and on the Pacific side of western Japan.

(3) Summer (June – August 2023)

- Seasonal mean temperatures were significantly above normal in northern, eastern and western Japan.
- Seasonal precipitation amounts were above normal on the Pacific side of eastern and western Japan and in Okinawa/Amami. Values were below normal on the Pacific side of northern Japan.
- Seasonal sunshine durations were significantly above normal on the Sea of Japan side and the Pacific side of northern and eastern Japan, and below normal in Okinawa/Amami.

Seasonal mean temperatures were significantly above normal in northern, eastern and western Japan due to coverage by warm air and sub-tropical warm air inflows. Summer values for northern and eastern Japan were the highest since 1946, with values in western Japan tied with 2013, 2018 and 2022 for the same record.

High-pressure systems frequently covered northern and eastern Japan, causing significantly above-normal seasonal sunshine durations on the Sea of Japan side and the Pacific side of northern and eastern Japan. The Baiu front in June and typhoons Khanun (T2306) and Lan (T2307) in August brought above-normal seasonal precipitation to the Pacific side of eastern and western Japan and Okinawa/Amami. These also caused below-normal seasonal sunshine durations in Okinawa/Amami.

(4) Autumn (September – November 2023)

- Seasonal mean temperatures were significantly above normal in northern, eastern and western Japan and above normal in Okinawa/Amami.
- Seasonal precipitation amounts were significantly above normal on the Sea of Japan side of northern Japan and above normal on the Sea of Japan side of eastern Japan. Values were significantly below normal on the Pacific side of eastern and western Japan and in Okinawa/Amami and below normal on the Sea of Japan side of western Japan.
- Seasonal sunshine durations were significantly above normal on the Pacific side of eastern and western Japan, on the Sea of Japan side of western Japan and in Okinawa/Amami, and above normal on the Sea of Japan side of northern and eastern Japan and the Pacific side of northern Japan.

Seasonal mean temperatures were significantly above normal in northern, eastern and western Japan and above normal in Okinawa/Amami in association with warm-air masses that frequently covered the country. Autumn values for northern and eastern Japan were the highest since 1946.

Autumn seasonal precipitation amounts were the highest since 1946 on the Sea of Japan side of northern Japan and above normal on the Sea of Japan side of eastern Japan in association with low-pressure systems and cold air. Values were significantly below normal on the Pacific side of eastern and western Japan and in Okinawa/Amami, and below normal on the Sea of Japan side of western Japan due to a lower-than-normal frequency of low-pressure systems and typhoons. Autumn seasonal precipitation amounts were the lowest since 1946 on the Pacific side of western Japan.

Seasonal sunshine durations were significantly above normal on the Pacific side of eastern and western Japan, on the Sea of Japan side of western Japan and in Okinawa/Amami, and above normal on the Sea of Japan side of northern and eastern Japan and on the Pacific side of northern Japan in association with frequent high-pressure systems coverage. Values were the highest for autumn since 1946 on the Pacific side of eastern and western Japan and on the Sea of Japan side of western Japan.

(5) Early Winter (December 2023)

Monthly mean temperatures were significantly above normal in eastern Japan in association with reduced effects from cold air. Monthly precipitation amounts were above normal on the Sea of Japan side of eastern Japan in association with low-pressure systems and the winter monsoon in the second and third 10 days of the month. Values were below normal on the Sea of Japan side of northern and western Japan and on the Pacific side of northern and eastern Japan due to a weak influence from the winter monsoon on the former and low-pressure systems on the latter. Monthly sunshine durations were above normal on the Pacific side of eastern and western Japan in association with the winter monsoon and high-pressure systems. In Okinawa/Amami, monthly precipitation amounts were above normal and sunshine durations were below normal in association with low-pressure systems and cold-air inflow in the first and third 10 days of the month.

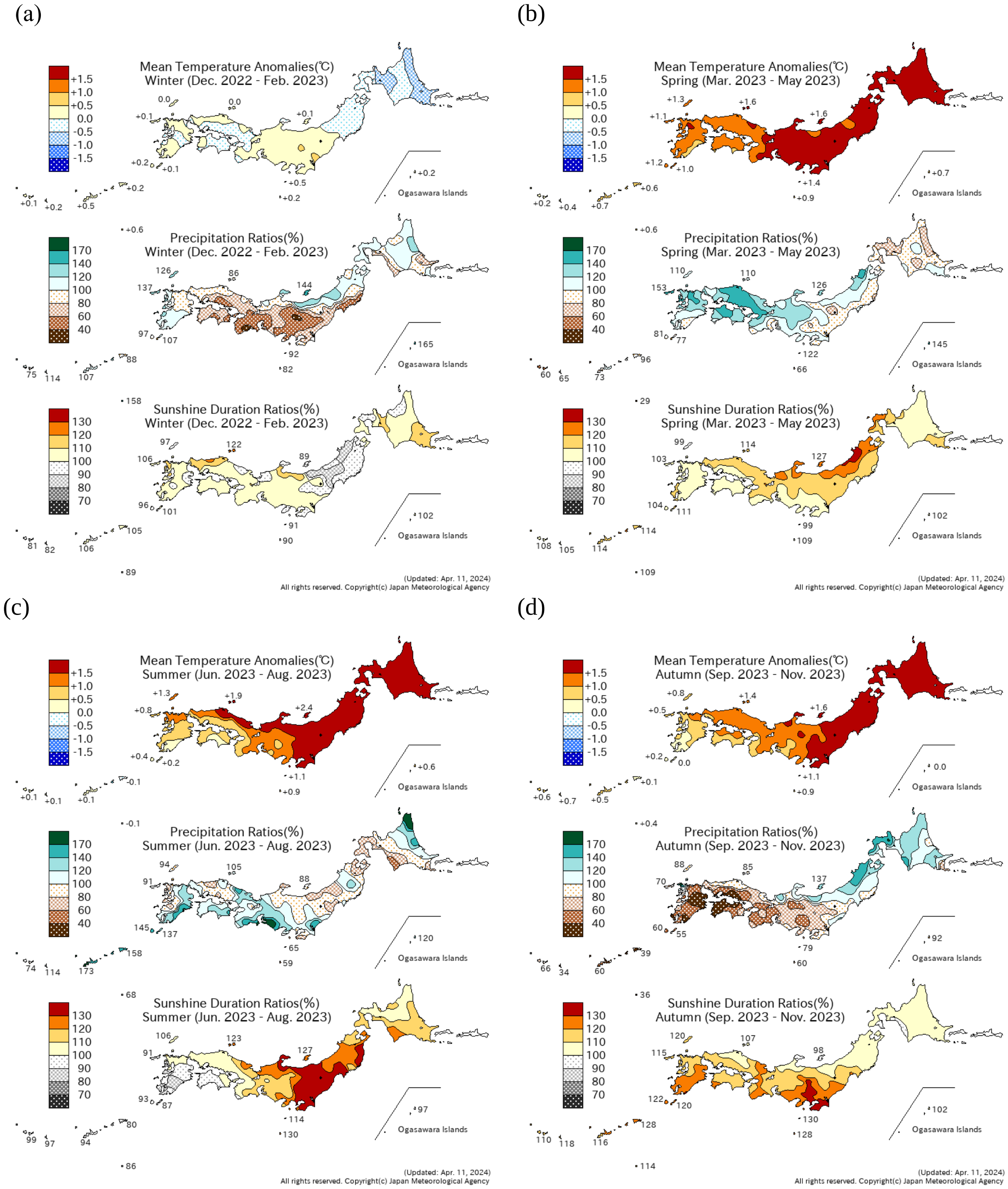

Figure 1.2-3 Seasonal anomalies/ratios for Japan in 2023

(a) Winter (December 2022 to February 2023), (b) spring (March to May 2023), (c) summer (June to August 2023), (d) autumn (September to November 2023). The base period for the normal is 1991 – 2020.

Table 1.2-1 Numbers of observatories reporting record (include tie record) of monthly mean temperatures, precipitation amounts and sunshine durations (2023)

From 153 surface meteorological stations across Japan.

	Temperature		Precipitation amount		Sunshine duration	
	Highest	Lowest	Heaviest	Lightest	Longest	Shortest
January				1	4	
February				2		
March	114			1	25	
April	13		1			
May				1		
June	27		1			
July	25			1	4	
August	70		4	3	2	
September	111			3	1	
October	5			2	9	
November	8		1	1	3	
December	2				4	

1.3 Atmospheric circulation and oceanographic conditions[6]

○ Following the La Niña event that began in boreal autumn 2021 and terminated in winter 2022/2023, an El Niño event occurred in boreal spring 2023 and developed through boreal autumn 2023. The influences of these events were seen in tropical atmospheric circulation. The positive phase of an Indian Ocean Dipole (IOD) event was observed from summer to autumn 2023.

○ Convective activity over the Asian summer monsoon region in 2023 was generally weaker than normal.

Monitoring of atmospheric and oceanographic conditions (e.g., upper air flow, tropical convective activity, sea surface temperatures (SSTs) and the Asian monsoon) is key to understanding the causes of extreme weather events[7]. This section briefly outlines the characteristics of atmospheric circulation and oceanographic conditions seen in 2023.

1.3.1 Characteristics of individual seasons[8]

(1) Winter (December 2022 – February 2023)

In the equatorial Pacific, significantly positive SST anomalies were observed in the western part and negative SST anomalies were seen from central to eastern parts (Figure 1.3-1 (a)) in association with La Niña conditions that persisted until boreal winter 2022/23.

Tropical convection was enhanced from the eastern Indian Ocean to Southeastern Asia, and was suppressed near the date line in the equatorial Pacific (Figure 1.3-1 (b)). In the upper troposphere, anti-cyclonic circulation anomalies were seen from South Asia to the south of Japan and cyclonic circulation anomalies straddling the equator were seen over the central tropical Pacific in association with suppressed convection (Figure 1.3-1 (c)). In the lower troposphere over the tropics, anti-cyclonic circulation anomalies straddling the equator were seen in the western to central Pacific and cyclonic circulation anomalies straddling the equator were seen from the Indian Ocean to Indonesia (Figure 1.3-1 (d)). It is suggested that these anomalies are partially attributable to La Niña conditions.

In the 500-hPa height field, the polar vortex in the Northern Hemisphere split, with positive anomalies over the polar region and negative anomalies from Eastern Siberia to northern East Asia. A wavy pattern was seen in height anomalies along the polar front jet over Eurasia (Figure 1.3-1 (e)). In the sea level pressure field, positive anomalies were seen over the north polar region. The Siberian High was stronger than normal over its central to western parts, and the Aleutian Low was stronger than normal over its northwestern part (Figure 1.3-1 (f)). Temperatures at 850 hPa were above normal over the north polar region and eastern North America, and were below normal from Central and Eastern Siberia to northern East Asia (Figure 1.3-1 (g)).

---

[6] See the Glossary for terms relating to sea surface temperature variations and monsoon.

[7] The main charts used for monitoring of atmospheric circulation and oceanographic conditions are: sea surface temperature (SST) maps representing SST distribution for monitoring of oceanographic variability elements such as El Niño/La Niña phenomena; outgoing longwave radiation (OLR) maps representing the strength of longwave radiation from the earth's surface under clear sky conditions into space or from the top of clouds under cloudy conditions into space for monitoring of convective activity; 850-hPa stream function maps representing air flow in the lower troposphere for monitoring of atmospheric circulation variability elements such as the Pacific High and the monsoon trough associated with the Asian summer monsoon; 500-hPa height maps representing air flow at a height of approximately 5,500 meters for monitoring of atmospheric circulation variability elements such as westerly jet streams and the Arctic Oscillation; sea level pressure maps representing air flow and pressure systems on the earth's surface for monitoring of the Pacific High, the Siberian High, the Arctic Oscillation and other phenomena; 850-hPa temperature maps representing air temperature at a height of approximately 1,500 meters; and temperature calculated from thickness in the troposphere for monitoring of mean temperature of the troposphere.

[8] JMA publishes Monthly Highlights on the Climate System including information on the characteristics of climatic anomalies and extreme events around the world, atmospheric circulation and oceanographic conditions. It can be found at https://www.data.jma.go.jp/tcc/tcc/products/clisys/highlights/index.html.

(2) Spring (March – May 2023)

SSTs in the eastern equatorial Pacific increased, and significantly positive SST anomalies were observed in the western and eastern equatorial Pacific in association with the emergence and development of an El Niño event (Figure 1.3-2 (a)).

Tropical convection was enhanced over the latitude bands from 10 to 20°N in the western and central tropical Pacific, and was suppressed from the Indochina Peninsula to the eastern Indian Ocean and over the equatorial central South Pacific (Figure 1.3-2 (b)). In the upper troposphere, cyclonic circulation anomalies straddling the equator were seen over the Indian Ocean, and cyclonic circulation anomalies were seen in the tropical North Pacific (Figure 1.3-2 (c)). In the lower troposphere over the tropics, anti-cyclonic circulation anomalies straddling the equator were seen over the Indian Ocean, and cyclonic circulation anomalies were seen over the western North Pacific (Figure 1.3-2 (d)). These anomalies generally correspond to tropical convection.

In the 500-hPa height field, the polar vortex in the Northern Hemisphere was stronger than normal to the north of Central Siberia. A wavy pattern in anomalies was seen from Greenland to northern Eurasia, and zonally elongated positive anomalies were seen from East Asia to the mid-latitude North Pacific (Figure 1.3-2 (e)). In the sea level pressure field, negative anomalies were seen from the Siberian side of the Arctic Ocean to Central and Eastern Siberia and over the mid-latitude North Atlantic, and zonally elongated positive anomalies were seen from Japan to the south of the Aleutian Islands (Figure 1.3-2 (f)). Temperatures at 850 hPa were above normal over northern North America and from Japan to the mid-latitude North Pacific, and were below normal over the Arctic ocean (Figure 1.3-2 (g)).

(3) Summer (June – August 2023)

The El Niño event that started in boreal spring developed, and positive SST anomalies over a wide area of the equatorial Pacific were accompanied by significant anomalies from central to eastern parts. In the tropical Indian Ocean, significantly positive anomalies were seen from the Bay of Bengal to the tropical western part and negative anomalies were seen in the tropical southeastern part, indicating the positive phase of the Indian Ocean Dipole (IOD) event (Figure 1.3-3 (a)).

Tropical convection was enhanced from seas east of the Philippines to the western equatorial Pacific and over the equatorward-shifted intertropical convergence zone in the eastern Pacific, and was suppressed in the Indian Ocean (Figure 1.3-3 (b)). In the upper troposphere, cyclonic circulation anomalies straddling the equator were seen from Africa to the Indian Ocean, and anti-cyclonic circulation anomalies straddling the equator were seen over the central to eastern Pacific. Zonally elongated cyclonic circulation anomalies were seen from seas northwest of Hawaii to the western coast of the USA, indicating an enhanced Mid-Pacific trough (Figure 1.3-3 (c)). In the lower troposphere, anti-cyclonic circulation anomalies straddling the equator were seen over the Indian Ocean, and cyclonic circulation anomalies were seen to the south of Japan (Figure 1.3-3 (d)). The anomalies over the tropical Pacific correspond to equatorward-shifted enhanced convection over the eastern tropical Pacific, suggesting an influence from the El Niño event.

In the 500-hPa height field, a hemispheric-scale wavy pattern of anomalies was seen, with positive anomalies over northwestern North America, to the south of Greenland, to the north of the Scandinavian Peninsula and to the east of Japan, and negative anomalies were seen over eastern North America (Figure 1.3-3 (e)). In the sea level pressure field, the North Atlantic subtropical high was weaker than normal, and the North Pacific subtropical high was stronger than normal. Negative anomalies were seen from west of Japan to the Aleutian Islands (Figure 1.3-3 (f)). Temperatures at 850 hPa were above normal over a wide area of the

Northern Hemisphere (Figure 1.3-3 (g)).

Record-hot conditions were observed over northern and eastern Japan in late July in association with an intensified North Pacific subtropical high extension toward the country (News I).

(4) Autumn (September – November 2023)

The El Niño event that started in boreal spring persisted, and positive SST anomalies were observed over a wide area of the equatorial Pacific, accompanied by significant anomalies from central to eastern parts. In the tropical Indian Ocean, significantly positive anomalies were seen in the western part and significantly negative anomalies were seen in the southeastern part, corresponding to the positive phase of the IOD event that started in boreal summer (Figure 1.3-4 (a)).

Tropical convection was enhanced in the equatorial Pacific and the western Indian Ocean and suppressed from the eastern Indian Ocean to Indonesia (Figure 1.3-4 (b)). In the upper troposphere, anti-cyclonic circulation anomalies straddling the equator were seen in the tropical Pacific, and cyclonic circulation anomalies straddling the equator were seen over the Indian Ocean (Figure 1.3-4 (c)). In the lower troposphere, anti-cyclonic circulation anomalies straddling the equator were seen over the Indian Ocean. Anti-cyclonic circulation anomalies were also seen in the subtropics from the South China Sea to the western North Pacific (Figure 1.3-4 (d)). Circulation anomalies from the Indian Ocean to the Pacific in the tropics corresponded to tropical convection, suggesting influences from the persistent El Niño event and the positive phase of the IOD.

In the 500-hPa height field, positive anomalies were seen over northern Central Siberia and over the northern North Pacific, and negative anomalies were seen over the eastern North Pacific, from the eastern USA to northern Europe, and over Eastern Siberia (Figure 1.3-4 (e)). The westerly jet stream was stronger than normal from North America to the North Atlantic and shifted southward from its normal position (see Figure 1.3-4 (c)). In the sea level pressure field, positive anomalies were seen over the central North Pacific and to the east of Greenland, and negative anomalies were seen from Europe to Central Asia and over a wide area of the Arctic Ocean (Figure 1.3-4 (f)). Temperatures at 850 hPa were above normal over northern North America, southern Europe and Central Siberia, and negative anomalies were seen over northern Europe (Figure 1.3-4 (g)).

(a) SST anomaly
(Dec. 2022 – Feb. 2023)

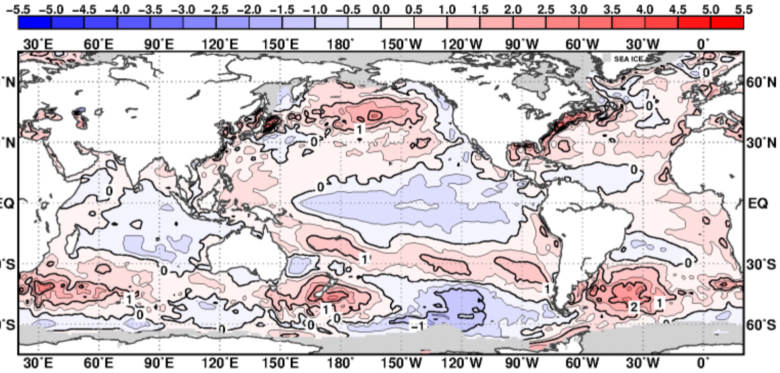

(b) OLR anomaly
(Dec. 2022 – Feb. 2023)

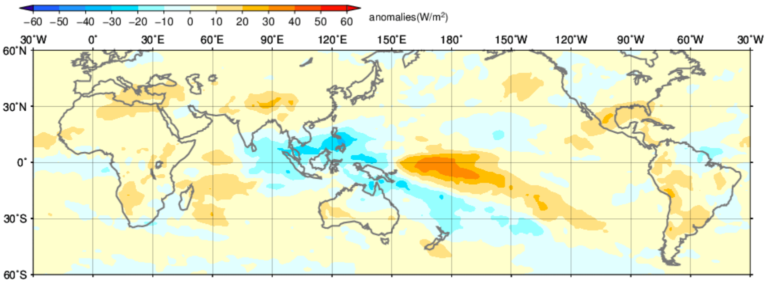

(c) 200hPa stream function and anomaly
(Dec. 2022 – Feb. 2023)

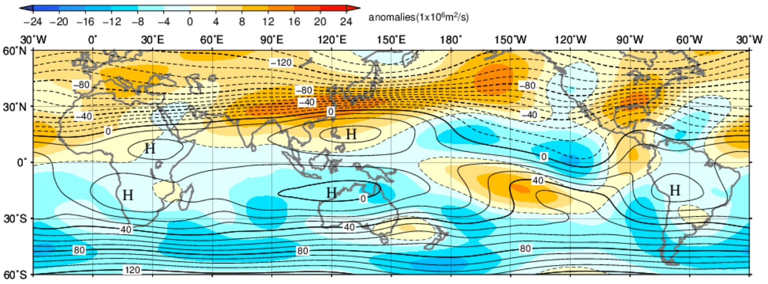

(d) 850hPa stream function and anomaly
(Dec. 2022 – Feb. 2023)

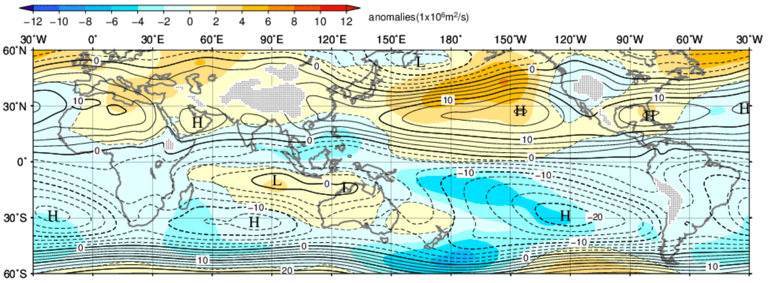

(e) 500hPa height and anomaly
(Dec. 2022 – Feb. 2023)

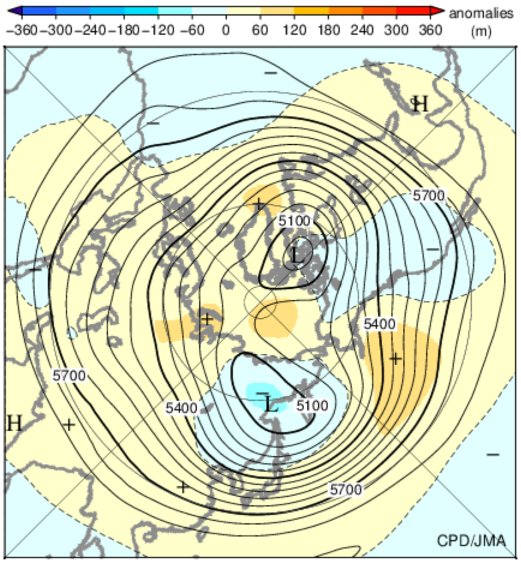

(f) SLP and anomaly
(Dec. 2022 – Feb. 2023)

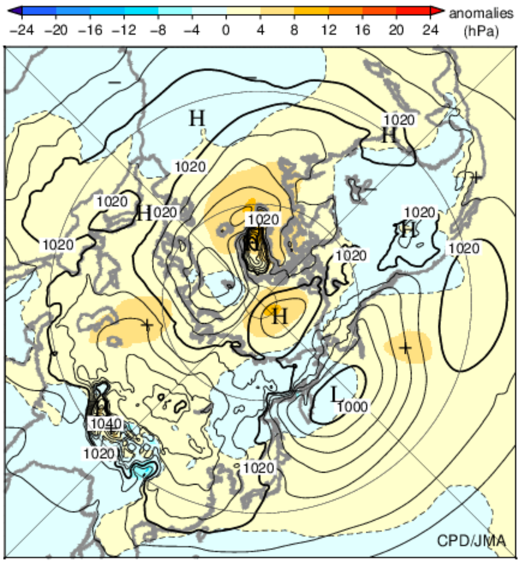

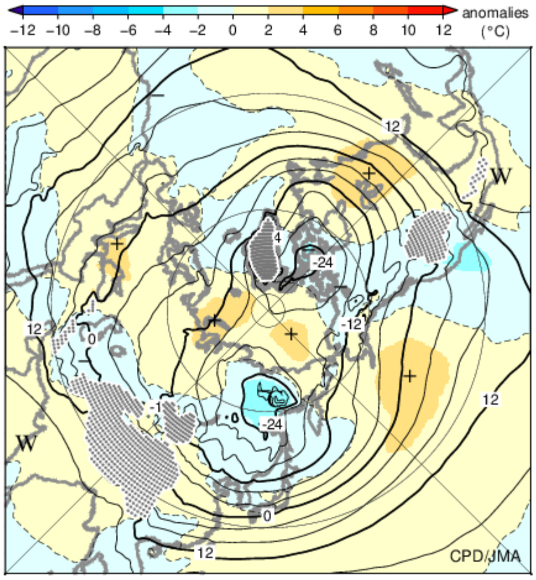

(g) 850hPa temperature and anomaly
(Dec. 2022 – Feb. 2023)

Figure 1.3-1 Three-month mean (a) sea surface temperature (SST) anomaly, (b) outgoing longwave radiation (OLR) anomaly, (c) 200-hPa stream function and anomaly, (d) 850-hPa stream function and anomaly, (e) 500-hPa height and anomaly in the Northern Hemisphere (NH), (f) sea level pressure (SLP) and anomaly in NH, and (g) 850-hPa temperature and anomaly in NH (December 2022 – February 2023)
The base period for the normal is 1991 – 2020. (a) The contour interval is 0.5°C. Sea ice coverage areas are shaded in gray. (b) Negative (cold color) and positive (warm color) OLR anomalies show enhanced and suppressed convection, respectively, compared to the normal. Original data provided by NOAA. The contour intervals are (c) 10 x 10^6 m^2/s and (d) 2.5 x 10^6 m^2/s. "H" and "L" denote high- and low-pressure systems, respectively. (e) Contours show 500-hPa height at intervals of 60 m, and shading indicates height anomalies. "H" and "L" denote high- and low-pressure systems, respectively. (f) Contours show sea level pressure at intervals of 4 hPa, and shading indicates sea level pressure anomalies. "H" and "L" denote high- and low-pressure systems, respectively. (g) Contours show temperature at intervals of 4°C, and shading indicates temperature anomalies. "W" and "C" denote warm and cold conditions, respectively.

(a) SST anomaly
(Mar. – May 2023)

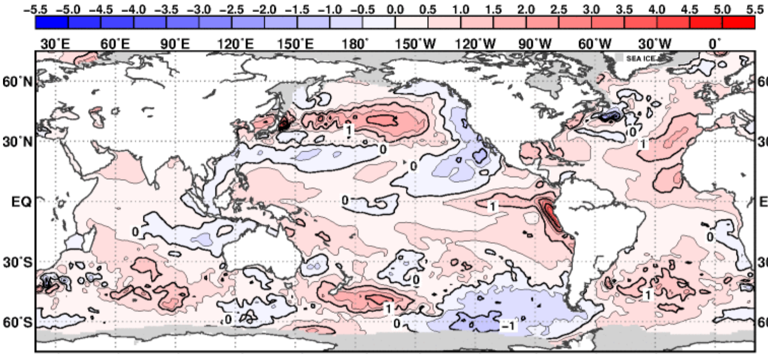

(b) OLR anomaly
(Mar. – May 2023)

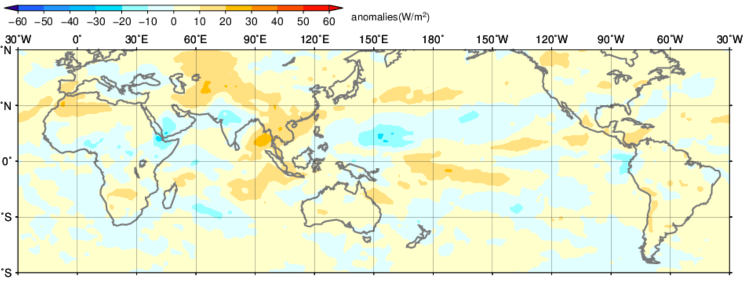

(c) 200hPa stream function and anomaly
(Mar. – May 2023)

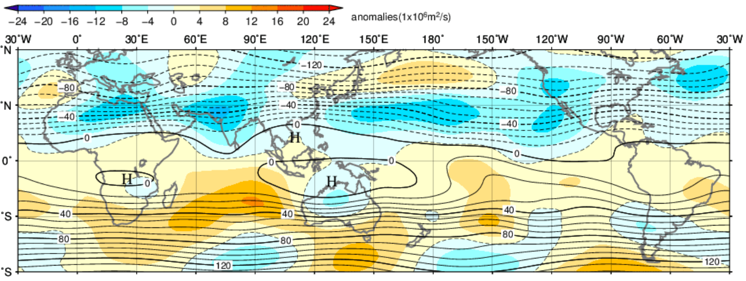

(d) 850hPa stream function and anomaly
(Mar. – May 2023)

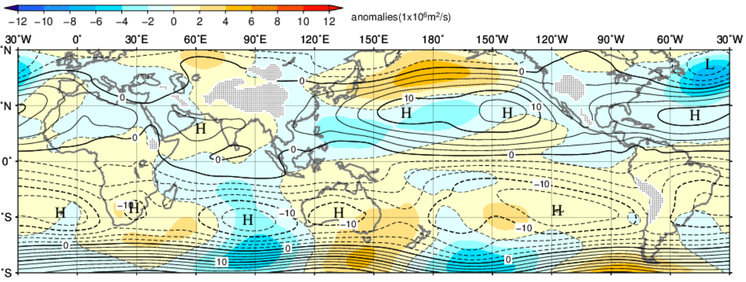

(e) 500hPa height and anomaly
(Mar. – May 2023)

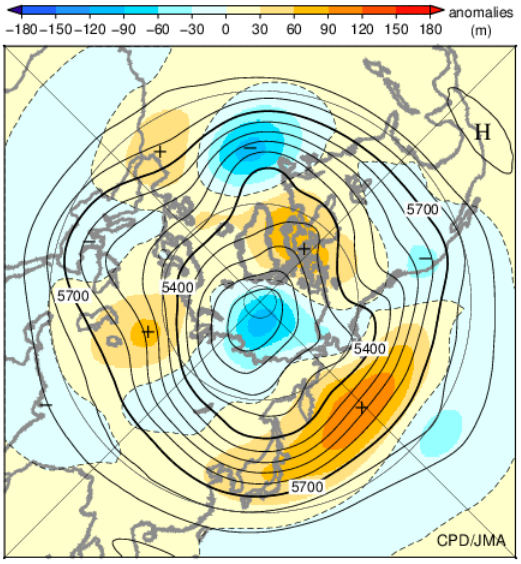

(f) SLP and anomaly
(Mar. – May 2023)

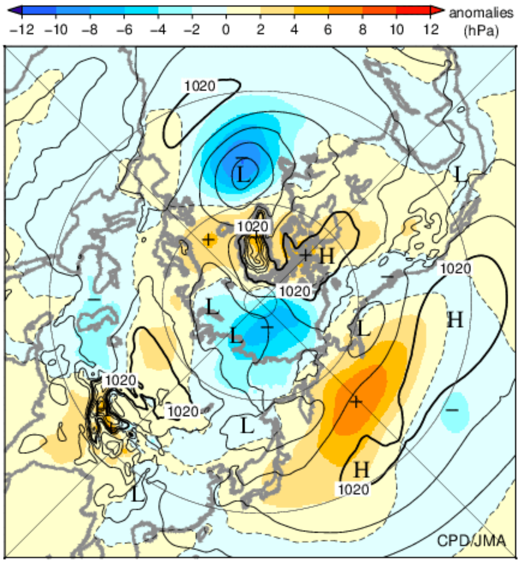

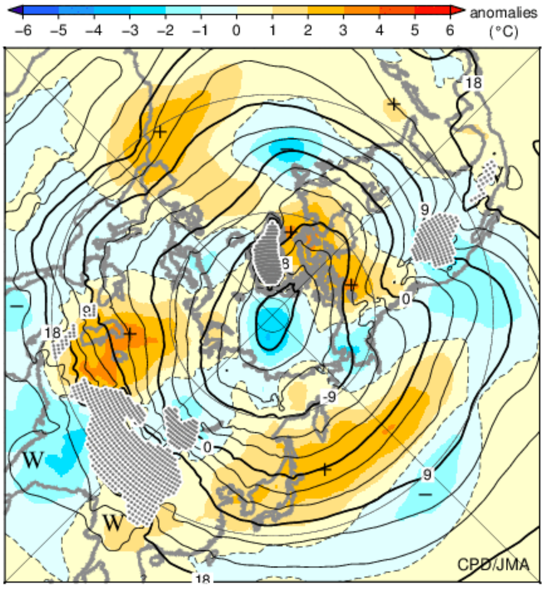

(g) 850hPa temperature
(Mar. – May 2023)

Figure 1.3-2 As per Figure 1.3-1, but for March – May 2023
In (g), the contour interval is 3°C.

(a) SST anomaly
(Jun. – Aug. 2023)

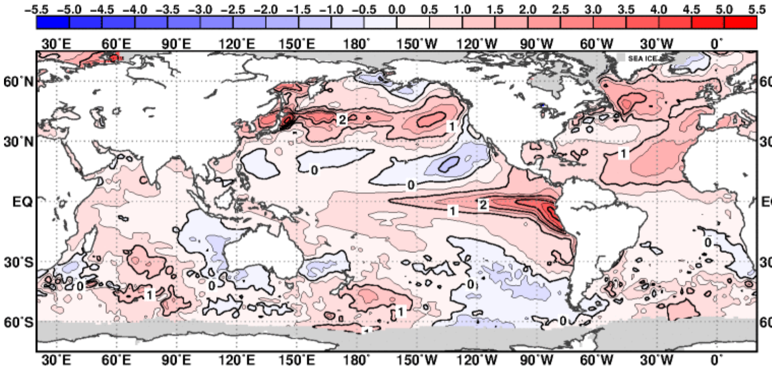

(b) OLR anomaly
(Jun. – Aug. 2023)

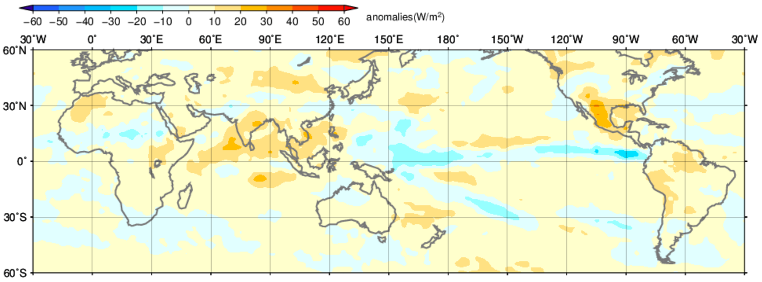

(c) 200hPa stream function and anomaly
(Jun. – Aug. 2023)

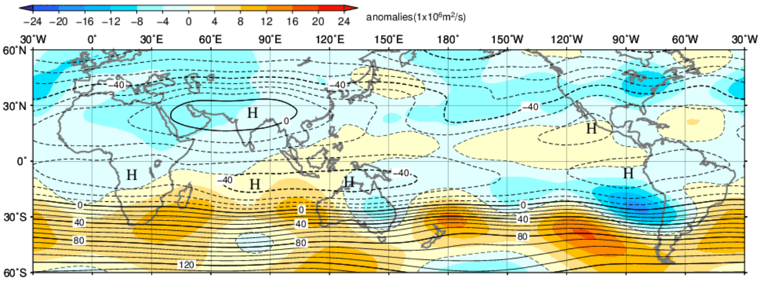

(d) 850hPa stream function and anomaly
(Jun. – Aug. 2023)

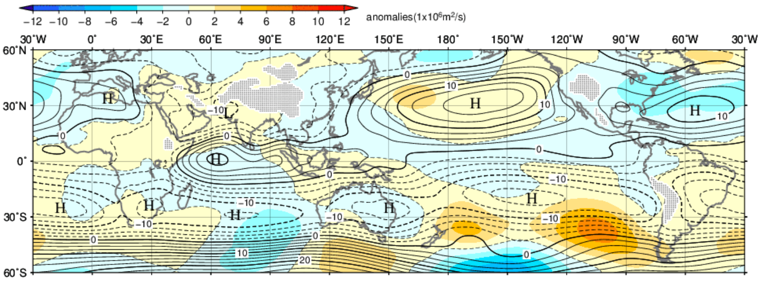

(e) 500hPa height and anomaly
(Jun. – Aug. 2023)

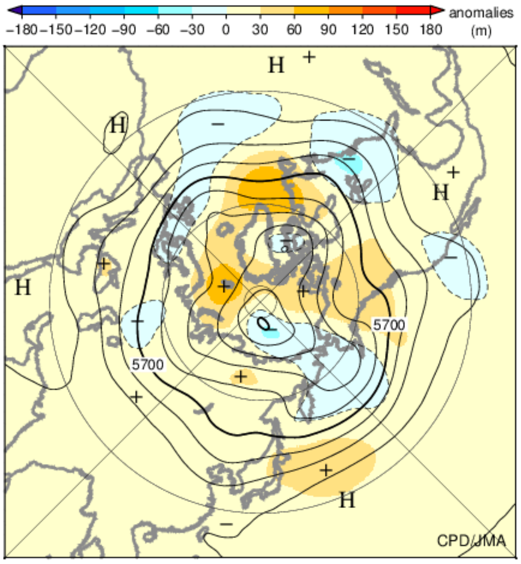

(f) SLP and anomaly
(Jun. – Aug. 2023)

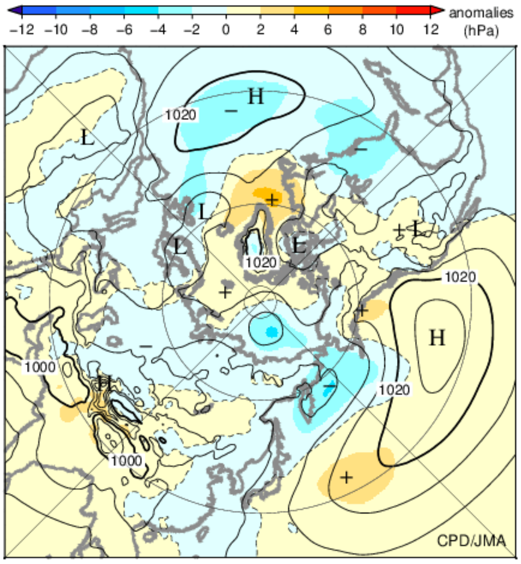

(g) 850hPa temperature and anomaly
(Jun. – Aug. 2023)

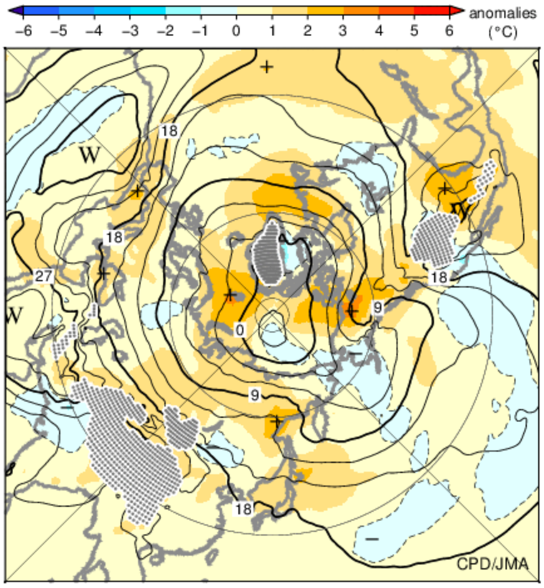

Figure 1.3-3 As per Figure 1.3-1, but for June – August 2023
In (g), the contour interval is 3°C.

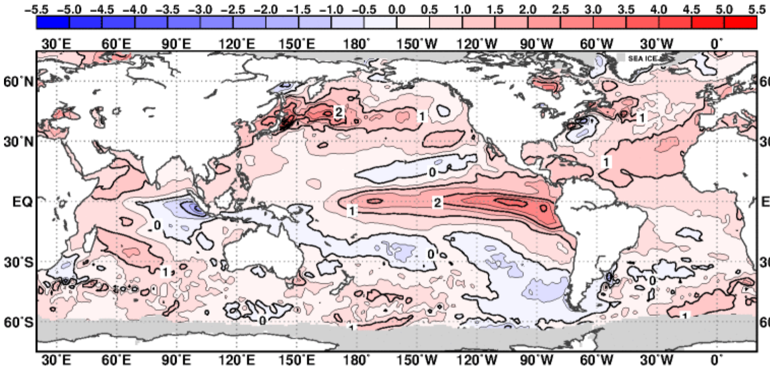

(a) SST anomaly
(Sep. – Nov. 2023)

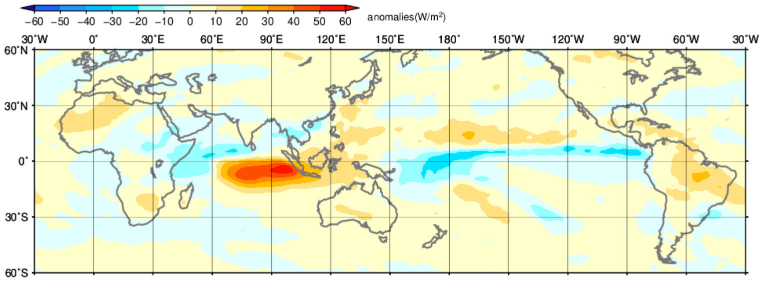

(b) OLR anomaly
(Sep. – Nov. 2023)

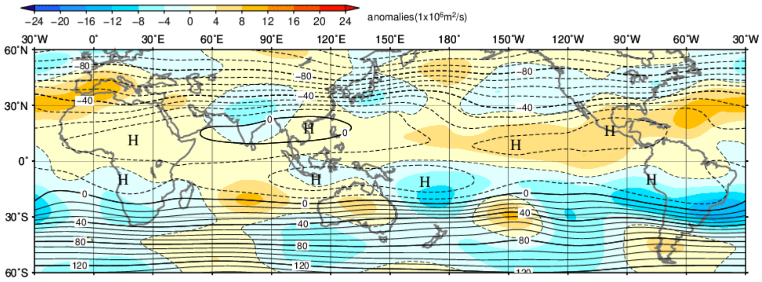

(c) 200hPa stream function and anomaly
(Sep. – Nov. 2023)

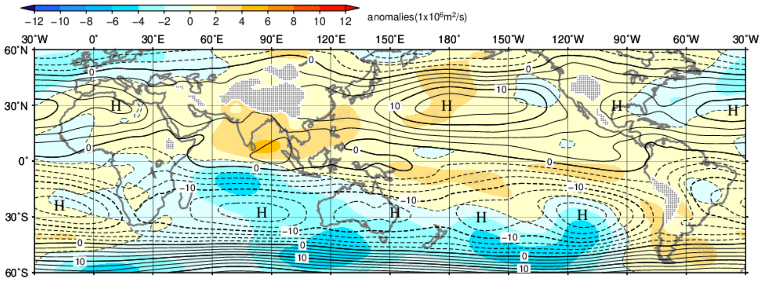

(d) 850hPa stream function and anomaly
(Sep. – Nov. 2023)

(e) 500hPa height and anomaly
(Sep. – Nov. 2023)

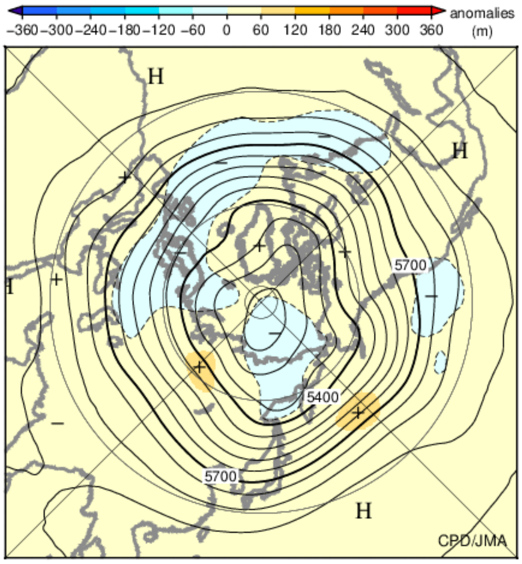

(f) SLP and anomaly
(Sep. – Nov. 2023)

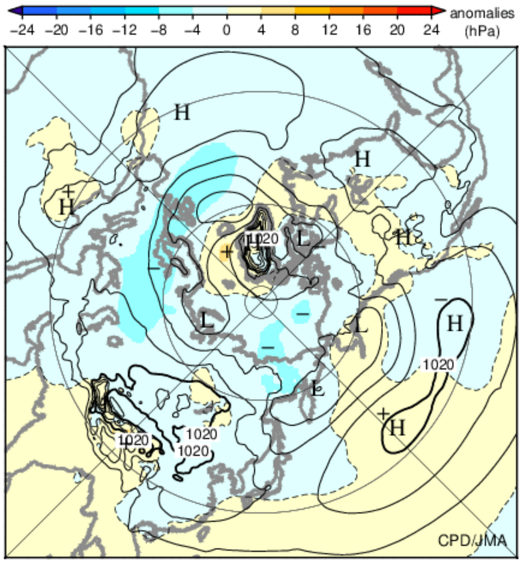

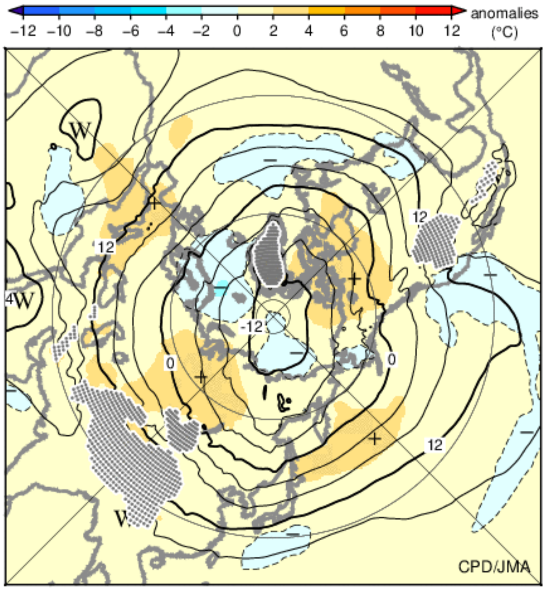
(g) 850hPa temperature and anomaly
(Sep. – Nov. 2023)

Figure 1.3-4 As per Figure 1.3-1, but for September – November 2023

1.3.2 Global average temperature in the troposphere

The global average temperature in the troposphere (Figure 1.3-5) in 2023 remained higher than normal throughout the year, and was significantly increased through boreal autumn. The average zonal mean temperature from September to November 2023 was higher than the normal in the troposphere, particularly in the tropics, in association with the prevailing El Niño conditions (Figure 1.3-6).

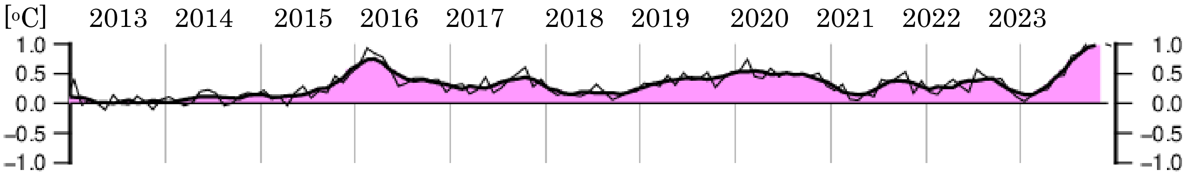

Figure 1.3-5 Time-series representation of global average temperature anomalies calculated from thickness in the troposphere (2013 to 2023)

The thin and thick lines show monthly mean and five-month running mean values, respectively. The base period for the normal is 1991 – 2020.

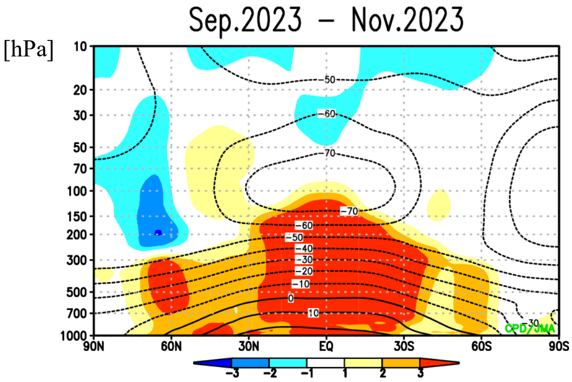

Figure 1.3-6 Latitude-height cross section of zonal mean temperature and anomaly (September – November 2023)

Contours show zonal mean temperature at intervals of 10°C, and shading indicates normalized temperature anomalies by standard deviations of interannual variations. The base period for the normal is 1991 – 2020.

1.3.3 Summer Asian monsoon

Convective activity over the Asian summer monsoon region in 2023 was generally weaker than normal, and showed significant variability with a periodicity from a few weeks to a month, as indicated by the OLR index (SAMOI (A)[9], JMA, 1997; Figure 1.3-7). Convection was enhanced in early May, early June, mid-July, early September and late September.

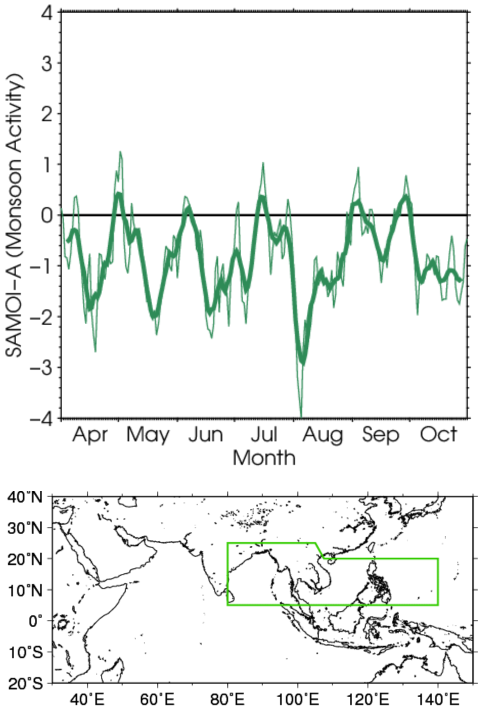

Figure 1.3-7 Time-series representation of the Asian summer monsoon OLR index (SAMOI (A)) (April – October 2023)

The thin and thick green lines indicate daily and seven-day running mean values, respectively. SAMOI (A) indicates the overall activity of the Asian summer monsoon, and positive and negative values indicate enhanced and suppressed convective activity, respectively, compared to the normal. The base period for the normal is 1991 – 2020. Original OLR data provided by NOAA.

---

[9] SAMOI (A) is defined as reversed-sign area-averaged OLR anomalies normalized by its standard deviation. The area for average is enclosed by green line in the map of Figure 1.3-7.

1.3.4 Tropical cyclones over the western North Pacific and the South China Sea

In 2023, 17 tropical cyclones (TCs) with maximum wind speeds of ≥ 34 kt formed over the western North Pacific and the South China Sea (Figure 1.3-8, Table 1.3-1), which was below the normal of 25.1 (1991 – 2020 average). In the period since September, a total of 5 TCs (normal 11.6) formed, which was the lowest since 1951.

A total of 9 TCs, which was below the normal of 11.7, came within 300 km of the Japanese archipelago. A total of 1 TC, Typhoon Lan made landfall on Japan, which was below the normal of 3.0.

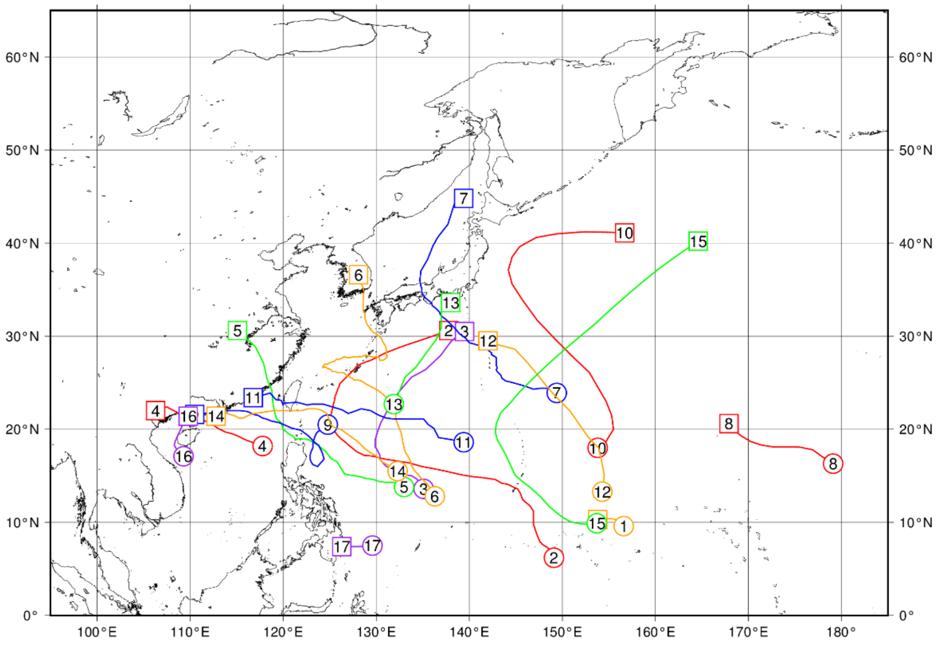

Figure 1.3-8 Tracks of TCs with maximum wind speeds of ≥ 34 kt in 2023
Numbered circles indicate positions of the TC formed (maximum wind speeds of ≥ 34 kt), and numbered squares indicate positions of the TC dissipated (maximum wind speeds lower than 34 kt). Source: RSMC Tokyo-Typhoon Center data.

Table 1.3-1 TCs with maximum wind speeds of ≥ 34 kt in 2023 (Source: RSMC Tokyo-Typhoon Center data)

Number ID	Tropical Cyclone	Duration (UTC)	Maximum Wind[1] (kt)	Number ID	Tropical Cyclone	Duration (UTC)	Maximum Wind[1] (kt)
2301	Sanvu	1200, 20 Apr - 0000, 22 Apr	45	2310	Damrey	1800, 24 Aug - 0600, 29 Aug	50
2302	Mawar	1200, 20 May - 0000, 03 Jun	115	2311	Haikui	1800, 28 Aug - 0000, 05 Sep	85
2303	Guchol	1200, 06 Jun - 1200, 12 Jun	80	2312	Kirogi	1200, 30 Aug - 0000, 03 Sep	45
2304	Talim	0600, 15 Jul - 1200, 18 Jul	60	2313	Yun-yeung	1200, 05 Sep - 1200, 08 Sep	40
2305	Doksuri	0000, 21 Jul - 0000, 29 Jul	100	2314	Koinu	1800, 29 Sep - 0600, 09 Oct	90
2306	Khanun	0000, 28 Jul - 0600, 10 Aug	95	2315	Bolaven	1200, 07 Oct - 1200, 14 Oct	115
2307	Lan	0000, 08 Aug - 0600, 17 Aug	90	2316	Sanba	0000, 18 Oct - 0000, 20 Oct	40
2308	Dora	0600, 12 Aug - 0000, 15 Aug	75	2317	Jelawat	0600, 17 Dec - 0000, 18 Dec	35
2309	Saola	0600, 24 Aug - 1800, 02 Sep	105				

1) Estimated maximum 10-minute mean wind speed

Chapter 2 Climate Change

2.1 Greenhouse gases[10,11]

○ Atmospheric concentrations of carbon dioxide are increasing.
○ Atmospheric concentrations of methane have shown an ongoing increase (with the exception of a stationary phase from 1999 to 2006).
○ Atmospheric concentrations of nitrous oxide are increasing.
○ Among halocarbons, atmospheric concentrations of chlorofluorocarbons are decreasing, while those of hydrofluorocarbons are increasing.

JMA operates the World Data Centre for Greenhouse Gases (WDCGG)[12] to collect, maintain and provide data on greenhouse gases for related monitoring on a global scale under the Global Atmosphere Watch (GAW) Programme of the World Meteorological Organization (WMO). Analysis of data reported to WDCGG shows that the global mean concentration of long-lived greenhouse gases with strong effects on global warming (in particular, carbon dioxide (CO_2), methane (CH_4) and nitrous oxide (N_2O)) continues to increase (Table 2.1-1).

In Japan, JMA monitors surface-air concentrations of greenhouse gases via three observation stations at Ryori in Ofunato, Minamitorishima in the Ogasawara Islands and Yonagunijima in the Nansei Islands. JMA research vessels are used to observe oceanic and atmospheric CO_2 in sea areas near Japan and in the western North Pacific. In addition, sampling of greenhouse gases in upper-air areas using cargo aircraft was commenced in 2011 (Figure 2.1-1).

Table 2.1-1 Atmospheric concentrations of major long-lived greenhouse gases (2022)[13]

	Atmospheric mole fraction			Absolute increase from 2021	Relative increase from 2021	Lifetime
	Pre-industrial level around 1750	Global mean in 2022	Relative increase from Pre-industrial level			
Carbon dioxide	About 278 ppm	417.9 ppm	+ 50 %	+2.2 ppm	+0.53 %	-
Methane	About 729 ppb	1,923 ppb	+164 %	+16 ppb	+0.84 %	11.8 years
Nitrous oxide	About 270 ppb	335.8 ppb	+ 24 %	+1.4 ppb	+0.42 %	109 years

---

[10] Part of this section shows observational outcomes for the period until 2022, as greenhouse gas observation data for 2023 were not yet fully available at the time of publication.

[11] Information on greenhouse gas monitoring is published on JMA's website.
https://www.data.jma.go.jp/ghg/info_ghg_e.html (Atmospheric greenhouse gases)

[12] See the WDCGG website for more information.
https://gaw.kishou.go.jp/

[13] Data on the annual mean mole fraction in 2022 and its absolute and relative differences from the previous year are from WMO (2023), while data on pre-industrial levels and lifetime are from IPCC (2021). The lifetime of gas as referred to here describes the time scale over which a local instantaneous increment of gas decays. The increase from pre-industrial levels is calculated from mole fractions for the pre-industrial era and 2022.

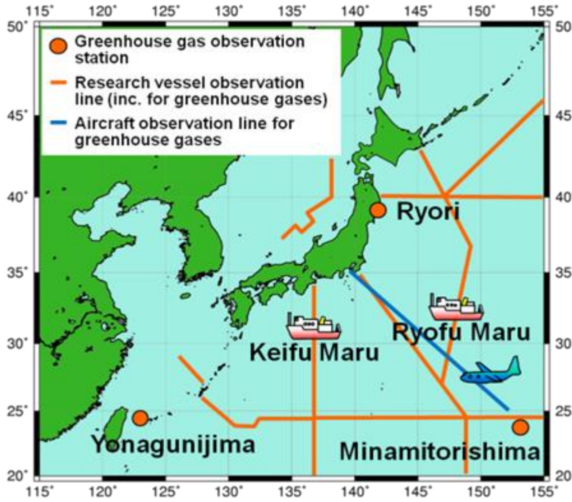

Figure 2.1-1 JMA's greenhouse gas observation network as of 2023

Observation stations at Ryori, Minamitorishima and Yonagunijima and regular monitoring routes of research vessel and cargo aircraft.

2.1.1 Concentration of carbon dioxide

(1) Concentration of global atmospheric carbon dioxide

The global mean concentration of atmospheric CO_2 shows a trend of increase with seasonal variations (Figure 2.1-2 (a)), primarily due to influences associated with human activity such as fossil fuel combustion and land-use changes (e.g., deforestation) (IPCC, 2021). Some anthropogenic CO_2 is absorbed by the terrestrial biosphere and the oceans, while the rest remains in the atmosphere. As most major sources of CO_2 are located in the Northern Hemisphere, concentrations tend to be higher in the mid- and high latitudes there and lower in the Southern Hemisphere (Figure 2.1-3).

The seasonal variability of CO_2 concentration is generally attributable to terrestrial biosphere activity. In summer, active plant photosynthesis consumes masses of CO_2, while emissions from plant respiration and organic-matter decomposition become dominant in winter (IPCC, 2021). As a result, the annual maximum concentration is observed from March to April in the Northern Hemisphere and from September to October in the Southern Hemisphere. Seasonal variations exhibit larger amplitudes in the mid- and high latitudes of the Northern Hemisphere than in the ocean-rich Southern Hemisphere (Figure 2.1-3). Accordingly, global mean CO_2 concentrations usually peak around April, reflecting strong seasonal variations in the Northern Hemisphere.

WDCGG analysis shows that global mean surface CO_2 concentration increased by 2.2 ppm from 2021 to 2022, reaching as much as 417.9 ppm (Table 2.1-1). The most recent 10-year average annual growth rate is 2.5 ppm/year, as opposed to the corresponding value of 1.5 ppm/year for the 1990s.

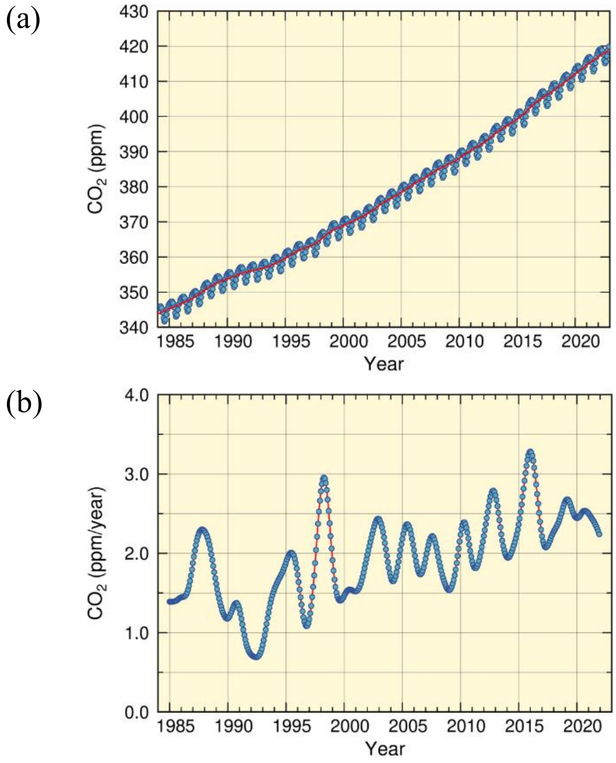

Figure 2.1-2 Global mean concentration of atmospheric CO_2 (a) and annual growth rate (b)
In the upper panel the blue dots are monthly values, and the red line represents the corresponding sequence after removal of seasonal variations. From the latter, the growth rate is derived and shown in the lower panel. Graph content is based on analysis of observation data reported to WDCGG using the method of WMO (2009). Data contributors are listed in WMO (2024).

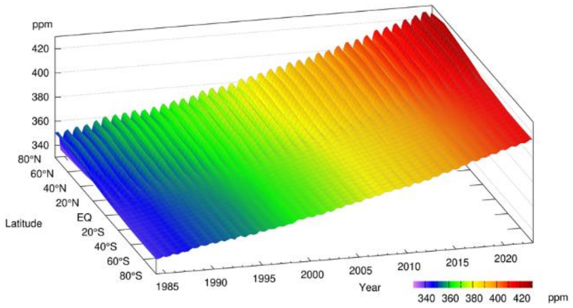

Figure 2.1-3 Latitudinal distribution of atmospheric CO_2 concentrations
The data set and analysis method are as per Figure 2.1-2.

The growth rate of CO_2 concentration exhibits significant interannual variations (Figure 2.1-2 (b)). Major increases in concentration often coincide with El Niño events, largely because the terrestrial biosphere emits more CO_2 than usual under such conditions. In particular, El Niño events bring about high temperatures and droughts in tropical areas and elsewhere, thereby promoting plant respiration and organic-matter decomposition in soil and hindering plant photosynthesis (Keeling *et al.*, 1995; Dettinger and Ghil, 1998).

Figure 2.1-4 illustrates net CO_2 uptake by the terrestrial biosphere as estimated using the method of Le Quéré *et al.* (2016). Here, CO_2 uptake is defined as the amount of anthropogenic emissions minus the increment of atmospheric concentration and the amount of uptake by oceans. The low uptake by the terrestrial biosphere in 2015 and 2016 is generally attributed to the 2014 – 2016 El Niño event (WMO, 2018b). The annual net CO_2 uptakes in 2015 and 2016 were both lower than the 10-year average of 2.7 ± 1.2 GtC/year for the period 2012 – 2021. Similar suppression of net CO_2 uptake was observed in association with the El Niño events of 1997/1998 and 2002/2003. An exception was observed from 1991 to 1992, when net CO_2 uptake by the terrestrial biosphere was large despite the presence of an El Niño event. This is attributable to the eruption of Mt. Pinatubo in June 1991, which triggered worldwide low temperatures and inhibited CO_2 emissions from organic-matter decomposition in soil (Keeling *et al.*, 1996; Rayner *et al.*, 1999).

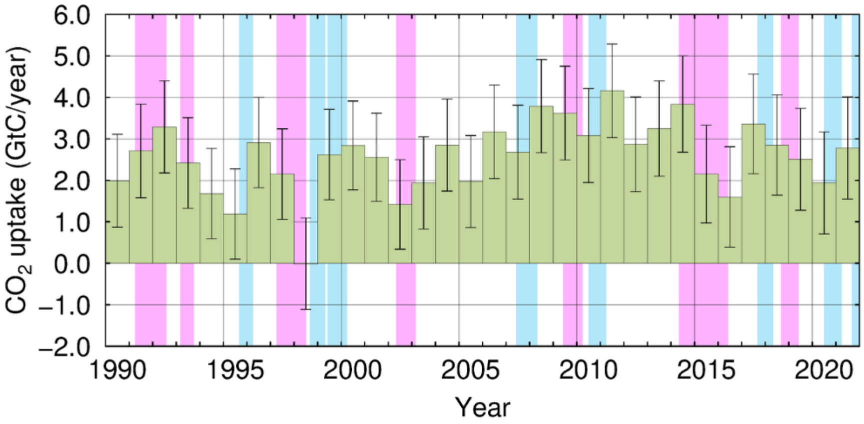

Figure 2.1-4 Annual net CO_2 uptake by the terrestrial biosphere
In this analysis, the net CO_2 uptake is estimated by subtracting the annual increment of atmospheric CO_2 and the amount of uptake by oceans from the amount of anthropogenic emissions. The amount of anthropogenic emissions stemming from fossil fuel combustion, cement production (including cement carbonation sinks) and land-use change is based on Friedlingstein *et al*. (2023). The annual increment of atmospheric CO_2 is the annual mean of the monthly means shown in Figure 2.1-2 (b). Oceanic uptake is based on Iida *et al*. (2021; see also Section 2.12.1 (2)), and incorporates emissions associated with the natural carbon cycle, corresponding to 0.6 GtC/year (IPCC, 2021). Error bars indicate 68% confidence levels. El Niño and La Niña periods are shaded in red and blue, respectively. A negative CO_2 uptake equates to an emission.

(2) Concentration of atmospheric carbon dioxide in Japan

Concentrations of atmospheric CO_2 at all three of Japan's observation stations have shown a continuous increase along with seasonal variations (Figure 2.1-5 (a)). The amplitude of these variations is greater at Ryori than at the other stations because it tends to be larger in higher latitudes of the Northern Hemisphere in association with significant seasonal variations in terrestrial biosphere activity in the mid- and high latitudes (see Figure 2.1-1). Although Yonagunijima and Minamitorishima have similar latitudes, the former tends to observe higher concentrations and seasonal variations with larger amplitudes because of its greater proximity to the Asian continent, which is characterized by major anthropogenic emissions and an extensive biosphere. The annual mean CO_2 concentration in 2023 was 425.0 ppm at Ryori, 421.8 ppm at Minamitorishima and 424.4 ppm at Yonagunijima (based on preliminary estimations). The increase from the previous year was 2.1 to 3.1 ppm/year, which is comparable to the mean annual absolute increase over the last 10 years.

Figure 2.1-5 (b) shows growth rates of CO_2 concentrations observed at the three observation stations. High rates have been observed in most cases during the periods of El Niño events. As a recent example, a sharp increase in CO_2 concentration was observed in association with the event that ran from summer 2014 to spring 2016.

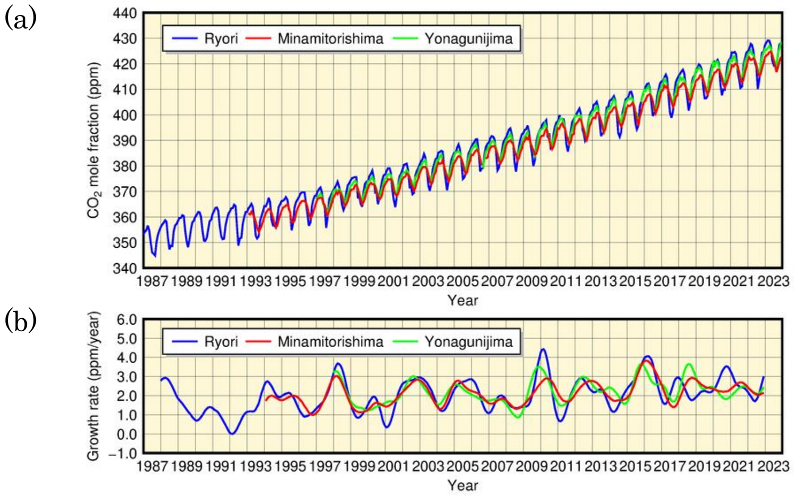

Figure 2.1-5 Monthly mean concentrations (a) and corresponding growth rates (b) of atmospheric CO_2 observed at Ryori (blue), Minamitorishima (red) and Yonagunijima (green)
The method used to calculate the growth rate is described in WMO (2009).

(3) Concentration of carbon dioxide in the upper air

Since 2011, JMA has monitored upper-air CO_2 concentrations using cargo aircraft with support from Japan Ministry of Defense, with air samples taken along the route from Atsugi Air Base (35.45°N, 139.45°E) to Minamitorishima Island (24.29°N, 153.98°E) during level flight at an altitude of approximately 6 km and during descent[14] to the island once a month (Tsuboi *et al.*, 2013; Niwa *et al.*, 2014).

Figure 2.1-6 shows measured and averaged concentrations for samples collected during level flight in black and blue dots, respectively. Monthly mean concentrations at the ground-based station on the island are also shown in red. The dashed curves in blue and red represent components after removal of seasonal cycles for aircraft and Minamitorishima, respectively. Concentrations exhibit a gradual increase over time in the upper air as well as on the surface, although values tend to be lower in the former.

Figure 2.1-7 shows the vertical dependence of average seasonal cycles based on air samples collected during descent in addition to level-flight data and ground-based data. To allow direct comparison, these monthly values are calculated by averaging concentrations after removal of long-term trends in surface observation data. At each level, the information shows similar seasonal variations with higher values from winter to spring and lower values from summer to fall, while significant vertical dependence with lower values toward higher altitudes is observed from winter to spring. Consequently, the amplitude of seasonal cycles is smaller in the upper air.

Figure 2.1-8 shows concentrations for samples taken during descent minus the daily mean value recorded at the ground-based station on the flight date for February (left) and August (right). While concentrations are lower toward higher altitudes in February, there is no clear vertical dependence in August.

The above results suggest that parts of surface air affected by the terrestrial biosphere in continental regions are transported to the ground and upper levels of the island, and that air transport behavior varies with seasons and altitudes. The characteristic of strong vertical dependence from winter to spring and weak dependence from summer to fall is also identified in data from other aircraft observations around North America and Asia (Sweeney *et al.*, 2015; Umezawa *et al.*, 2018).

---

[14] Although some air samples are taken during ascent flights from Minamitorishima Island, all vertical samplings are referred to here as descent samplings.

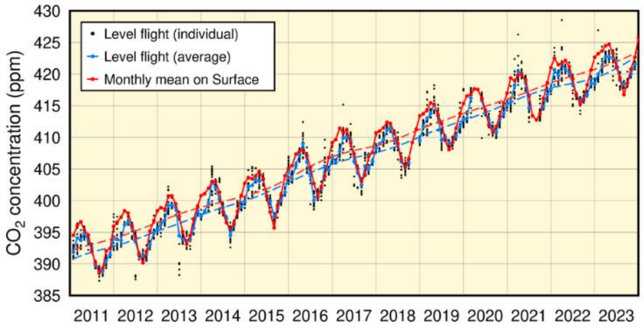

Figure 2.1-6 Measured and single-cruise average CO₂ concentrations for air samples collected during level flight (height: approx. 6 km) of cargo aircraft from Atsugi Air Base to Minamitorishima (black and blue dots, respectively) and monthly mean concentrations at the Minamitorishima ground station (red dots)

Blue and red dashed lines represent components after the removal of seasonal cycles from the series of blue and red dots, respectively. The analysis is based on WMO (2009).

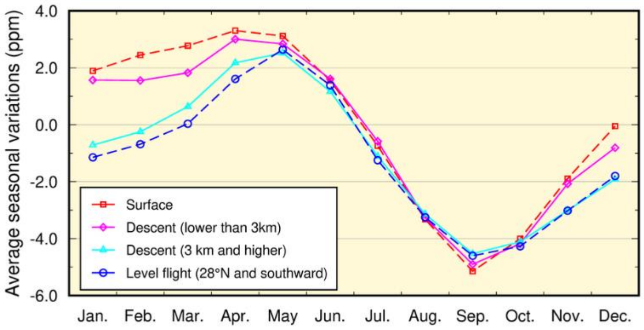

Figure 2.1-7 Vertical dependence of average seasonal cycles around Minamitorishima for monthly mean concentrations on the surface (red), concentrations for air samples taken during level flight at latitudes of 28°N and southward (blue), and values recorded during descent with altitudes less than 3 km (magenta) and otherwise (cyan) based on data covering the period from February 2011 to December 2023

Monthly values are calculated by averaging concentrations after removal of long-term trends (components without seasonal cycles) for surface observation data (the red dashed line in Figure 2.1-6).

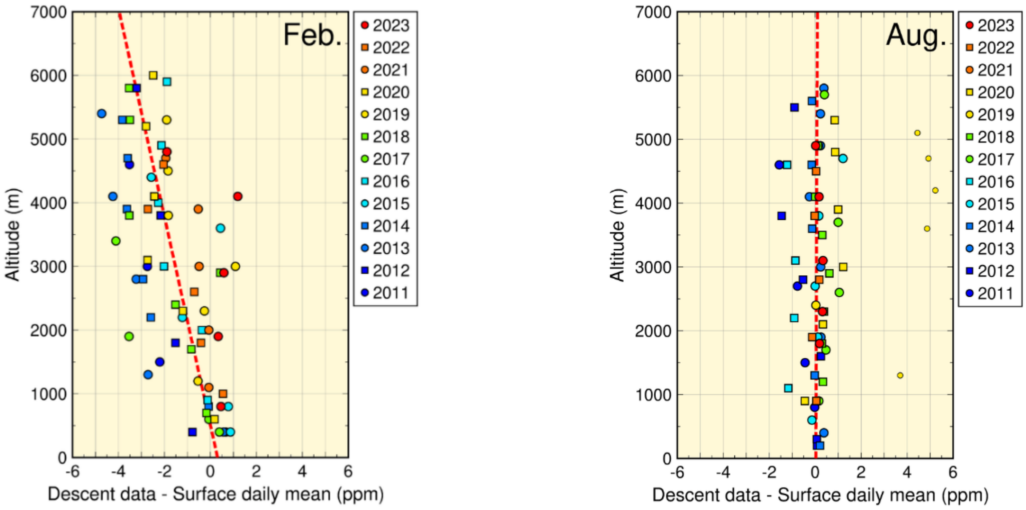

Figure 2.1-8 Vertical variations of CO₂ concentrations over Minamitorishima

Circles and squares show concentrations of air samples taken during descent to the island minus the daily mean value recorded at the ground-based station on the flight date. Symbol colors and shapes represent observation years. Dashed red lines show the vertical gradient of the symbols as determined using the least squares method. To determine representative characteristics for the observation area, outlier data (small symbols) beyond the 3 sigma of the residual standard deviation from the fitted line are excluded from calculation for the vertical gradient. On the flight date in August 2019, daily mean concentration on the surface was 4 – 5 ppm lower than that during descent because continental air masses with low CO₂ concentrations were transported to areas near the ground around Minamitorishima. It should be noted that observations for August 2021 were missing.

2.1.2 Concentration of methane

(1) Concentration of global atmospheric methane

The global mean concentration of atmospheric CH_4 has been increasing since at least the mid-1980s when worldwide monitoring began, except for a stationary phase from 1999 to 2006 (Figure 2.1-9). IPCC (2021) reported that anthropogenic emissions from the oil and gas sectors declined through the 1990s, and that concurrent emission changes from fossil fuels and the agricultural sector may be responsible for the greater concentrations observed since 2007. Meanwhile, large uncertainties still remain in relation to CH_4 emissions from wetlands and biomass combustion driven by El Niño Southern Oscillation and variations in hydroxyl radicals[15], which contribute to CH_4 destruction.

WDCGG analysis shows that the global mean concentration of CH_4 in 2022 was 1,923 ppb, which is the highest since records began (Table 2.1-1).

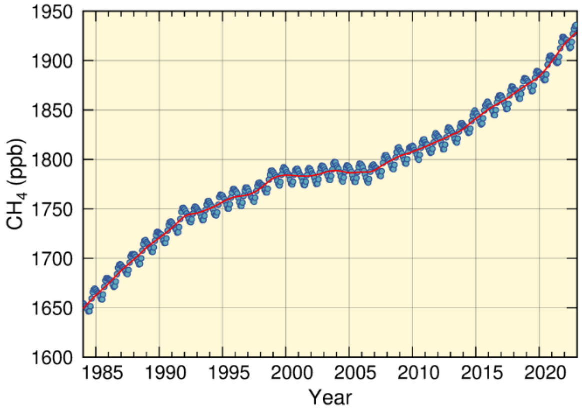

Figure 2.1-9 Global mean concentration of atmospheric CH_4

The blue dots are monthly values, and the red line represents the corresponding sequence after the removal of seasonal variations. Graph content is based on analysis of observation data reported to WDCGG based on the method of WMO (2009). Data contributors are listed in WMO (2024).

Figure 2.1-10 shows the latitudinal dependence of CH_4 concentrations. Values are lower in the tropics than in the high and mid-latitudes of the Northern Hemisphere because CH_4 is mostly emitted from land areas in the Northern Hemisphere, and disappears due to reaction with hydroxyl radicals over tropical oceans during transportation to the Southern Hemisphere. In summer, more CH_4 is destroyed because more hydroxyl radicals are produced as a result of enhanced ultraviolet radiation and water vapor. This reaction contributes to seasonal variations of CH_4 concentrations in both hemispheres, with lower values in summer and higher values in winter (Figures 2.1-9 and 2.1-10).

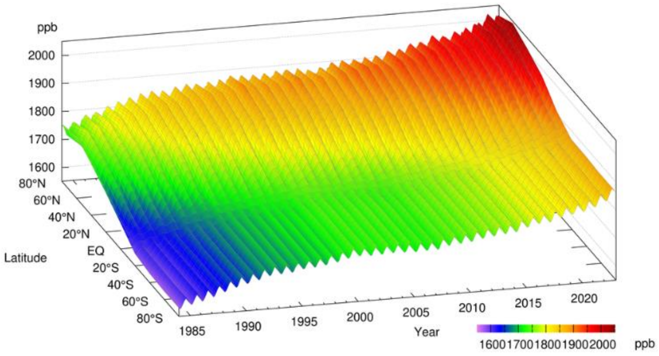

Figure 2.1-10 Latitudinal distribution of atmospheric CH_4 concentrations

The data set and analysis method are as per Figure 2.1-9.

The remarkable increase observed in global mean atmospheric concentrations of CH_4 since the industrial

---

[15] Hydroxyl radicals are highly reactive chemicals generated by the reaction of atomic oxygen, which is derived from UV photolysis of ozone, with airborne water vapor. It is particularly abundant at low latitudes, where UV radiation is strong and water vapor is plentiful.

era (+164%) has been much more rapid than that of CO_2 (+50%) (Table 2.1-1). This is partly because around 40% of CH_4 released into the atmosphere is of natural origin (wetlands, termites, etc.) and around 60% is from human-related activity sources (ruminants, rice paddies, fossil fuel mining, landfill, biomass burning, etc.), and anthropogenic emissions of CH_4 exceed natural emissions. The long-term trend of CH_4 concentration depends on various factors of uncertainty, including anthropogenic/natural emissions and chemical reactions. Accordingly, further development of the global CH_4 observation network is required.

(2) Concentration of atmospheric methane in Japan

Atmospheric CH_4 concentrations at all of Japan's three observation stations exhibit a trend of increase with seasonal variations in the same way as the global mean concentration (Figure 2.1-11 (a)). Ryori usually observes the highest concentration among the three stations because it is located in the northern part of Japan, where CH_4 sources in the Asian continent are more influential and reaction with hydroxyl radicals is less marked. Although Yonagunijima and Minamitorishima are located at similar latitudes, the former tends to record higher concentrations in winter because CH_4 sources on the Asian continent have a stronger impact there in winter as a result of continental air mass expansion. In summer, meanwhile, a hydroxyl radical-rich maritime air mass covers both stations, and similarly low concentrations are observed. Since 2010, Yonagunijima has occasionally observed concentrations as high as those of Ryori in winter. The annual mean CH_4 concentration in 2023 was 2,004 ppb at Ryori, 1,957 ppb at Minamitorishima and 1,981 ppb at Yonagunijima, all of which are the highest on record (based on preliminary estimations).

The growth rate of atmospheric CH_4 concentration exhibits interannual variations that differ significantly from station to station (Figure 2.1-11 (b)).

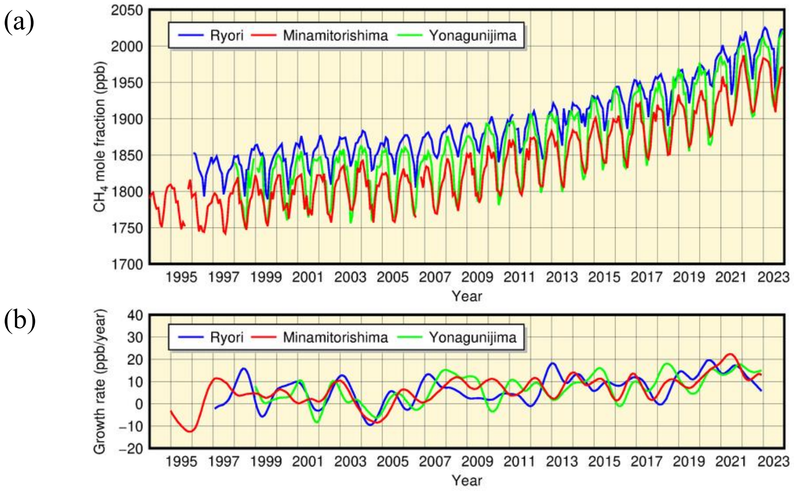

Figure 2.1-11 Monthly mean concentrations (a) and corresponding growth rates (b) of atmospheric CH_4 observed at Ryori (blue), Minamitorishima (red) and Yonagunijima (green)
The method for calculating the growth rate is described in WMO (2009).

2.1.3 Concentration of nitrous oxide

Figure 2.1-12 shows that the global mean concentration of atmospheric N_2O has been continuously increasing. The annual mean concentration in 2022 was 335.8 ppb, which was 24% above the pre-industrial level of 270 ppb (Table 2.1-1). Around 57% of N_2O released into the atmosphere is of natural origin (oceans, soil, etc.), and around 43% is from human activity-related sources (biomass burning, nitrate fertilizers, various industrial processes, etc.). Seasonal variations of N_2O concentrations were lower than those of CH_4 because N_2O has a longer lifetime (109 years). The hemispheric mean concentration is approximately 1 ppb higher in the Northern Hemisphere than in the Southern Hemisphere (Figure 2.1-13) because there are more sources of anthropogenic emissions in the former. This inter-hemispheric difference is, however, much smaller than those observed with CH_4 due to the long atmospheric lifetime of N_2O.

The atmospheric N_2O concentration at Ryori exhibits characteristics similar to those of the global mean (Figure 2.1-14). The annual mean concentration in 2023 at Ryori was 339.8 ppb (based on preliminary estimations).

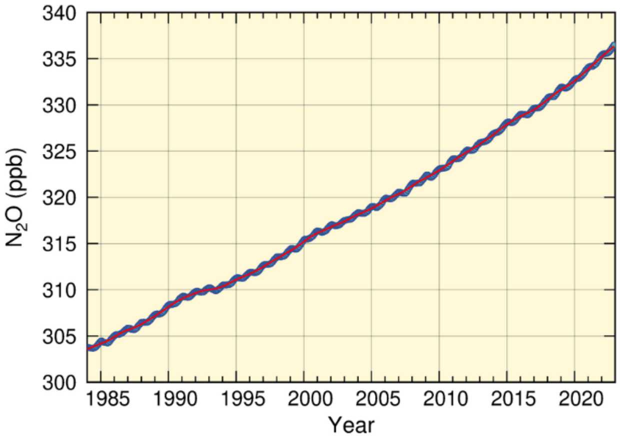

Figure 2.1-12 Global mean concentration of atmospheric N_2O
The blue dots are monthly values, and the red line represents the corresponding sequence after the removal of seasonal variations. Graph content is based on analysis of observation data reported to WDCGG based on the method of WMO (2009). Data contributors are listed in WMO (2024).

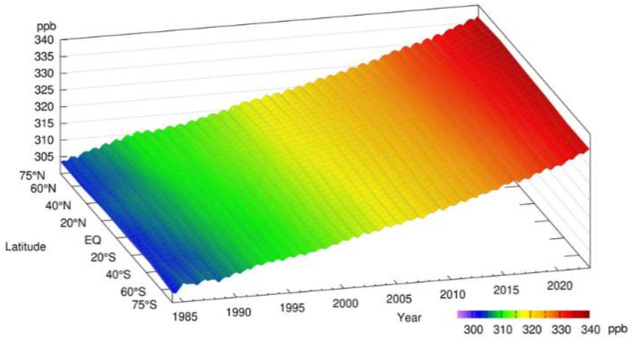

Figure 2.1-13 Latitudinal distribution of atmospheric N_2O concentrations
The data set and analysis method are as per Figure 2.1-12.

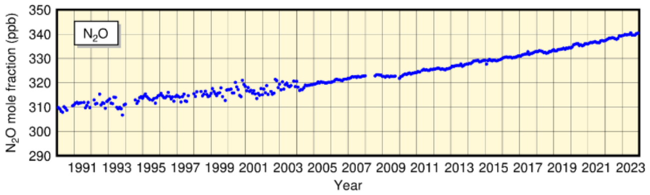

Figure 2.1-14 Monthly mean concentrations of atmospheric N_2O at Ryori
Improvement of observation equipment in 2004 resulted in improved stability of measurements.

2.1.4 Concentration of halocarbons

Halocarbons are generally carbon compounds containing halogens such as chlorine and bromine, many of which are powerful greenhouse gases whose atmospheric concentrations have increased rapidly since the second half of the 20th century due to artificial production. Although their atmospheric concentrations are only around a millionth those of CO_2, their greenhouse effect per unit mass is several thousand times greater.

Chlorofluorocarbons (CFCs; CFC-11, CFC-12 and CFC-113 among others), which are compounds of carbon, fluorine and chlorine, are ozone-depleting substances (ODSs). They are regulated under the 1987 Montreal Protocol on Substances that Deplete the Ozone Layer and its Amendments and Adjustments.

Hydrofluorocarbons (a halocarbon variety consisting of carbon compounds containing fluorine and hydrogen, referred to here as HFCs) have no effects on stratospheric ozone depletion and have been used as substitutes for CFCs. However, the Kigali Amendment of 2016 added HFCs to the list of substances subject to regulation under the Montreal Protocol (effective as of 2019) due to their significant greenhouse effects.

(1) Global concentration of halocarbons

Global concentrations of atmospheric CFCs increased rapidly until the 1980s before entering a decreasing trend in the 1990s (Figure 2.1-15). The concentration of CFC-11 peaked in 1992 – 1994, and has since shown a decreasing tendency. The concentration of CFC-12 increased until around 2003, and has also since shown a decreasing tendency. The concentration of CFC-113 reached its maximum in around 1993 in the Northern Hemisphere and around 1996 in the Southern Hemisphere. Differences in the concentrations of these gases between the Northern Hemisphere, where most emissions sources are located, and the Southern Hemisphere, which has significantly fewer sources, have decreased since the 1990s in contrast to the situation of the 1980s. These observations indicate that the CFC emission controls under the Montreal Protocol have been effective.

However, a slowdown in the decline of CFC-11 concentrations has been observed since 2012, with a rate of decrease approximately two thirds of that seen from 2002 to 2012. Results from numerical model calculation suggest that this is attributable to increased global CFC-11 emissions with main sources probably located in eastern Asia (WMO, 2018a; WMO, 2018b; Montzka *et al.*, 2018; Rigby *et al.*, 2019). Since 2018, ground-based observations and numerical model calculation results have suggested a resumed trend of decline in CFC-11 emissions from East Asia (Park *et al.*, 2021), and global ground-based observations have also shown an accelerated decrease in the growth rate of atmospheric CFC-11 concentrations since 2019 (Montzka *et al.*, 2021).

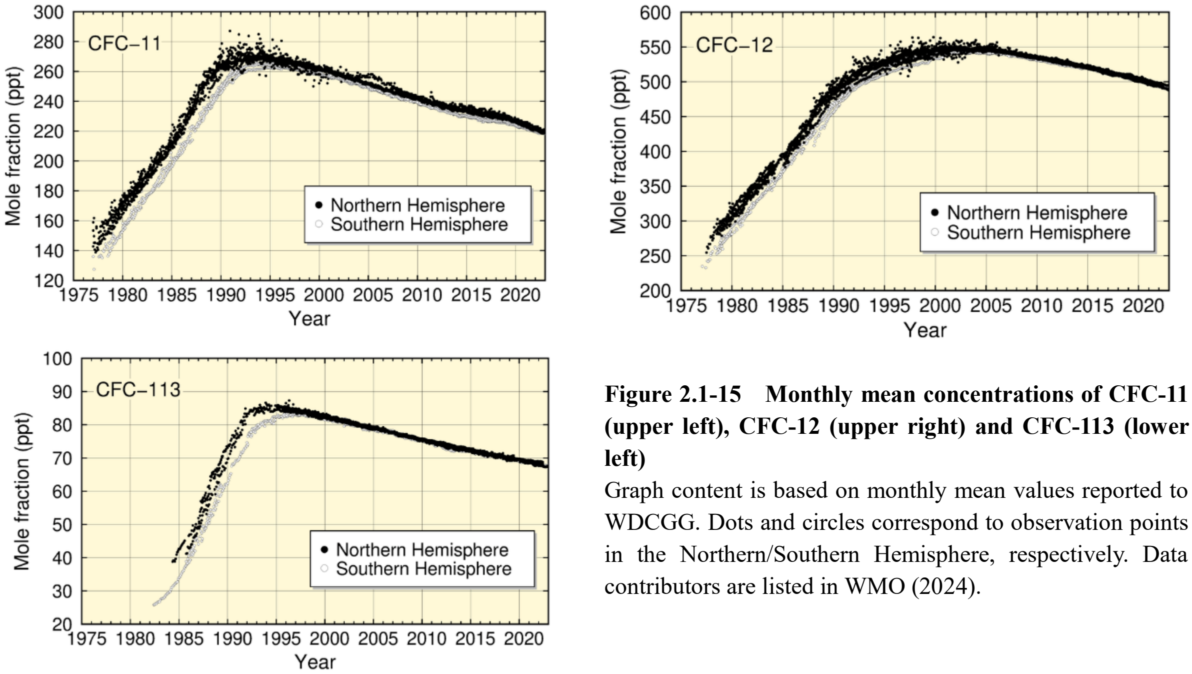

Figure 2.1-15 Monthly mean concentrations of CFC-11 (upper left), CFC-12 (upper right) and CFC-113 (lower left)

Graph content is based on monthly mean values reported to WDCGG. Dots and circles correspond to observation points in the Northern/Southern Hemisphere, respectively. Data contributors are listed in WMO (2024).

As with CFCs, atmospheric concentrations of HFCs are higher in the Northern Hemisphere, where there are more emissions sources than in the Southern Hemisphere (Figure 2.1-16). Atmospheric concentrations of HFC-134a continue to increase, while those of HFC-152a have levelled off in recent years. The difference of atmospheric concentrations of HFC-152a between the Northern Hemisphere and the Southern Hemisphere is large due to its short atmospheric lifetime and atmospheric concentrations of HFC-152a show remarkable seasonal variations.

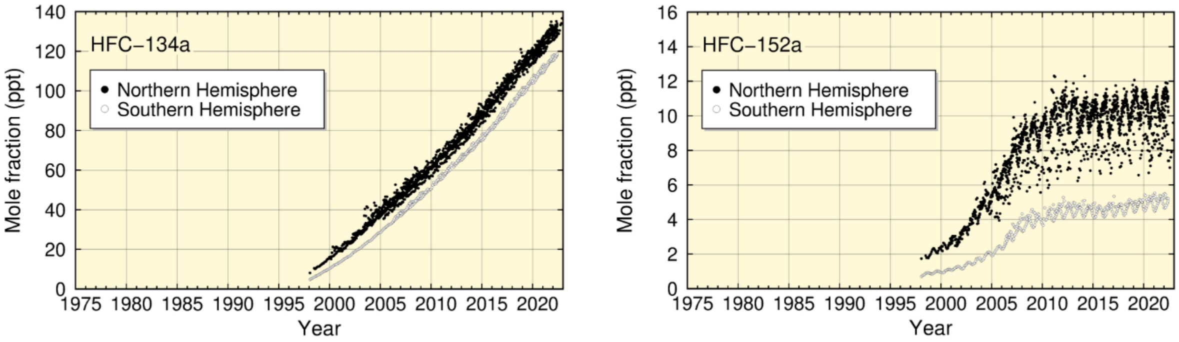

Figure 2.1-16 Monthly mean concentrations of HFC-134a (left) and HFC-152a (right)

The dataset and analysis method are as per Figure 2.1-15.

(2) Concentrations of halocarbons in Japan

Concentrations of CFC-11, CFC-12 and CFC-113 at Ryori have shown decreasing tendencies since reaching maxima in various years (Figure 2.1-17). The concentration of CFC-11 peaked at about 270 ppt in 1993 – 1994, and has since decreased. The distinct peak of concentration observed in 2011 is considered attributable to emissions from polyurethane foam insulation materials released by the Great East Japan Earthquake and the subsequent hugely destructive tsunami of 11 March 2011 (Saito *et al.*, 2015). The rate of increase in CFC-12 concentration slowed around 1995, and a gradual decrease has been seen since 2005. There was no clear tendency of increase or decrease in the concentration of CFC-113 until 2001, but a decreasing tendency has been seen since then.

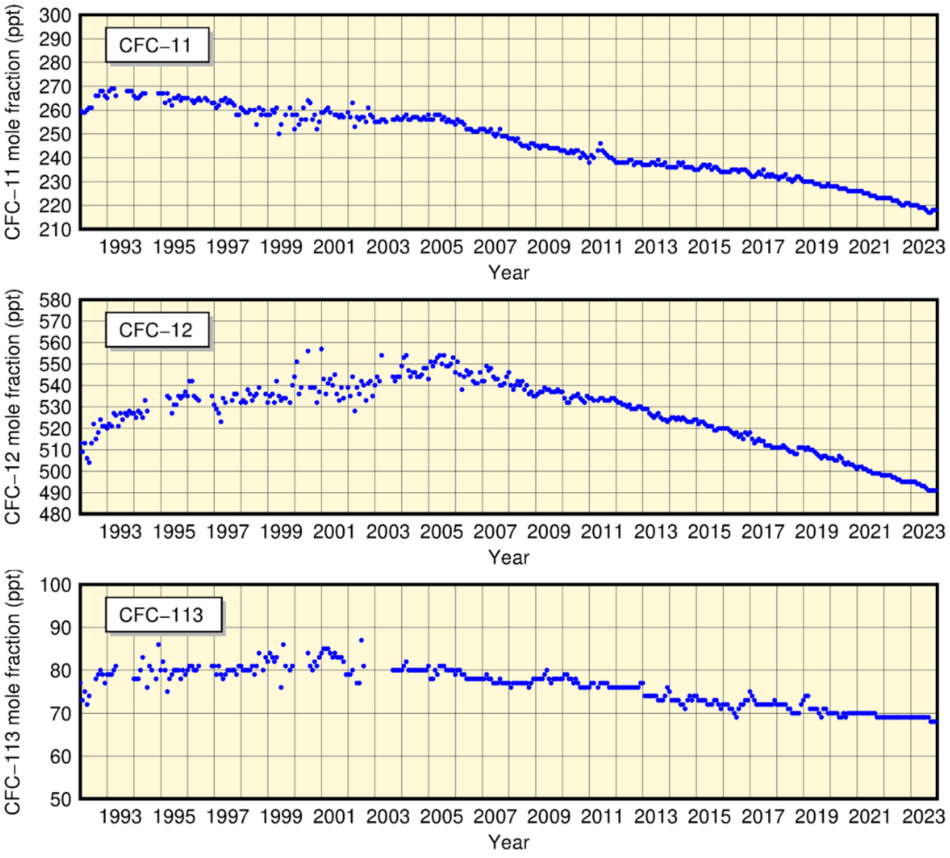

Figure 2.1-17 Monthly mean atmospheric concentrations of CFC-11 (top), CFC-12 (middle) and CFC-113 (bottom) at Ryori

Improvement of observation equipment in September 2003 resulted in improved stability of measurements.

The Japan Meteorological Agency began observing atmospheric HFC concentrations at Minamitorishima in April 2020. The results show that values for HFC-134a and HFC-152a are similar to those at other observation sites in the Northern Hemisphere in the context of global observation (Figure 2.1-18). In particular, atmospheric concentrations of HFC-152a show remarkable seasonal variations with higher concentrations from winter to spring and lower concentrations from summer to fall. Against this background, ongoing long-term monitoring is considered important.

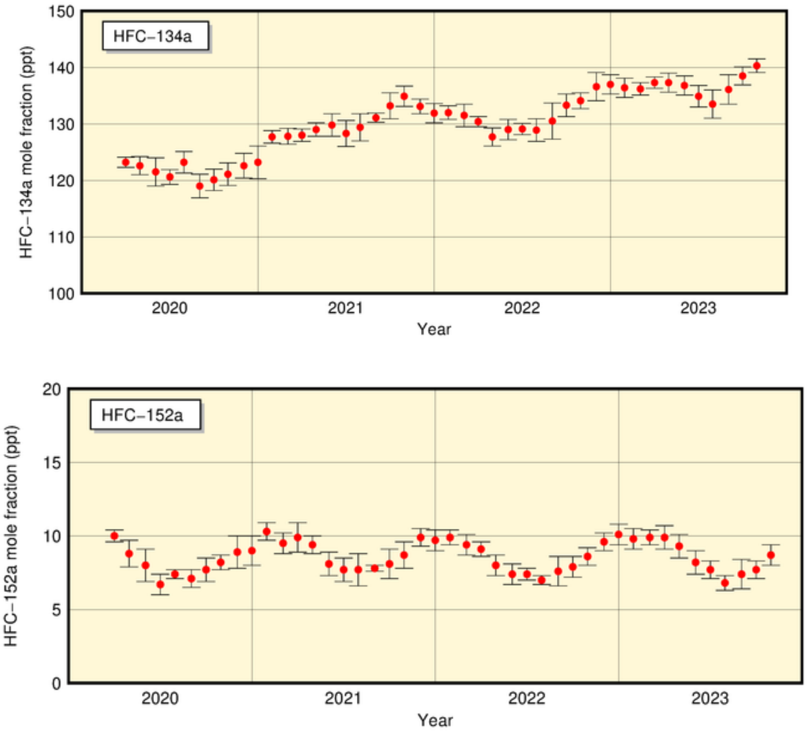

Figure 2.1-18 Monthly mean atmospheric concentrations of HFC-134a (top) and HFC-152a (bottom) at Minamitorishima

Observation of atmospheric HFC concentrations was started in April 2020 at Minamitorishima.

2.2 Aerosols and surface radiation[16]

○ Background atmospheric turbidity coefficients (which depend on concentrations of aerosols, water vapor and other variables) in Japan from 1960 onward show several local maxima up to the early 1990s due to aerosol-related high turbidity in the stratosphere from large-scale volcanic eruptions. These coefficients as of 2023 have returned approximately to the levels seen before the 1963 eruption of Mt. Agung.

○ The number of days when any meteorological station in Japan observed Kosa was 14 in 2023, and the total number of stations reporting its occurrence during the year was 40.

2.2.1 Aerosols

Interannual variations in atmospheric turbidity coefficients[17] from 1960 onward, as calculated from direct solar radiation[18] measurements taken at five stations in Japan excluding the fluctuation component of the troposphere, show clear impacts of stratospheric aerosols resulting from volcanic eruptions (Figure 2.2-1). The increased turbidity coefficients observed for several years after 1963 and during the periods of 1982 – 1983 and 1991 – 1993 were caused by the eruptions of Mt. Agung (Indonesia) in 1963, Mt. El Chichón (Mexico) in 1982 and Mt. Pinatubo (Philippines) in 1991, respectively. The increased turbidity stems from the persistent presence of sulfate aerosol in the stratosphere resulting from huge amounts of sulfur dioxide (SO_2) released by the volcanic eruptions. The turbidity coefficient has now returned to approximately the same level as that observed before the eruption of Mt. Agung because no large-scale eruptions have occurred since that of Mt. Pinatubo.

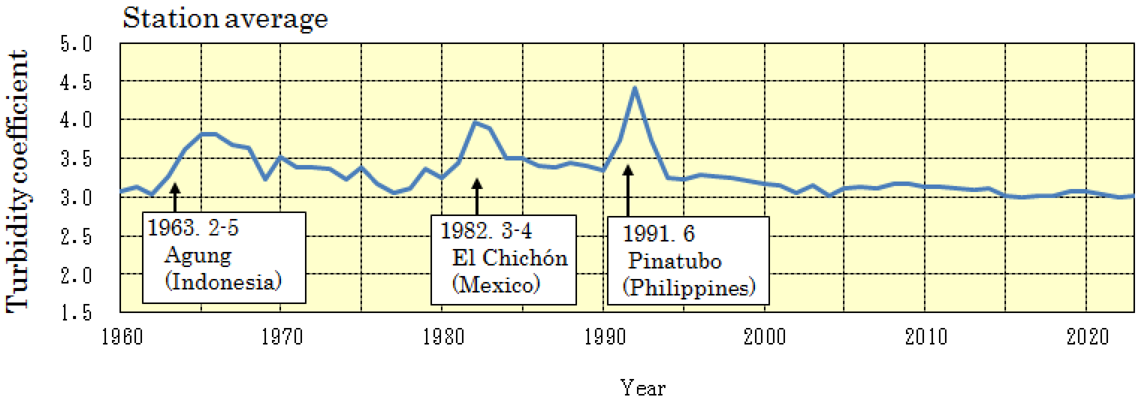

Figure 2.2-1 Time-series representation of annual mean atmospheric turbidity coefficients (1960 – 2023)
To eliminate the influence of variations in tropospheric constituents such as water vapor, dust and air pollutants, the annual mean atmospheric turbidity coefficient is calculated using the minimum turbidity coefficient for each month. Arrows indicate significant volcanic eruptions.

---

[16] See the Glossary for terms relating to aerosols. Information on surface radiation and Kosa is published on JMA's website.
https://www.data.jma.go.jp/env/kosahp/en/kosa.html (Aeolian Dust (Kosa))
https://www.data.jma.go.jp/env/radiation/en/info_rad_e.html (Solar and Infrared Radiation)

[17] The atmospheric turbidity coefficient indicates the ratio of the atmospheric optical depth affected by aerosols, water vapor and trace gases in the atmosphere to that uninfluenced by constituents other than air molecules such as oxygen and nitrogen in the atmosphere. Larger values indicate greater amounts of turbid matter in the air.

[18] Direct solar radiation is the incident solar energy acting on the earth's surface from the sun. The atmospheric turbidity coefficient (also known as the Feussner-Dubois turbidity coefficient) can be calculated from direct solar radiation amounts.

2.2.2 *Kosa (Aeolian dust)*

Kosa (Aeolian dust) is a kind of aerosol blown up from semi-arid areas of the Asian continent and transported by westerly winds to Japan. A total of 11 JMA meteorological stations (as of 31 December 2023) perform Kosa monitoring. The phenomenon is recorded when visually observed by station staff. The number of days when any meteorological station in Japan observed Kosa was 14 in 2023 (Figure 2.2-2), and the total number of stations reporting its occurrence during the year was 40 (Figure 2.2-3).

Both the number of days on which Kosa was observed and the annual total number of stations reporting observation show large interannual variability but no discernible trend between 1967 and 2023.

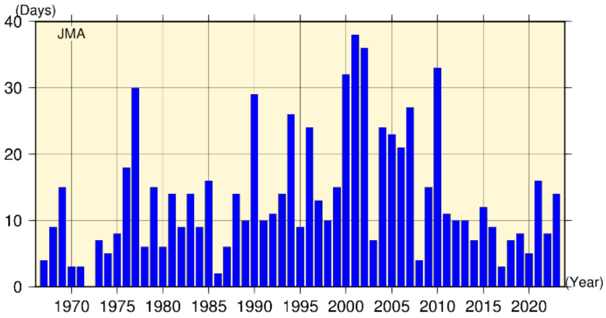

Figure 2.2-2 Number of days when any station in Japan observed Kosa (1967 – 2023) based on the 11 stations that were active for the whole period

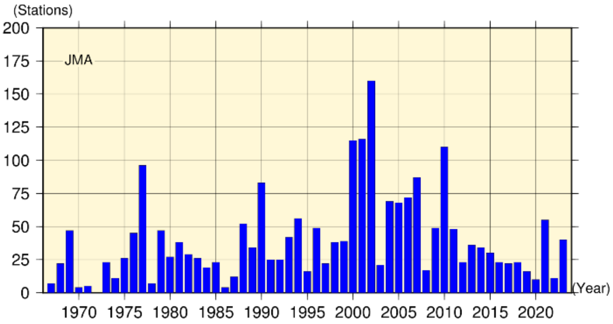

Figure 2.2-3 Annual total number of stations observing Kosa in Japan (1967 – 2023) based on the 11 stations that were active for the whole period

2.2.3 *Solar radiation and downward infrared radiation*

The earth’s radiation budget is a source of energy for climate change, and monitoring of its variations is important. To this end, JMA conducts measurements of direct solar radiation, diffuse solar radiation and downward infrared radiation[19] at five stations in Japan (Abashiri, Tsukuba, Fukuoka, Ishigakijima and Minamitorishima) (Figure 2.2-4).

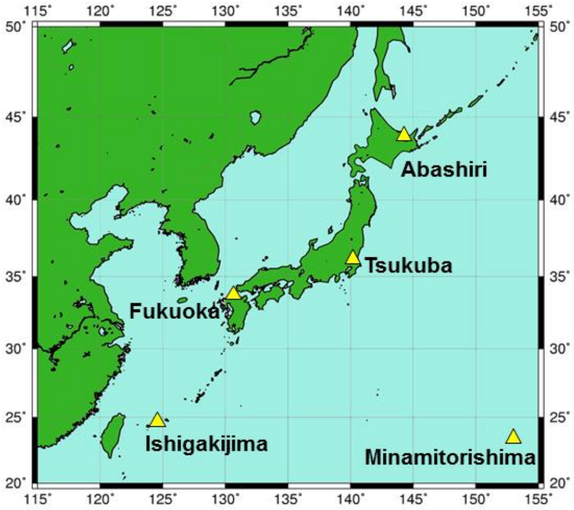

Figure 2.2-4 JMA’s solar radiation and infrared radiation observation network

JMA conducts observation of direct solar, diffuse solar and downward infrared radiation at five stations (Abashiri, Tsukuba, Fukuoka, Ishigakijima and Minamitorishima) as of 2023.

---

[19] Downward infrared radiation is the incident infrared radiation acting on the earth’s surface from all directions in the sky. It is emitted from clouds and atmospheric constituents such as water vapor and carbon dioxide in proportion to the fourth power of their temperature, and can be used as an index of global warming.

(1) Global solar radiation

Reports indicate that global solar radiation[20] decreased from around 1960 to the late 1980s before increasing rapidly from the late 1980s to around 2000, and no obvious changes have been observed in most regions of the world (Ohmura, 2009). In Japan, global solar radiation declined from the late 1970s to around 1990 before increasing from around 1990 to the early 2000s. Since then, data from measurements at the five observation stations show no obvious changes. These long-term variations are consistent with those reported globally (Figure 2.2-5).

Variations are considered to stem mainly from changes in anthropogenic aerosols in the atmosphere, and to be partly attributed to changes in cloud cover and cloud characteristics (Wild, 2009). Norris and Wild (2009) quantitatively estimated the cause of the increase in global solar radiation observed in Japan from around 1990 to the beginning of the 2000s. According to their estimates, two thirds of the increase was due to reduced anthropogenic aerosols in the atmosphere and the other third was due to reduced cloud cover. These results imply that the presence of anthropogenic aerosols has a profound effect on solar radiation variations. Results produced by Kudo et al. (2012) indicated that the solar radiation increase was mainly caused by changes in the optical characteristics of aerosols due to changes in the aerosol composition of the atmosphere.

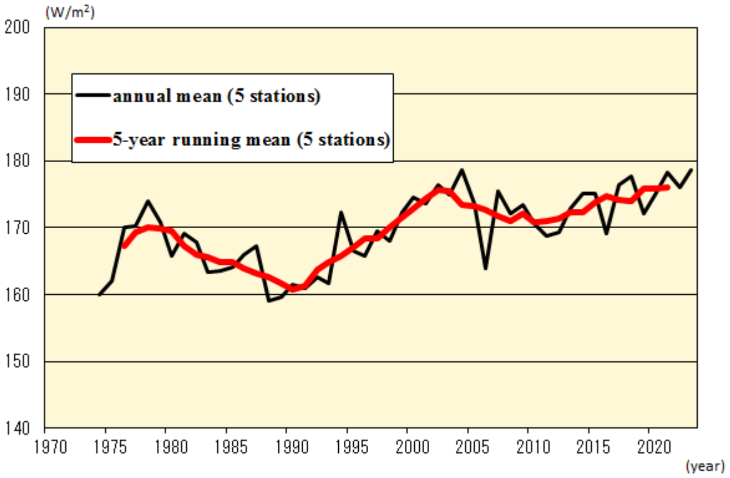

Figure 2.2-5 Time-series representations of annual (black line) and five-year-running (red line) means of global solar radiation at five stations in Japan (Abashiri, Tsukuba, Fukuoka, Ishigakijima and Minamitorishima)
Annual means are based only on monthly mean calculation from more 20 daily datasets. Before March 2010 (before February 2021 at Abashiri and before December 1987 at Tsukuba), observation was global pyranometer-based, while values have since been derived from the sum of direct and diffused pyranometer observations.

(2) Downward infrared radiation

Atmospheric concentrations of carbon dioxide and other greenhouse gases, which cause global warming, show increasing yearly trends. Observation of downward infrared radiation is effective for the evaluation of global warming because signals of global warming due to increased greenhouse gases are seen more clearly from

---

[20] Global solar radiation is the total incident solar energy arriving on a horizontal plane from all directions in the sky, and is the sum of direct solar radiation and diffuse solar radiation (the incident solar energy, except from the direction of the sun, acting on the earth's surface after being scattered by the atmosphere and clouds from all directions in the sky). It is observed either with a pyranometer or as the sum of direct and diffused pyranometer observation results. Data from the latter method are used as much as possible in Figure 2-2.5.

increased downward infrared radiation than from increased surface temperatures. While general circulation model experiments suggest that two decades of downward infrared radiation monitoring are necessary to detect statistically significant increases with a confidence level of 95%, analysis of in situ observation data covering about a decade has shown an overall increase (Wild and Ohmura, 2004).

In Japan, downward infrared radiation has been monitored since the early 1990s at Tsukuba. Analysis of the data obtained shows an increasing trend at a rate of about 0.3 W/m^2 per year during the period from 1993 to 2023 (Figure 2.2-6). This is consistent with the trend seen in the results of analysis using data from 20 BSRN[21] stations worldwide (+0.3 W/m^2 per year during the period from 1992 to 2009) (WCRP, 2010).

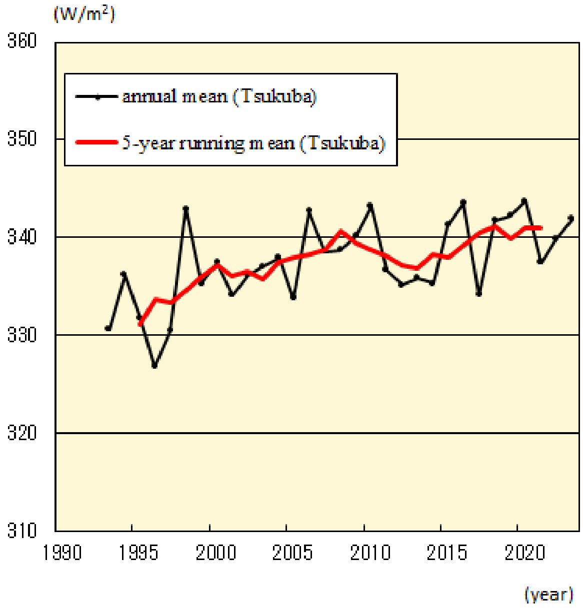

Figure 2.2-6 Time-series representations of annual (black line) and five-year-running (red line) means of downward infrared radiation at Tsukuba

---

[21] The BSRN (Baseline Surface Radiation Network) is a global observation network for measuring high-precision surface radiation balance on an ongoing basis. JMA operates five BSRN stations in Japan (Abashiri, Tsukuba, Fukuoka, Ishigakijima and Minamitorishima) and one in Antarctica (Syowa Station).

2.3 Temperature[22]

- ○ The annual anomaly of the global average surface temperature in 2023 was +0.54ºC, the highest since 1891. On a longer time scale, it is virtually certain that the annual global average surface temperature has risen at a rate of 0.76ºC per century.
- ○ The annual anomaly of the average temperature over Japan in 2023 was +1.29ºC, the highest since 1898. On a longer time scale, it is virtually certain that the annual average temperature over Japan has risen at a rate of 1.35ºC[23] per century.
- ○ It is virtually certain that the annual number of days with maximum temperatures of 35 ºC or higher ($T_{max} \geq 35$ºC) and that with minimum temperatures of 25ºC or higher ($T_{min} \geq 25$ºC) have increased, while the annual number of days with minimum temperatures below 0ºC ($T_{min} < 0$ºC) has decreased.

2.3.1 Global surface temperature

The annual anomaly of the global average surface temperature in 2023 (i.e., the combined average of the near-surface air temperature over land and the SST) was +0.54ºC above the 1991 – 2020 average. This was the highest since 1891 (Figure 2.3-1). The years from 2014 to 2023 were the top-ten warmest on record in terms of global temperature. The global average temperature fluctuates on different time scales ranging from years to decades. On a longer time scale, it is virtually certain that the global average surface temperature has risen at a rate of 0.76ºC per century[24] (statistically significant at a confidence level of 99%[25]).

The surface temperature anomalies over the Northern Hemisphere and the Southern Hemisphere were +0.68ºC (the highest) and +0.38ºC (the highest) above the 1991 –2020 average, respectively (Figure 2.3-2). It is virtually certain that average surface temperatures over the Northern Hemisphere and the Southern Hemisphere have risen at rates of 0.80ºC and 0.69ºC per century, respectively (both statistically significant at a confidence level of 99%).

Linear temperature trends for 5° × 5° latitude/longitude grid boxes indicate that most areas of the world have experienced long-term warming (Figure 2.3-3).

---

[22] Monthly, seasonal and annual estimates of mean temperatures averaged over the globe and Japan are published on JMA's website.
https://www.data.jma.go.jp/cpdinfo/temp/index.html (Japanese)
https://www.data.jma.go.jp/tcc/tcc/products/gwp/gwp.html (English)

[23] The degree of increase per century was +1.30°C until 2022 and increased to +1.35°C for this period (up to 2023) with the record-high temperature of 2023. However, this can be considered insignificant because the value has a standard error of ±0.10.

[24] IPCC AR6 (IPCC, 2021) reported that the global surface temperature from 2001 to 2020 was 0.99°C (with a very likely assessment range of 90 – 100%, or a 90% interval, of 0.84 – 1.10°C) higher than the period from 1850 to 1900. IPCC AR6 values and those in this report show no remarkable difference in rise on a long-term time scale but have been higher since the mid-1990s. Exact correspondence is not observed due to calculation differences and the statistical period examined.

[25] For evaluation and clarification of the significance statistics used here, see "Explanatory note on detection of statistical significance in long-term trends" at the end of the report.

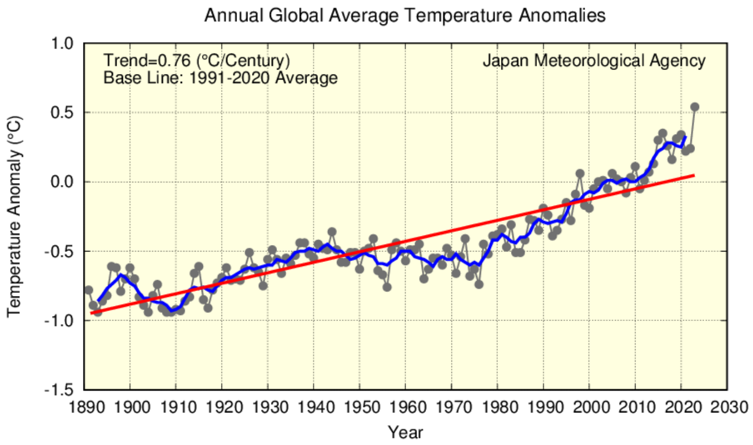

Figure 2.3-1 Annual anomalies in the global surface temperature (i.e., the combined average of the near-surface air temperature over land and the SST) from 1891 to 2023 Anomalies are deviations from the baseline (i.e., the 1991 – 2020 average). The black dots indicate annual surface temperature anomalies, the blue line indicates the five-year running mean, and the red line indicates the long-term linear trend.

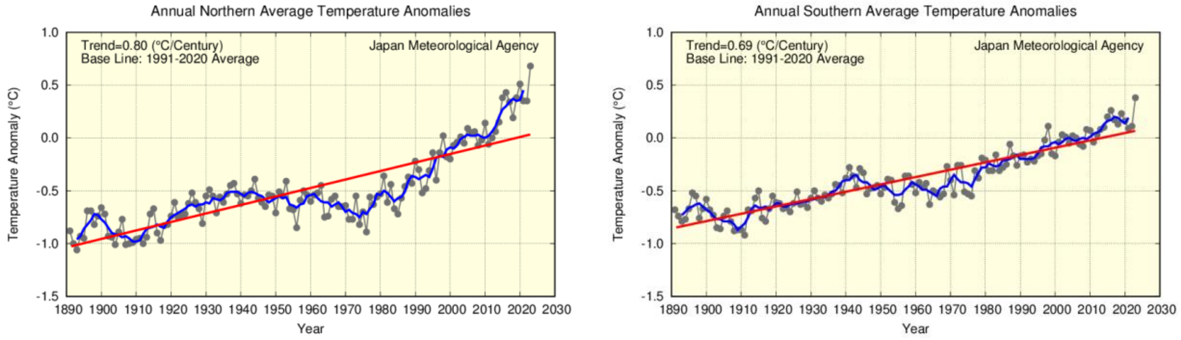

Figure 2.3-2 Annual anomalies in surface temperature (i.e., the combined average of the near-surface air temperature over land and the SST) from 1891 to 2023 for the Northern Hemisphere (left) and for the Southern Hemisphere (right)

Anomalies are deviations from the baseline (i.e., the 1991 – 2020 average). The thin black line with dots indicates surface temperature anomaly for each year. The blue line indicates the five-year running mean, and the red line indicates the long-term linear trend.

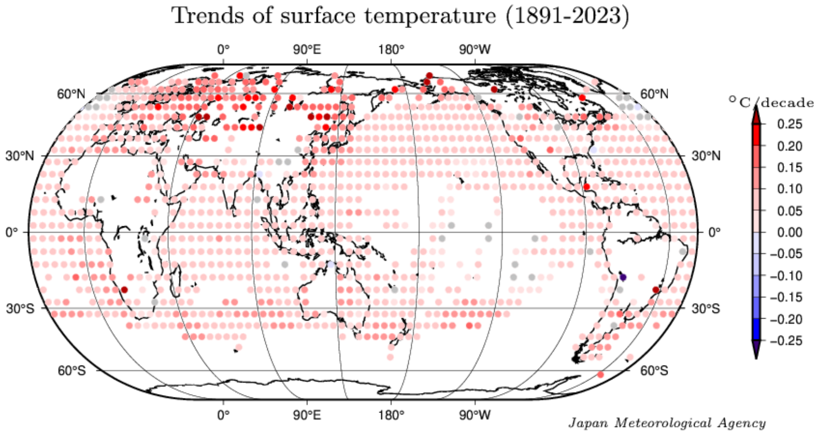

Figure 2.3-3 Linear temperature trends for 5° × 5° latitude/longitude grid boxes for the period of 1891 to 2023

The grid boxes with gray circles have no statistically significant trend (not statistically significant at a confidence level of 90%). Blank areas indicate those with insufficient data to analyze long-term trends.

2.3.2 Surface temperature over Japan

Long-term changes in the surface temperature over Japan are analyzed using observational records dating back to 1898. Table 2.3-1 lists the meteorological stations whose data are used to derive annual mean surface temperatures.

Table 2.3-1 Observation stations whose data are used to calculate surface temperature anomalies over Japan
Miyazaki and Iida were relocated in May 2000 and May 2002, respectively, and their temperatures have been adjusted to eliminate the influence of the relocation.

Element	Observation stations
Temperature (15 stations)	Abashiri, Nemuro, Suttsu, Yamagata, Ishinomaki, Fushiki, Iida, Choshi, Sakai, Hamada, Hikone, Tadotsu, Miyazaki, Naze, Ishigakijima

The mean surface temperature in Japan for 2023 is estimated to have been + 1.29ºC above the 1991 – 2020 average, which is the highest since 1898 (Figure 2.3-4). The surface temperature fluctuates on different time scales ranging from years to decades. On a longer time scale, it is virtually certain that the annual mean surface temperature over Japan has risen at a rate of 1.35ºC per century (statistically significant at a confidence level of 99%). Similarly, it is virtually certain that the seasonal mean temperatures for winter, spring, summer and autumn have risen at rates of about 1.19, 1.62, 1.25 and 1.36ºC per century, respectively (all statistically significant at a confidence level of 99%).

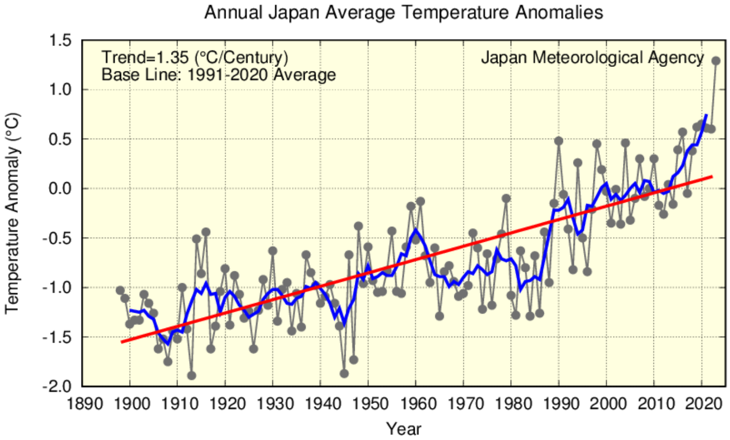

Figure 2.3-4 Annual surface temperature anomalies from 1898 to 2023 in Japan
Anomalies are deviations from the baseline (i.e., the 1991 – 2020 average). The thin black line indicates the surface temperature anomaly for each year. The blue line indicates the five-year running mean, and the red line indicates the long-term linear trend.

2.3.3 Long-term trends of extreme temperature events in Japan

This section describes long-term trends of extremely high/low-temperature events in Japan, as derived from analysis of temperature records from the 15 observation stations. Though monthly mean temperatures of the stations in Iida and Miyazaki have been adjusted to eliminate the influence of their relocation, records from these two stations are not used for analysis of daily temperatures due to the difficulty of adjustment in regard to the relocation.

(1) Long-term trends of monthly extreme temperatures

It is virtually certain that the frequency of extremely high monthly temperatures has increased during the period from 1901 to 2023, while that of extremely low monthly temperatures has decreased (Figure 2.3-5).

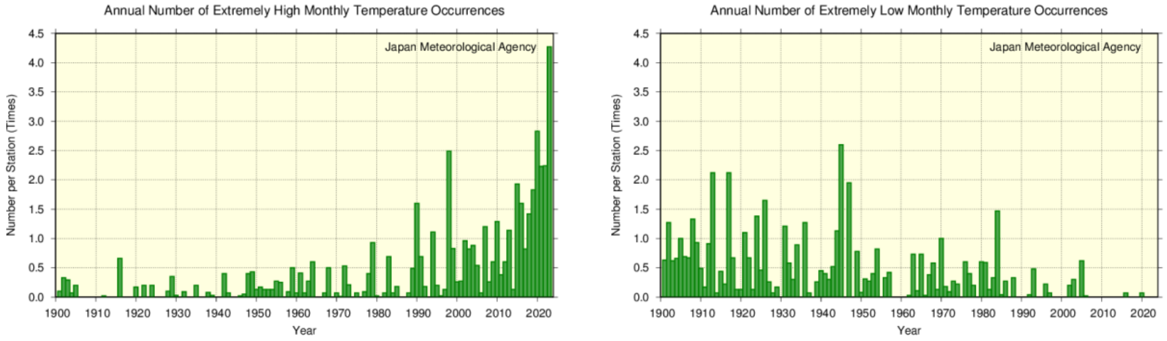

Figure 2.3-5 Annual number of extremely high/low monthly mean temperature occurrences from 1901 to 2023
The graphs show the annual number of occurrences of the highest/lowest first-to-forth values for each month. The green bars indicate annual occurrences of extremely high/low monthly mean temperatures divided by the total number of monthly observation data sets available for the year (i.e., the average occurrence per station).

(2) Annual number of days with maximum temperatures of ≥ 30°C and ≥ 35°C

The annual number of days with maximum temperatures (T_{max}) of ≥ 30°C and T_{max} ≥ 35°C is virtually certain to have increased during the period from 1910 to 2023 (both statistically significant at a confidence level of 99%) (Figure 2.3-6).

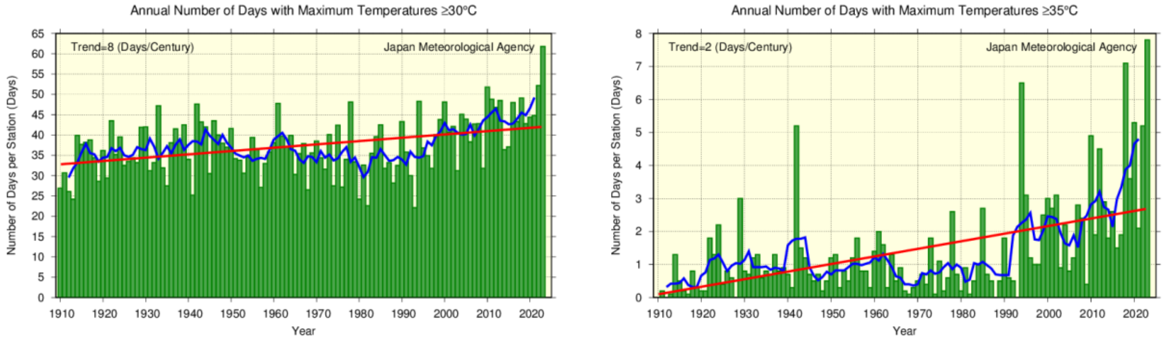

Figure 2.3-6 Annual number of days with maximum temperatures of ≥ 30°C and ≥ 35°C from 1910 to 2023
The green bars indicate the annual number of days per station for each year. The blue line indicates the five-year running mean, and the straight red line indicates the long-term linear trend.

(3) Annual number of days with minimum temperatures of < 0°C and ≥ 25°C

It is virtually certain that the annual number of days with minimum temperatures[26] (T_{min}) of < 0°C has decreased, while the annual number of days with $T_{min} \geq 25$°C has increased during the period from 1910 to 2023 (both statistically significant at a confidence level of 99%) (Figure 2.3-7).

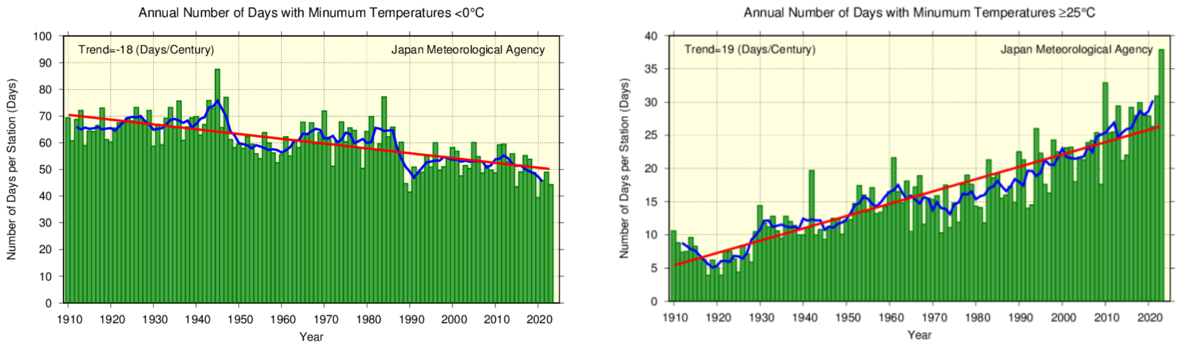

Figure 2.3-7 Annual number of days with minimum temperatures of ＜0°C and ≥ 25°C from 1910 to 2023
As per Figure 2.3-6.

2.3.4 Urban heat island effect at urban stations in Japan

The long-term trends of annual average temperatures are more pronounced for urban observation stations whose data are homogeneous over a long period (Sapporo, Sendai, Tokyo, Yokohama, Niigata, Nagoya, Kyoto, Osaka, Hiroshima, Fukuoka, Kagoshima) than for the average of the 15 rural observation stations (Table 2.3-2 and Figure 2.3-8). Although values varied by location, the rates of increase in annual mean temperatures at urban stations (by way of example) were around 0.4–1.7 ºC per century higher than the 15 station averages.

Records from urban stations whose data are not affected by relocation are used to determine long-term trends for the annual number of days with $T_{min} < 0$°C and ≥ 25°C and $T_{max} \geq 30$°C and ≥ 35°C. The number of days with $T_{min} < 0$°C is very likely to have decreased with statistical significance at all urban stations, and the number with $T_{min} \geq 25$°C, $T_{max} \geq 30$°C and $T_{max} \geq 35$°C is very likely to have increased with statistical significance at most stations except Sapporo (Table 2.3-3).

---

[26] In JMA statistics, daily maximum and minimum temperatures were observed at the daily boundary of 9:00 for the period 1953 – 1963. Systematic differences caused by a change in the daily boundary time are discussed in Fujibe (1999) and elsewhere. Estimation from monthly differences in daily minimum temperatures between the 9:00 and 24:00 daily boundaries based on observation for the period 2009 – 2020 indicates that the daily minimum temperature can be expected to be about 0.4 to 0.6°C higher than current values depending on the location and month. The number of days with Tmin < 0°C is estimated to be about 4.6 higher and that with Tmin ≥ 25°C about 0.5 lower than the values for each year in the graph (the average number of days for each of 13 locations nationwide) during the period 1953 – 1963.

Table 2.3-2 Long-term trends of annual and seasonal average temperatures at urban stations in Japan

These figures are based on data from 1927 to 2023. The trend of the 15 rural station averages (Table 2.3-1) is also listed. All results are statistically significant at a confidence level of 90%. For stations with asterisks (5 urban stations, and Iida and Miyazaki among the 15 rural stations), trends are calculated after adjustment to eliminate the influence of relocation.

Station	Long-term temperature trend (°C/century)														
	Average					Daily maximum					Daily minimum				
	Ann	Win	Spr	Sum	Aut	Ann	Win	Spr	Sum	Aut	Ann	Win	Spr	Sum	Aut
Sapporo	2.8	3.2	3.2	2.1	2.7	1.3	1.4	2.1	0.9	0.8	4.5	5.3	4.8	3.5	4.3
Sendai	2.6	2.9	3.1	1.8	2.7	1.6	1.7	2.2	1.4	1.3	3.3	3.5	3.9	2.3	3.4
Tokyo*	3.4	4.2	3.5	2.3	3.5	2.1	2.2	2.4	1.6	2.0	4.5	5.7	4.7	3.1	4.4
Yokohama	2.9	3.5	3.3	2.0	2.9	2.7	2.8	3.2	2.1	2.6	3.6	4.5	3.9	2.4	3.6
Niigata*	2.2	2.3	2.7	1.6	2.1	2.2	2.7	3.0	1.1	2.0	2.3	2.3	2.8	2.0	2.1
Nagoya	3.0	3.0	3.3	2.4	3.2	1.6	1.7	2.1	1.2	1.6	3.9	3.8	4.5	3.3	4.3
Kyoto	2.8	2.6	3.2	2.4	2.9	1.3	1.0	2.0	1.3	1.1	3.8	3.7	4.2	3.3	4.1
Osaka*	2.6	2.6	2.8	2.1	3.0	2.3	2.2	2.6	2.0	2.2	3.5	3.1	3.5	3.2	4.0
Hiroshima*	2.1	1.6	2.5	1.6	2.6	1.1	0.8	1.9	1.2	0.8	3.2	2.7	3.5	2.7	3.9
Fukuoka	3.1	2.9	3.5	2.3	3.8	1.9	1.8	2.4	1.6	1.9	4.9	4.2	5.8	3.7	6.0
Kagoshima*	2.6	2.6	2.9	2.0	2.9	1.4	1.3	1.8	1.1	1.6	3.9	3.5	4.5	3.2	4.6
15 station averages*	1.7	1.6	2.1	1.3	1.7	1.3	1.3	1.9	1.1	1.1	2.0	1.9	2.3	1.8	2.0

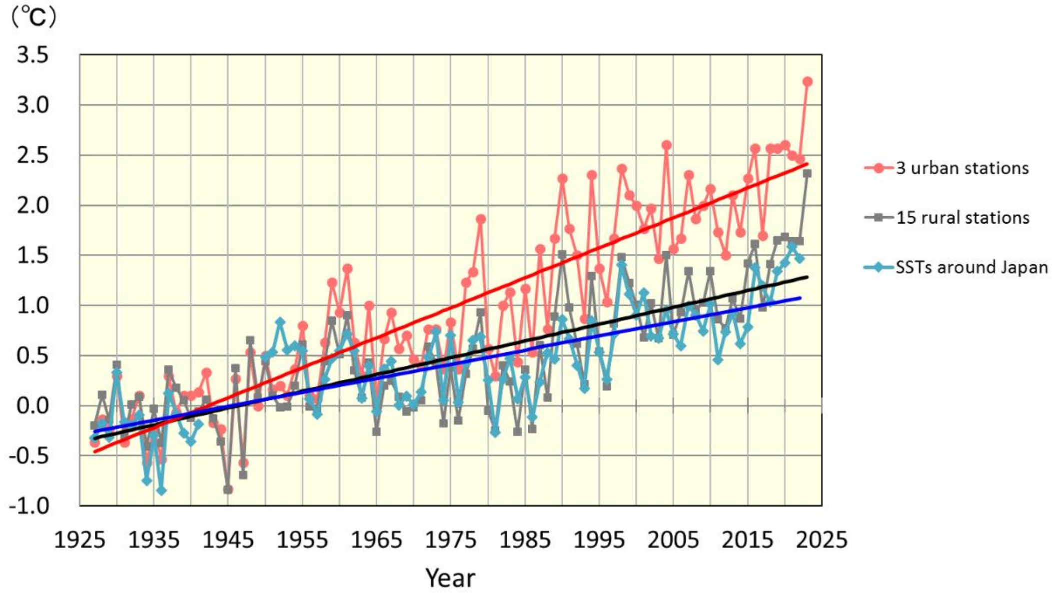

Figure 2.3-8 Annual surface temperature anomalies averaged over 3 urban stations (Tokyo, Nagoya and Osaka), 15 rural stations in Japan and annual sea surface temperature anomalies around Japan from 1927 to 2023

Anomalies are deviations from the baseline (i.e., the 1927 – 1956 average). The red line indicates average annual surface temperature anomalies over the urban stations of Tokyo, Nagoya and Osaka, and the black line indicates average annual surface temperature anomalies at each of 15 rural stations. The blue line indicates annual sea surface temperature anomalies around Japan (base data as per Figure 2.8-4). The 30-year averages from 1927 to 1956 for each anomaly equal 0, respectively.

Table 2.3-3 Long-term trends for the annual number of days with minimum temperatures of < 0°C and ≥ 25°C and maximum temperatures of ≥ 30°C and ≥ 35°C

These figures are based on data from 1927 to 2023. The trend of the 13 rural station averages (Table 2.3-1 excluding Iida and Miyazaki) is also listed. Values shown in italics are not statistically significant at a confidence level of 90%.

Station	Annual number of days			
	Trend (days/century)			
	$T_{\mathrm{min}} < 0$°C	$T_{\mathrm{min}} \geq 25$°C	$T_{\mathrm{max}} \geq 30$°C	$T_{\mathrm{max}} \geq 35$°C
Sapporo	−46	1	*4*	*0*
Sendai	−58	7	14	1
Yokohama	−58	34	24	3
Nagoya	−67	39	15	12
Kyoto	−70	39	16	16
Fukuoka	−47	49	15	12
13 station averages	−21	19	8	3

2.4 Precipitation[27]

- ○ The annual anomaly of global precipitation (for land areas only) in 2023 was -15 mm.
- ○ The annual anomaly of precipitation in 2023 was −27.8 mm in Japan. Annual precipitation over Japan shows no discernible long-term trend.
- ○ The annual number of days with daily and hourly extreme precipitation has increased in Japan, while that with wet days has decreased.

2.4.1 Global precipitation over land

Annual precipitation (for land areas only) in 2023 was 15 mm below the 1991 – 2020 average (the 57th heaviest in 123 years since 1901). Long-term trend is not shown because there is a relatively large margin of error in early statistical period due to limited observation data.

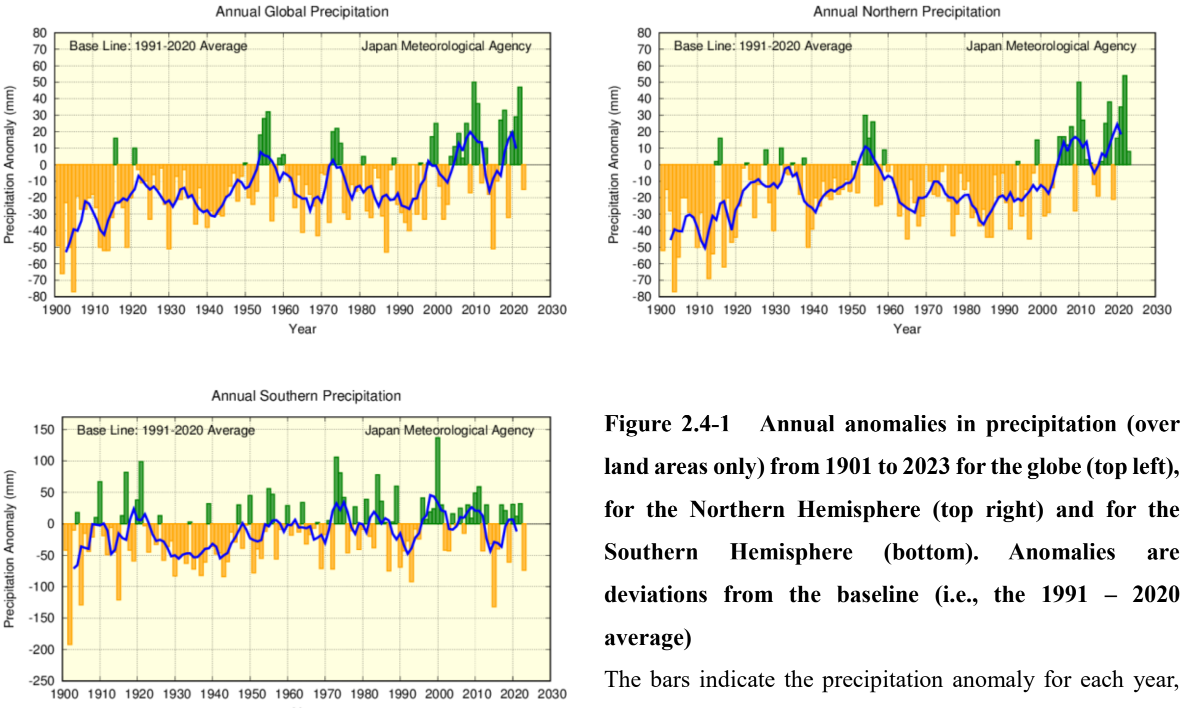

Figure 2.4-1 Annual anomalies in precipitation (over land areas only) from 1901 to 2023 for the globe (top left), for the Northern Hemisphere (top right) and for the Southern Hemisphere (bottom). Anomalies are deviations from the baseline (i.e., the 1991 – 2020 average)

The bars indicate the precipitation anomaly for each year, and the blue line indicates the five-year running mean.

2.4.2 Precipitation over Japan

This section describes long-term trends in precipitation over Japan as derived from analysis of precipitation records from 51 observation stations (Table 2.4-1).

Annual precipitation in 2023 was −27.8 mm (the 53rd lightest since 1898) above the 1991 – 2020 average (Figure 2.4-2).

---

[27] Data on annual precipitation around the world and in Japan are published on JMA’s website.

Table 2.4-1 List of 51 observation stations whose data are used to calculate precipitation anomalies and long-term trends in Japan

Element	Observation stations
Precipitation (51 stations)	Asahikawa, Abashiri, Sapporo, Obihiro, Nemuro, Suttsu, Akita, Miyako, Yamagata, Ishinomaki, Fukushima, Fushiki, Nagano, Utsunomiya, Fukui, Takayama, Matsumoto, Maebashi, Kumagaya, Mito, Tsuruga, Gifu, Nagoya, Iida, Kofu, Tsu, Hamamatsu, Tokyo, Yokohama, Sakai, Hamada, Kyoto, Hikone, Shimonoseki, Kure, Kobe, Osaka, Wakayama, Fukuoka, Oita, Nagasaki, Kumamoto, Kagoshima, Miyazaki, Matsuyama, Tadotsu, Kochi, Tokushima, Naze, Ishigakijima, Naha

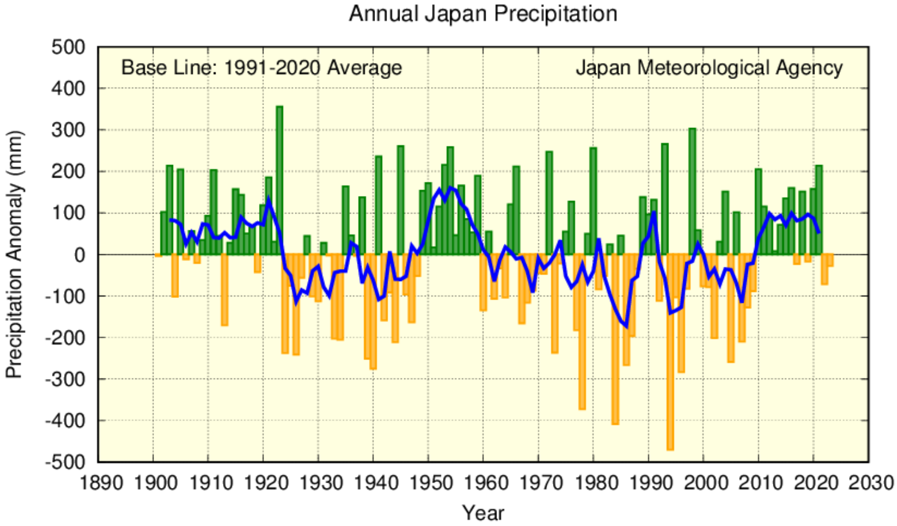

Figure 2.4-2 Annual anomalies in precipitation from 1898 to 2023 in Japan. Anomalies are deviations from the baseline (i.e., the 1991 – 2020 average)

The bars indicate the precipitation anomaly for each year, and the blue line indicates the five-year running mean.

2.4.3 *Long-term trends of extreme precipitation events in Japan*

(1) Extremely wet/dry months[28]

This part describes long-term trends in frequencies of extremely wet/dry months and heavy daily precipitation events in Japan based on analysis of precipitation data from 51 observation stations.

It is virtually certain that the frequency of extremely dry months increased (Figure 2.4-3 left). There has been no discernible trend in the frequency of extremely wet months (Figure 2.4-3 right).

---

[28] Here, judgment of extremely heavy/light precipitation is based on the fourth–highest/lowest monthly values on record over about 120-year period from 1901. The frequency of occurrence of the highest/lowest to the fourth–highest/lowest values over this period is once approximately every 30 years, which is close to JMA's definition of extreme climate events as those occurring once every 30 years or longer (See the Glossary for terms relating to Extreme climate event).

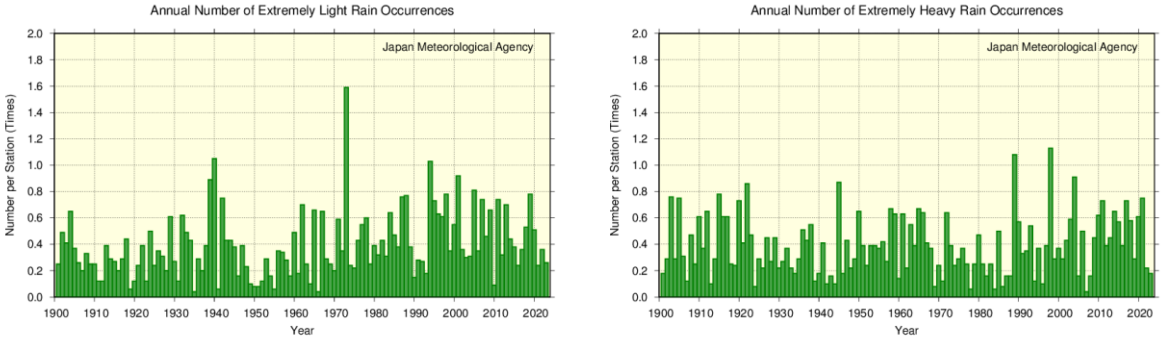

Figure 2.4-3 Annual number of extremely wet/dry months from 1901 to 2023

The graphs show the annual number of occurrences of the first-to-forth heaviest/lightest precipitation values for each month. The green bars indicate annual occurrences of extremely heavy/light monthly precipitation divided by the total number of monthly observation data sets available for the year (i.e., the average occurrence per station).

(2) Annual number of days with precipitation of ≥ 100 mm, ≥ 200 mm and < 1.0 mm

The annual number of days with precipitation of ≥ 100 mm and ≥ 200 mm are virtually certain to have increased during the period from 1901 to 2023 (both statistically significant at a confidence level of 99%) (Figure 2.4-4). The annual number of days with precipitation of < 1.0 mm (dry days) is virtually certain to have increased over the same period (statistically significant at a confidence level of 99%) (Figure 2.4-5).

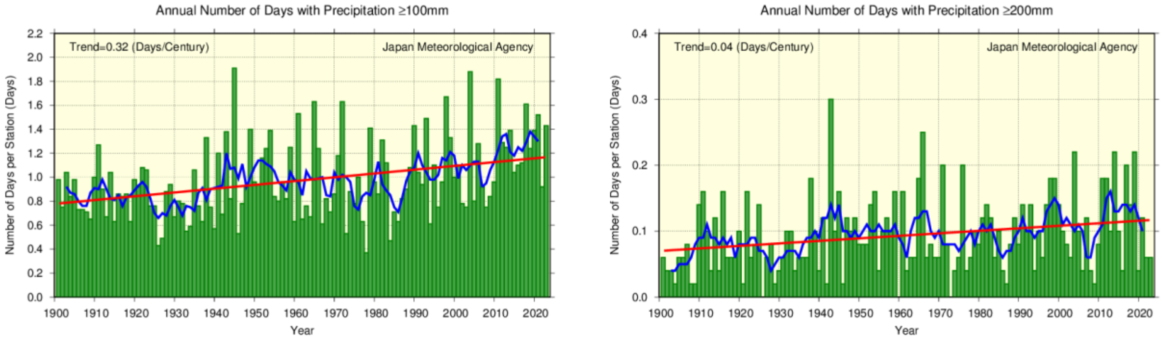

Figure 2.4-4 Annual number of days with precipitation ≥ 100 mm and ≥ 200 mm from 1901 to 2023

The green bars indicate the annual number of days per station for each year. The blue line indicates the five-year running mean, and the straight red line indicates the long-term liner trend.

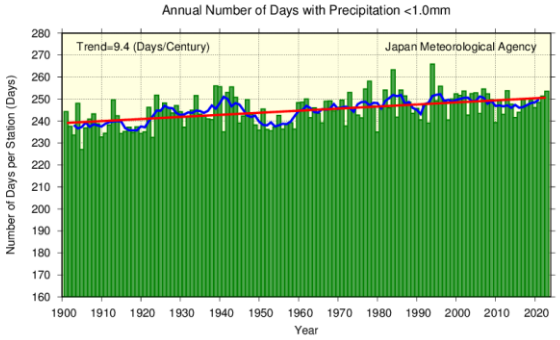

Figure 2.4-5 Annual number of days with precipitation of < 1.0 mm (dry days) from 1901 to 2023

As per figure 2.4-4.

(3) Heavy rainfall frequency based on Automated Meteorological Data Acquisition System (AMeDAS) data

JMA operationally observes precipitation at about 1,300 unmanned regional meteorological observation stations all over Japan (collectively known as the Automated Meteorological Data Acquisition System, or AMeDAS). Observation was started in the latter part of the 1970s at many points, and observation data covering the approximately 50-year period through to 2023 are available[29]. Although the period covered by AMeDAS observation records is shorter than that of Local Meteorological Observatories or Weather Stations (which have observation records for the past 120 years or so), there are around eight times as many AMeDAS stations as Local Meteorological Observatories and Weather Stations combined. Hence, AMeDAS is better equipped to capture heavy precipitation events that take place on a limited spatial scale.

It is virtually certain that annual numbers of heavy rainfall events have increased (Table 2.4-2, Figure 2.4-6). As the frequency of extreme precipitation events is low and the period covered by observation records is still relatively short, the addition of future observations to the data series is expected to increase the reliability of statistical trend detection.

---

[29] The number of AMeDAS station was about 800 in 1976, and had gradually increased to about 1,300 now. To account for these numerical differences, the annual number of precipitation events needs to be converted to a per-1,300-station basis. Data from wireless robot precipitation observation stations previously deployed in mountainous areas are also excluded.

Table 2.4-2 Changes in annual numbers of heavy rainfall events from 1976 to 2023 on AMeDAS data

Element	**Trend**	**Frequency ratio (2014 – 2023 average vs. 1976 – 1985 average)**
≥ 50 mm per hour	Virtually certain to have increased (statistically significant at a confidence level of 99%)	Approx. x 1.5 (Approx. 226 -> Approx. 330)
≥ 80 mm per hour	Virtually certain to have increased (statistically significant at a confidence level of 99%)	Approx. x 1.7 (Approx. 14 -> Approx. 24)
≥ 100 mm per hour	Extremely likely to have increased (statistically significant at a confidence level of 95%)	Approx. x 1.8 (Approx. 2.2 -> Approx. 4.0)
≥ 100 mm per 3 hours	Virtually certain to have increased (statistically significant at a confidence level of 99%)	Approx. x 1.6 (Approx. 155 -> Approx. 253)
≥ 150 mm per 3 hours	Virtually certain to have increased (statistically significant at a confidence level of 99%)	Approx. x 1.8 (Approx. 19 -> Approx. 34)
≥ 200 mm per 3 hours	Virtually certain to have increased (statistically significant at a confidence level of 99%)	Approx. x 2.0 (Approx. 2.8 -> Approx. 5.6)
≥ 200 mm per day	Extremely likely to have increased (statistically significant at a confidence level of 95%)	Approx. x 1.6 (Approx. 160 -> Approx. 251)
≥ 300 mm per day	Virtually certain to have increased (statistically significant at a confidence level of 99%)	Approx. x 2.1 (Approx. 28 -> Approx. 57)
≥ 400 mm per day	Virtually certain to have increased (statistically significant at a confidence level of 99%)	Approx. x 2.3 (Approx. 6.4 -> Approx. 15)

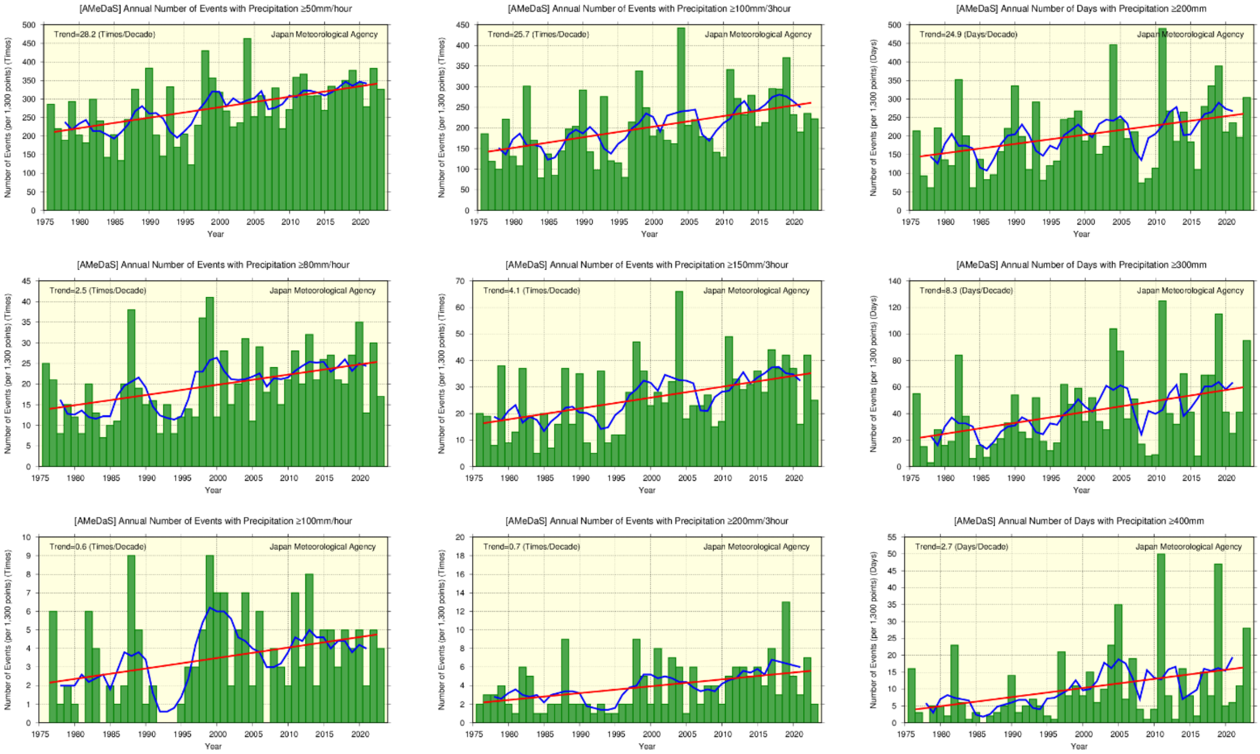

Figure 2.4-6 Annual numbers of heavy rainfall events from 1976 to 2023

Left: Events with precipitation of ≥ 50 mm (top), ≥ 80 mm (center) and ≥ 100 mm (bottom) per hour

Center: Events with precipitation of ≥ 100 mm (top), ≥ 150 mm (center) and ≥ 200 mm (bottom) per 3 hours

Right: Days with precipitation of ≥ 200 mm (top), ≥ 300 mm (center) and ≥ 400 mm (bottom)

The green bars indicate the annual number of events per 1,300 AMeDAS stations for each year. The blue line indicates the five-year running mean, and the straight red line indicates the long-term liner trend.

(4) Heavy rainfall intensity based on AMeDAS data

Changes in the intensity of annual maximum 24-, 48- and 72-hour precipitation over Japan were analyzed using data from 636 AMeDAS stations where ongoing observation was conducted from 1976 to 2023. Annual data are averages of ratios against the baseline (the 1991 – 2020 average).

It is extremely likely that annual maximum 24-, 48- and 72-hour precipitation increased at rates of 3.2%, 3.5% and 3.3% per decade (each statistically significant at a confidence level of 95%), respectively (Figure 2.4-7). As per Section (3), the addition of future observations to the data series is expected to increase the reliability of statistical trend determination.

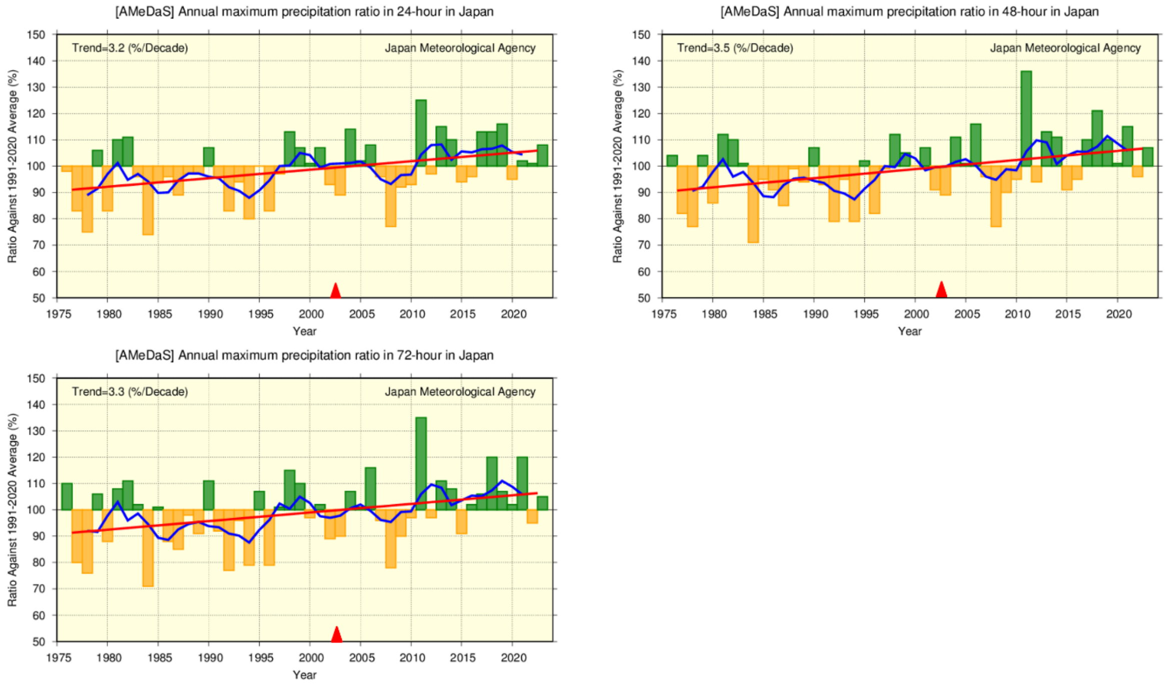

Figure 2.4-7 Annual maximum precipitation ratios (%) for 24-hour (top left) , 48-hour (top right) and 72-hour (bottom) periods over Japan for the period from 1976 to 2023

Annual averages for each year are presented as ratios against the baseline (i.e., the 1991 – 2020 average). The green and yellow bars indicate the annual maximum precipitation ratios for each year based on 636 AMeDAS stations where ongoing observation was conducted from 1976. The blue line indicates the five-year running means, and the straight red line indicates the long-term linear trend. Red triangles (▲) indicate the change in observational periodicity for hourly precipitation from every hour to every 10 minutes in 2003[30].

---

[30] As of 1 Jan. 2003, annual maximum precipitation is determined from 10-minute data as opposed to the previous hourly data. This creates a systematic difference ▲ (e.g., annual maximum daily precipitation ≥ 50 mm tends to average 8 mm more than before.)

2.5 Snow depth and snow cover

○ It is extremely likely that a decreasing trend is observed in the interannual variability of the total snow cover extent in the Northern Hemisphere for January and the period from September to December and in Eurasia for the period from January to March, June and the period from September to December.

○ In winter 2022/2023, there were more days of snow cover than normal over the western USA, and fewer over northern East Asia.

○ Snow depth on the Sea of Japan side is extremely likely to have decreased.

2.5.1 Snow cover in the Northern Hemisphere

JMA monitors snow-cover variations in the Northern Hemisphere using analysis data from satellite observations[31] based on its own algorithm. The average seasonal migration of snow cover in the Northern Hemisphere normally peaks around January – February and decreases in spring.

In the Northern Hemisphere (north of 30°N), it is extremely likely (statistically significant at a confidence level of 95%) that a decreasing trend is observed in the interannual variability of the total snow cover extent over the 36-year period from 1988 to 2023 for January and the period from September to December, while no discernible trend is seen for the period from February to August (Figure 2.5-1 (a) and (c)). In Eurasia (north of 30°N from 0° to 180°E), it is extremely likely (statistically significant at a confidence level of 95%) that a decreasing trend is observed in the interannual variability of the total snow cover for the period from January to March, June and the period from September to December, while no discernible trend is seen for the period from April to May and the period from July to August (Figure 2.5-1 (b) and (d)). In winter (December to February) 2022/2023, there were more days of snow cover than normal over the western USA, and fewer over northern East Asia (Figure 2.5-1 (e)). In November 2023, there were more days of snow cover in the northeastern China, and fewer from Western Russia to Central Asia and over northern Canada (Figure 2.5-1 (f)).

The albedo of snow-covered ground (i.e., the ratio of solar radiation reflected by the surface) is higher than that of snow-free ground. The variability of snow cover has an impact on the earth's surface energy budget and radiation balance, and therefore on the climate. In addition, snow absorbs heat from its surroundings and melts, thereby providing soil moisture and related effects on the climate system. The variability of atmospheric circulation and oceanographic conditions affects the amount of snow cover, which exhibits a close and mutual association with climatic conditions. Snow-cover variations in Eurasia and other parts of the Northern Hemisphere may affect climate conditions in Japan, but the mechanisms behind such a potential influence remain unclear. The accumulation of future observation data in addition to the current body of information and the implementation of related research are expected to increase the reliability of statistical work to identify trends of snow cover extent and help to elucidate how snow-cover variations affect climate conditions.

---

[31] The Defense Meteorological Satellite Program (DMSP) polar-orbiting satellites of the USA, equipped with the Special Sensor Microwave/Imager (SSM/I) and the Special Sensor Microwave Imager Sounder (SSMIS), and the Japan Aerospace Exploration Agency (JAXA) Global Change Observation Mission – Water (GCOM-W) satellite, equipped with the Advanced Microwave Scanning Radiometer 2 (AMSR2)

(a) February（Northern Hemisphere）

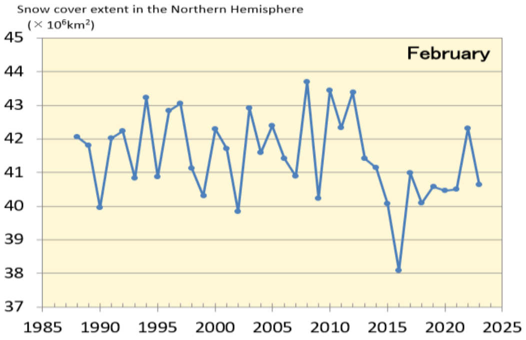

(b) February（Eurasia）

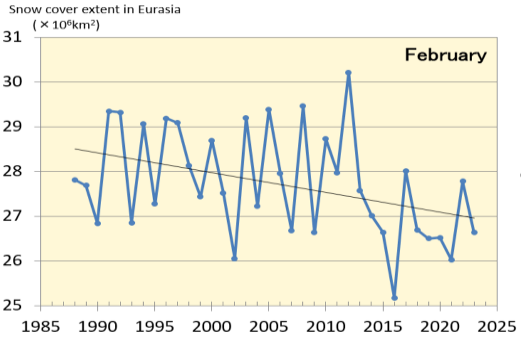

(c) November（Northern Hemisphere）

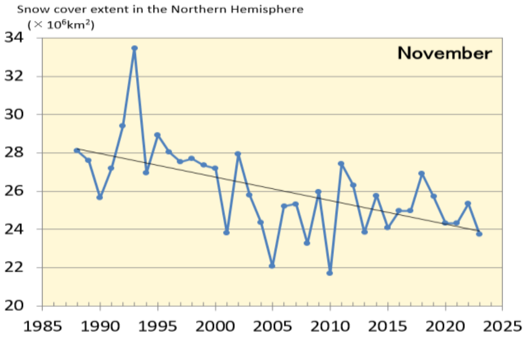

(d) November（Eurasia）

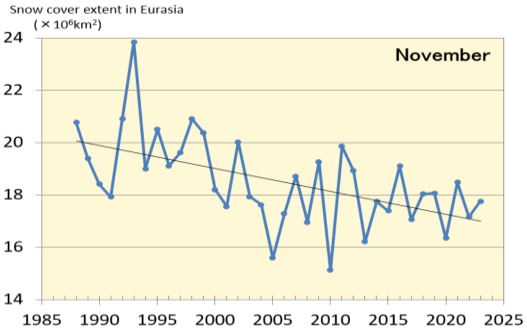

(e) February

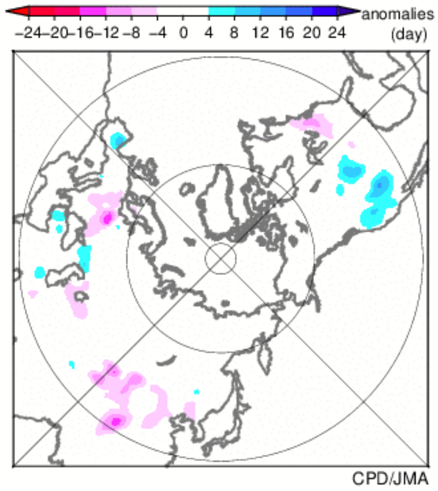

(f) November

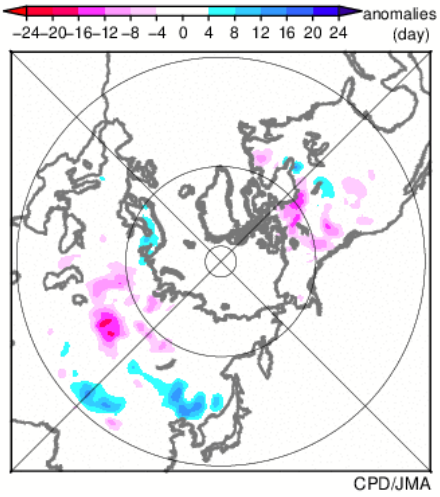

Figure 2.5-1 Interannual variations in the total area of monthly snow cover (km^2) in the Northern Hemisphere (north of 30°N) for (a) February and (c) November and in Eurasia (north of 30°N, from 0° to 180°E) for (b) February and (d) November from 1988 to 2023, and anomalies in the number of days with snow cover for (e) February and (f) November in 2023

(a) - (d): The blue lines indicate the total snow cover area for each year, and the black lines show linear trends (statistically significant at a confidence level of 95%).

(e) - (f): Blue (red) shading indicates more (fewer) days of snow cover.

The base period for the normal is 1991 – 2020.

2.5.2 Snow depth and Snowfall in Japan

(1) Annual maximum snow depth

Long-term trends in the annual maximum snow depth (represented in terms of a ratio against the 1991 – 2020 average) in Japan since 1962[32] are analyzed using observational records from stations located on the Sea of Japan coast (Table 2.5-1).

Table 2.5-1 Observation stations whose data are used to calculate snow depth ratios in Japan

Region	Observation stations
Sea of Japan side of northern Japan	Wakkanai, Rumoi, Asahikawa, Sapporo, Iwamizawa, Suttsu, Esashi, Kutchan, Wakamatsu, Aomori, Akita, Yamagata
Sea of Japan side of eastern Japan	Wajima, Aikawa, Niigata, Toyama, Takada, Fukui, Tsuruga
Sea of Japan side of western Japan	Saigo, Matsue, Yonago, Tottori, Toyooka, Hikone, Shimonoseki, Fukuoka, Oita, Nagasaki, Kumamoto

The annual maximum snow depth ratio in 2023 was 100% relative to the 1991 – 2020 average for the Sea of Japan side of northern Japan, 124% for the same side of eastern Japan, and 99% for the same side of western Japan (Figure 2.5-2). On a longer time scale, the annual maximum snow depth ratio from 1962 on each area is very likely to have decreased (statistically significant at a confidence level of 90% for the Sea of Japan side of northern Japan and 95% for the same side of eastern and western Japan).

(2) Heavy snowfall frequency

This section describes long-term trends in frequencies of heavy daily snowfall since 1962 at stations on the Sea of Japan side of Japan (Table 2.5-1).

It is very likely that the annual number of heavy snowfall events (such as ≥ 20 cm per day) has decreased for the Sea of Japan side of eastern and western Japan (statistically significant at confidence levels of 95% and 99%, respectively), while that for the Sea of Japan side of northern Japan exhibits no statistically discernible trend (Table 2.5-2, Figure 2.5-3). The average annual number of days with snowfall of ≥ 20 cm per day in each region from 2014 to 2023 was lower than that for 1962 to 1971 (Table 2.5-2).

The annual number of days with snowfall of ≥ 50 cm exhibits no statistically discernible trend for northern and western Japan (where such events occur only once every few years), possibly due to the rarity of such cases. Values for the Sea of Japan side of eastern Japan are very likely to have decreased (statistically significant at a confidence level of 95%).

As annual maximum snow depth and snowfall fluctuate greatly and the period covered by observation records is still relatively short, addition of future observations to the data series is expected to increase the reliability of statistical trend determination.

---

[32] Annual statistical data here are focused on winter (e.g., the value for 1976 is from data for August 1975 – July 1976).

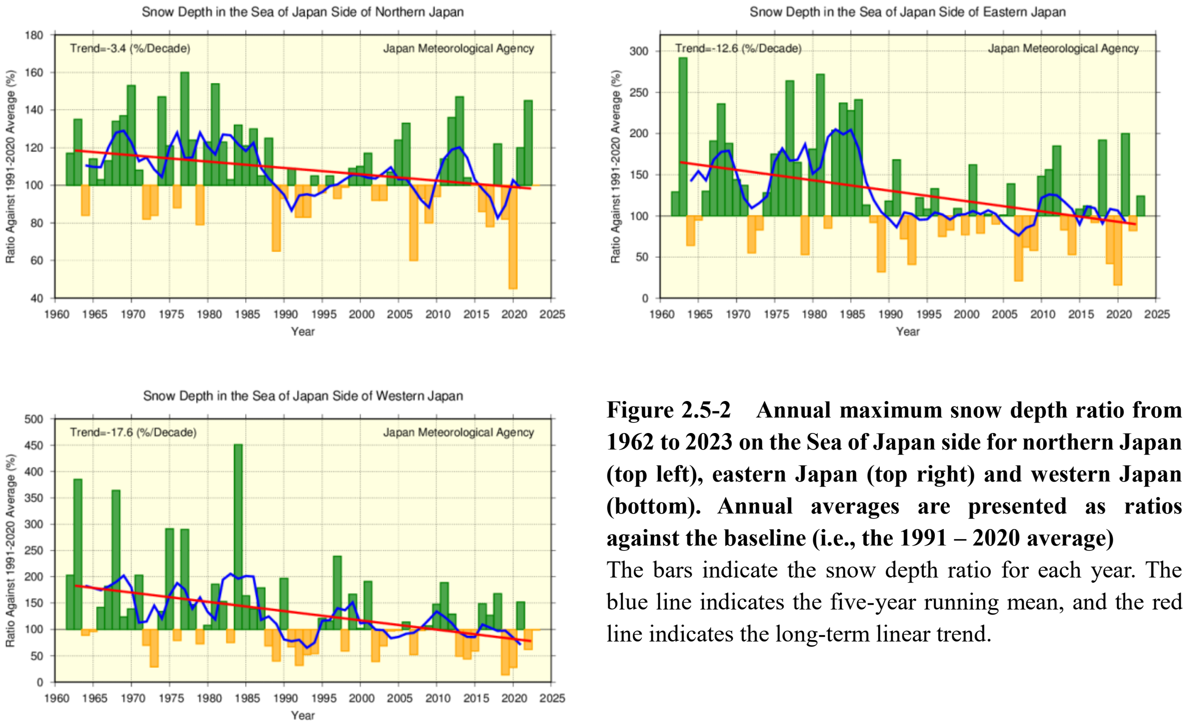

Figure 2.5-2 Annual maximum snow depth ratio from 1962 to 2023 on the Sea of Japan side for northern Japan (top left), eastern Japan (top right) and western Japan (bottom). Annual averages are presented as ratios against the baseline (i.e., the 1991 – 2020 average)

The bars indicate the snow depth ratio for each year. The blue line indicates the five-year running mean, and the red line indicates the long-term linear trend.

Table 2.5-2 Annual numbers of days with snowfall ≥ 20 cm from 1962 to 2023

Element	≥ 20 cm-per-day trend	Frequency ratio (2014 – 2023 average vs. 1962 – 1971 average)
The Sea of Japan side of northern Japan	No statistically discernible trend	Approx. x 0.8 (Approx. 4.3 -> Approx. 3.4)
The Sea of Japan side of eastern Japan	Extremely likely to have decreased (statistically significant at a confidence level of 95%)	Approx. x 0.5 (Approx. 3.9 -> Approx. 1.9)
The Sea of Japan side of western Japan	Virtually certain to have decreased (statistically significant at a confidence level of 99%)	Approx. x 0.5 (Approx. 1.1 -> Approx. 0.5)

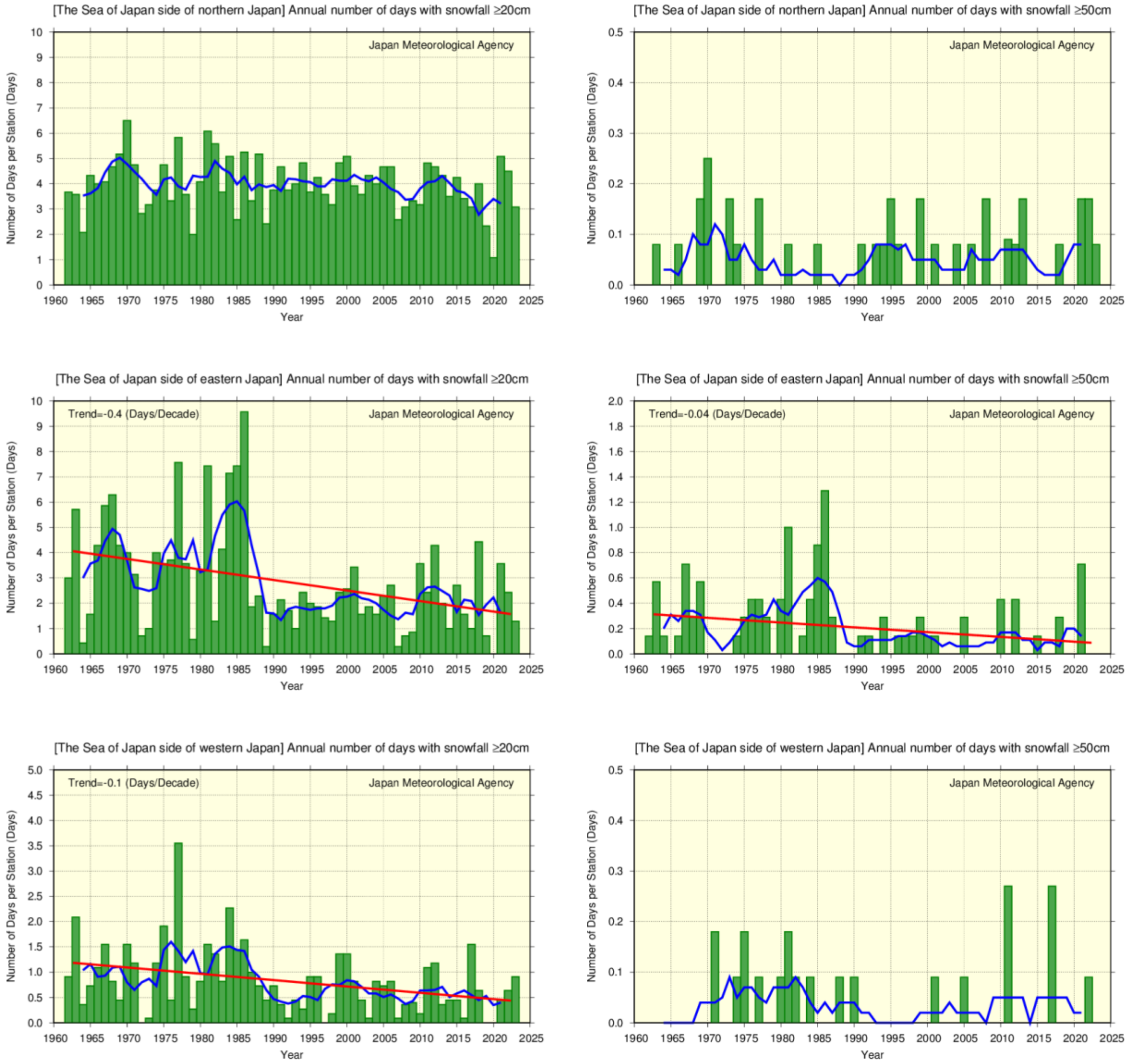

Figure 2.5-3 Annual numbers of days with snowfall of ≥ 20 cm and ≥ 50 cm per day from 1962 to 2023

Top: ≥ 20 cm (left) and ≥ 50 cm (right) for the Sea of Japan side of northern Japan

Middle: ≥ 20 cm (left) and ≥ 50 cm (right) for the Sea of Japan side of eastern Japan

Bottom: ≥ 20 cm (left) and ≥ 50 cm (right) for the Sea of Japan side of western Japan

Green bars indicate annual numbers of days averaged for each year and region (Table 2.5-1), blue lines indicate five-year running means, and red lines indicate long-term linear trends (for confidence levels ≥ 90%).

2.6 Tropical cyclones over the western North Pacific and the South China Sea

- ○ A total of 17 tropical cyclones (TCs) with maximum wind speeds of 34 kt[33] or higher formed over the western North Pacific and the South China Sea in 2023, which was below normal.
- ○ The number of formations shows no significant long-term trend.

In 2023, 17 tropical cyclones (TCs) with maximum wind speeds of ≥ 34 kt formed over the western North Pacific and the South China Sea (Figure 2.6-1), which was below normal (i.e., the 1991 – 2020 average) of 25.1. The number of formations shows no discernible long-term trend during the analysis period from 1951 to 2023. The number of TCs with maximum wind speeds of ≥ 34 kt approaching and making landfall in Japan was 9 and 1 (Figure 2.6-1), both of which were below normal of 11.7 and 3.0, respectively. The number of TCs approaching Japan also shows no discernible long-term trend during the same period from 1951 to 2023.

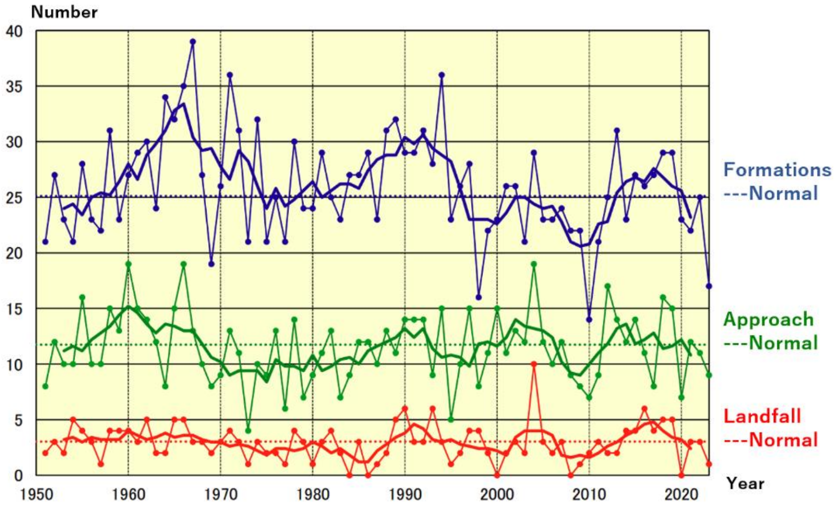

Figure 2.6-1 Time-series of the number of TCs with maximum wind speeds of ≥ 34 kt forming in the western North Pacific and the South China Sea (blue), approaching (green) and making landfall in Japan (red) from 1951 to 2023
The thin and thick lines represent annual and five-year running means, respectively.

---

[33] One knot (kt) is about 0.51 m/s

2.7 Phenology of cherry blossoms and acer leaves in Japan

○ It is virtually certain that cherry blossoms have been flowering earlier.
○ It is virtually certain that acer leaves have been changing color later.

JMA implements phenological observation to monitor seasonal progress, geographical variations and long-term changes in relation to the climate. Observation covers the first/full flowering and foliage color changes in several types of flora.

As part of its phenological monitoring, JMA observes cherry blossoms at 58 stations and acer leaves at 51 stations. Figure 2.7-1 shows interannual changes in the first reported dates of cherry blossom flowering and acer leaf color change between 1953 and 2023. The former exhibits a long-term advancing trend at a rate of 1.2 days per decade, while the latter shows a delaying trend at a rate of 3.0 days per decade (99% level of confidence for both cases). Table 2.7-1 compares climatological normals (based on 30-year averages) of the first reported date of cherry blossom flowering between 1961 – 1990 and 1991 – 2020 at stations in major Japanese cities. These phenomena are closely related to the surface mean temperature in the period before the event, and long-term warming is considered to be a major factor behind the trends observed.

IPCC AR6 WG1 reports several long-term trends in plant phenology. By way of example, peak blooming of cherry blossoms in Kyoto has been increasingly earlier in recent decades based on historical records covering several hundred years (Aono and Saito, 2010)

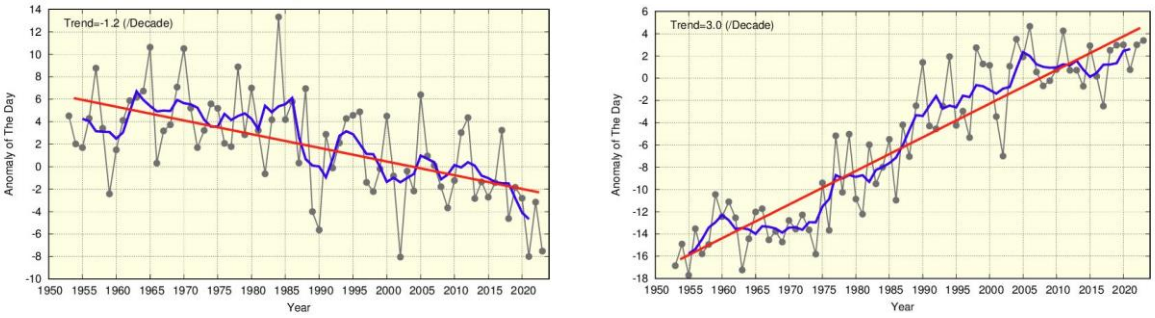

Figure 2.7-1 First reported dates of cherry blossom flowering (left) and acer leaf color change (right)
The black lines show annual anomalies of the first reported date averaged over all observation stations nationwide based on the normals for 1991 – 2020, and the blue lines indicate five-year running means. The red lines show the linear trend (cherry blossoms: −1.2 days per decade; acer leaves: +3.0 days per decade).

Table 2.7-1 Comparison of first reported dates of cherry blossom flowering
Differences in climatological normals for the first reported date of cherry blossom flowering between 1991 – 2020 and 1961 – 1990 at stations in major Japanese cities

	1961-1990 average	1991-2020 average	Difference (days)		1961-1990 average	1991-2020 average	Difference (days)
Kushiro	May 19	May 16	-3	Osaka	Apr 1	Mar 27	-5
Sapporo	May 5	May 1	-4	Hiroshima	Mar 31	Mar 25	-6
Aomori	Apr 27	Apr 22	-5	Takamatsu	Mar 31	Mar 27	-4
Sendai	Apr 14	Apr 8	-6	Fukuoka	Mar 28	Mar 22	-6
Niigata	Apr 13	Apr 8	-5	Kagoshima	Mar 27	Mar 26	-1
Tokyo	Mar 29	Mar 24	-5	Naha	Jan 16	Jan 16	0
Nagoya	Mar 30	Mar 24	-6	Ishigakijima	Jan 15	Jan 18	+3

2.8 Sea surface temperature[34] and ocean heat content

- ○ The annual mean global average sea surface temperature (SST) in 2023 was 0.40°C above the 1991 – 2020 average, and was the highest since 1891.
- ○ The global average SST has risen at a rate of about +0.61°C per century.
- ○ Globally integrated ocean heat content (OHC) exhibits a long-term increase.
- ○ OHC has exhibited a higher rate of increase since the mid-1990s.
- ○ Annual average SSTs around Japan have risen by +1.28°C per century.

2.8.1 Global sea surface temperature

The annual mean global average SST in 2023 was 0.40°C above the 1991 – 2020 average. This was the highest since 1891. The years from 2014 to 2023 represent the top-ten warmest since 1891.

The linear trend from 1891 to 2023 shows an increase of +0.61°C per century (Figure 2.8-1). Although magnitudes of the long-term SST trend vary by area, it is extremely likely that SSTs have increased in many parts of the world's oceans (Figure 2.8-2).

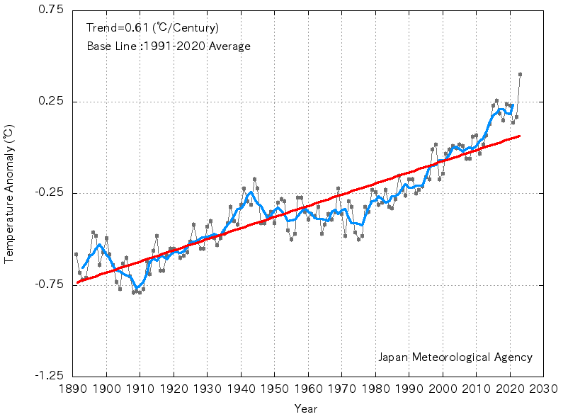

Figure 2.8-1 Time-series representation of global average sea surface temperature anomalies from 1891 to 2023

The black, blue and red lines indicate annual anomalies, the five-year running mean and the long-term linear trend, respectively. Anomalies are deviations from the 1991 – 2020 average.

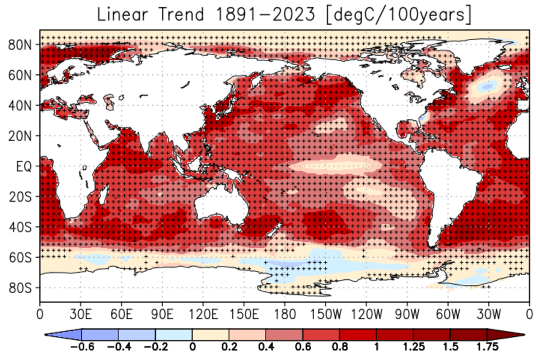

Figure 2.8-2 Linear trend of annual mean sea surface temperature during the period from 1891 to 2023 (°C per century)

Plus signs indicate statistically significant trends with a confidence level of 95%.

2.8.2 Global ocean heat content

Oceans have a significant impact on the global climate because they cover about 70% of the earth's surface and have high heat capacity. IPCC AR6 WG1 (IPCC, 2021) said that approximately 90% of heat energy in the earth's system was present in oceans since 1970.

It is virtually certain that globally integrated ocean heat content (OHC) from 0 to 2,000 m exhibits a long-term increase (statistically significant at a confidence level of 99%) (Figure 2.8-3). OHC had risen by approximately 47 × 10^{22} J in 2023 relative to 1955. Since the mid-1990s, the rate of increase (10.1 × 10^{22} J per decade for 1993 – 2023) has risen (3.9 × 10^{22} J per decade for 1955 – 1993). The Intergovernmental Panel on Climate Change Special Report on the Ocean and Cryosphere in a Changing Climate (IPCC, 2019) and IPCC

---

[34] The results of analysis regarding tendencies of SSTs worldwide and around Japan are published on JMA's website.
https://www.data.jma.go.jp/kaiyou/english/long_term_sst_global/glb_warm_e.html
https://www.data.jma.go.jp/kaiyou/english/long_term_sst_japan/sea_surface_temperature_around_japan.html

(2021) also reported an accelerated increase of ocean heat uptake.

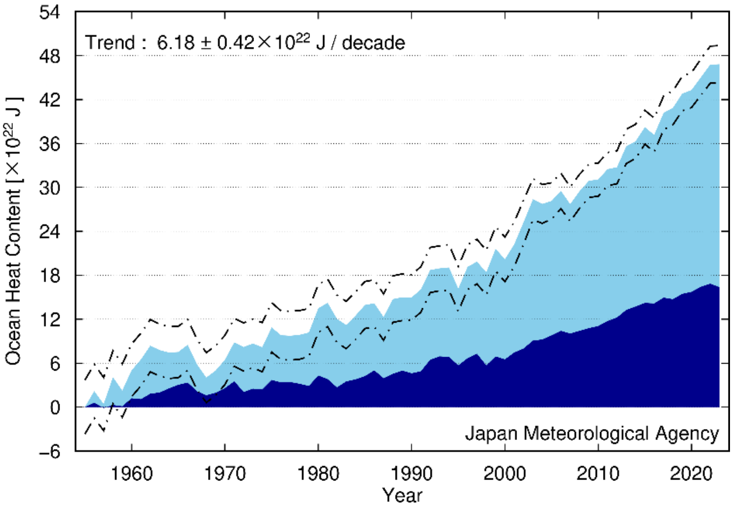

Figure 2.8-3 Time-series representation of globally integrated ocean heat content relative to 1955
The light- and dark-blue areas show annual means for global integrals of 0 to 700 m and 700 to 2,000 m, respectively, for ocean heat content relative to 1955. The dot-dash lines indicate a 95% confidence level for ocean heat content above 2,000 m.

2.8.3 *Sea surface temperature (around Japan)*

Figure 2.8-4 shows increase rates of area-averaged annual mean SSTs for 13 areas around Japan. Values for all areas have risen by +1.28°C per century, which is higher than the corresponding value for the North Pacific (+0.64°C per century). In addition to this long-term increase, SSTs fluctuate on time scales ranging from years to decades. Values have shown an upward trend in recent years, with 2023 being the highest since 1908.

It is virtually certain (statistically significant at a confidence level of 99%) that SSTs have risen by between +0.79 and +1.94°C per century in the sea off Kushiro, the sea off Sanriku, eastern and southern parts of the sea off Kanto, the sea off Shikoku and Tokai, east of Okinawa, the central and southwestern parts of the Sea of Japan, the Yellow Sea, the East China Sea, and the sea around the Sakishima Islands (areas E1-3, S1-3, N2-3, and W1-4). It is extremely likely (statistically significant at a confidence level of 95%) that SSTs in the northeastern part of the Sea of Japan (area N1) have risen by +0.42°C per century.

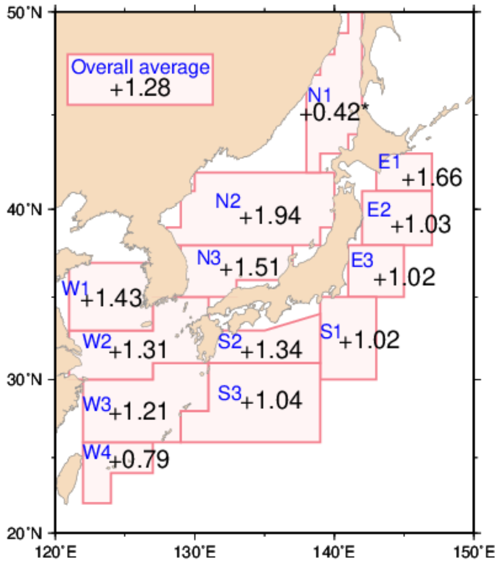

Area number	Area name
E1	Sea off Kushiro
E2	Sea off Sanriku
E3	Eastern part of the sea off Kanto
S1	Southern part of the sea off Kanto
S2	Sea off Shikoku and Tokai
S3	East of Okinawa
N1	Northeastern part of the Sea of Japan
N2	Central part of the Sea of Japan
N3	Southwestern part of the Sea of Japan
W1	Yellow Sea
W2	Northern part of the East China Sea
W3	Southern part of the East China Sea
W4	Sea around the Sakishima Islands

Figure 2.8-4 Increase rates of area-averaged annual mean SSTs around Japan from 1900 to 2023 (°C per century)
Areas with no symbol and those marked with [*] have statistically significant trend at confidence levels of 99% and 95 %.

2.9 El Niño/La Niña[35] and PDO (Pacific Decadal Oscillation)[36]

○ The La Niña event persisting after autumn 2021 terminated in winter 2022/2023 and an El Niño event emerged in spring 2023.

○ Negative PDO index values were generally observed from around 2000 to the early 2010s, generally positive values persisted in the late 2010s, and negative values have been observed since around 2020.

2.9.1 *El Niño/La Niña*

An El Niño event is a phenomenon in which sea surface temperatures (SSTs) are above normal over the equatorial Pacific from near the date line to the coast of South America for around a year. In contrast, a La Niña event is a phenomenon in which SSTs are below normal over the same area. Both events occur every few years, causing changes in global atmospheric circulations which result in abnormal weather conditions worldwide. In Japan, cooler summers and warmer winters tend to appear during El Niño events, while hotter summers and colder winters tend to appear during La Niña events.

Figure 2.9-1 shows a time-series representation of SST deviations from climatological means based on a sliding 30-year period for the El Niño monitoring region (5°N – 5°S, 150°W – 90°W) and SST deviations from reference values based on linear extrapolation with respect to the latest sliding 30-year period for the tropical western Pacific region (Eq. – 15°N, 130 – 150°E) since 2013. SSTs in the El Niño monitoring region were near or below related reference values from May 2020 to January 2023, and were above the reference values from March 2023 onward. These variations are consistent with the termination of La Niña conditions in winter 2022/2023 and the development of El Niño conditions from spring 2023 onward. SSTs in the tropical western Pacific were near or above related reference values from August 2022 to May 2023, and near or below the reference values from June 2023 onward.

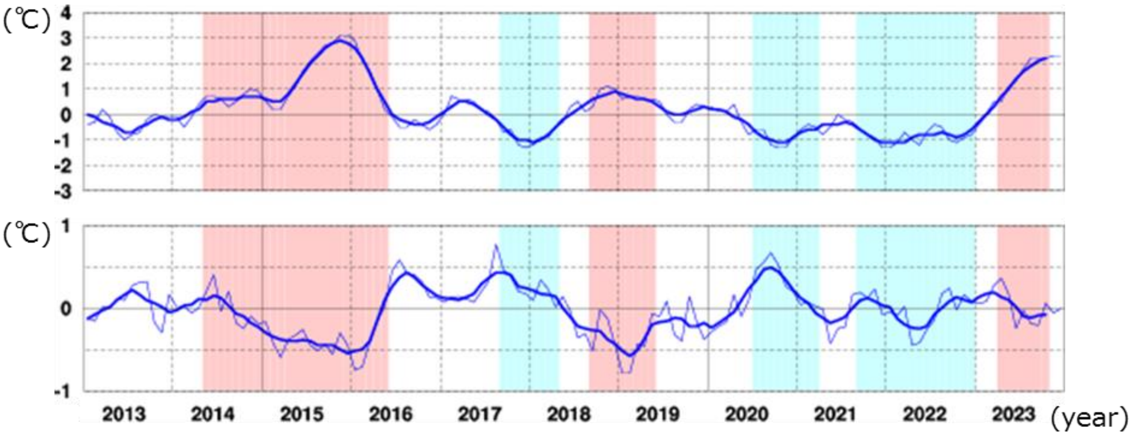

Figure 2.9-1 Time-series representations of SST deviations from the climatological mean based on a sliding 30-year period for the El Niño monitoring region (top) and SST deviations from reference values based on linear extrapolation with respect to the latest sliding 30-year period for the Western Pacific (bottom)
Thin lines indicate monthly means, and smooth thick curves indicate the five-month running mean.
Red shading denotes El Niño periods, and blue shading denotes La Niña periods.

---

[35] See the Glossary for terms relating to El Niño phenomena. Monthly diagnosis reports, ENSO monitoring products, ENSO indices and El Niño outlooks are published on JMA’s website.
https://www.data.jma.go.jp/tcc/tcc/products/elnino/index.html

[36] See the Glossary for an explanation of the PDO. The PDO index time series is published on JMA's website.
https://www.data.jma.go.jp/tcc/tcc/products/elnino/decadal/pdo.html

2.9.2 Pacific Decadal Oscillation

SST variability is also observed on time scales ranging from one to several decades in addition to El Niño/La Niña events, whose time scale is several years, and long-term trends associated with global warming. Among these, the atmosphere and oceans tend to co-vary with a period of more than ten years in the North Pacific in a phenomenon known as the Pacific Decadal Oscillation (PDO, Mantua et al. 1997). When SSTs are lower (higher) than their normals in the central part of the North Pacific, those in its part along the coast of North America are likely to be higher (lower) than their normals. This seesaw pattern changes slowly, and appears repeatedly with a period of more than ten years. The PDO index, which is defined by the SST anomaly pattern in the North Pacific, is used as a measure of phase and strength of the oscillation. Since both the PDO index and SST anomaly patterns associated with PDO are estimated based on monthly mean SST anomalies, it is noted that they include relatively short-timescale variabilities such as El Niño/La Niña events in addition to decadal to multi-decadal components.

When the PDO index is positive (negative), SSTs in the central part of the North Pacific are likely to be lower (higher) than their normals in addition to those along the coast of North America, and those in the equatorial part from near the date line to the coast of South America are likely to be higher (lower) than normal. This tendency is analogous to the patterns observed in El Niño (La Niña) events (Figure 2.9-2). Additionally, sea level pressures (SLPs) in the high latitudes of the North Pacific are likely to be lower (higher) than their normals in the same time (Figure 2.9-3). This indicates that the Aleutian Low is stronger (weaker) than its normal in winter and spring. These atmospheric variations affect meteorological conditions mainly in North America. When the PDO index is positive, winter temperatures tend to be high in the northwestern part of North America and the northern part of South America, and low in the southeastern part of the USA and in parts of China (Mantua and Hare, 2002).

The PDO index was generally positive from the late 1920s to the early 1940s, from the late 1970s to around 2000 and in the late 2010s, and was generally negative from the late 1940s to the mid-1970s and from around 2000 to the early 2010s (Figure 2.9-4). Negative values have persisted since around 2020.

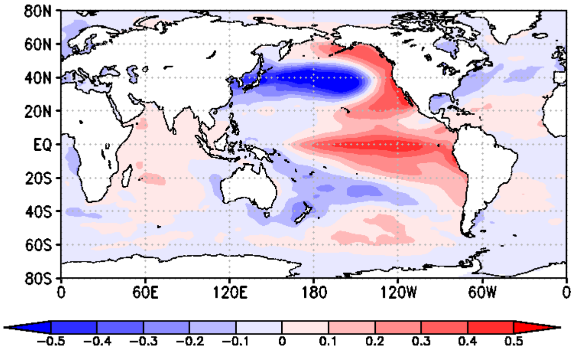

Figure 2.9-2 Typical SST anomaly patterns in the positive phase of the PDO

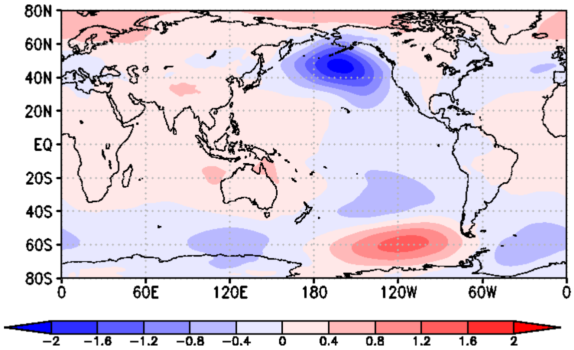

Figure 2.9-3 Typical SLP anomaly patterns in the positive phase of the PDO

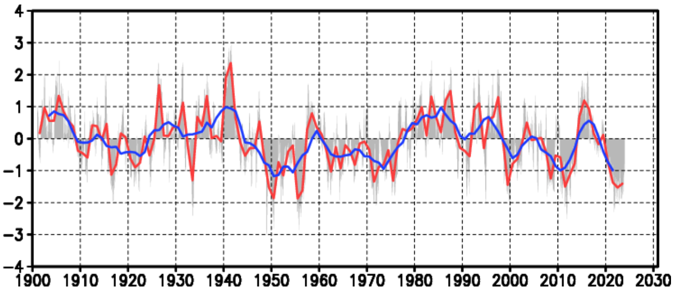

Figure 2.9-4 Time-series of the PDO index

The red line represents annual mean values for the PDO index, the blue line represents five-year running mean values, and the gray bars represent monthly values.

2.10 Sea levels around Japan[37]

- ○ No significant long-term trend of mean sea level (MSL) has been observed along the coast of Japan over the past 110 years. However, a trend of MSL rise has been seen since the 1980s.
- ○ The average rate of MSL rise using records from 13 tide gauges (based on GPS data to exclude the effects of vertical land motion (VLM)) was 3.4 [1.1 to 5.6][38] mm per year from 2006 to 2018.

MSL in Japanese coastal areas exhibited no significant rise from 1906 to 2023. Variations with 10- to 20-year periods are seen in this time frame, as decadal climate variability has a greater effect than global warming. However, a trend of MSL rise since the 1980s is seen. This is attributed to global mean sea level (GMSL) rise from the effects of global warming (Figure. 2.10-1).

The annual MSL anomaly around Japan in 2023 is 72 mm higher than the normal (i.e., the 1991 – 2020 average), and it is the highest since 1906 (Figure.2.10-1). However, the values in Figure. 2.10-1 may still include some VLM effects.

Annual MSL is calculated using records from 13 tide gauges with GPS data to exclude the effects of VLM. The 2023 MSL value was 57 mm higher than that of 2004 and the highest since that year.

Chapter 9 of the IPCC 6th Assessment Report (AR6) concluded that GMSL rise in the 20th century had been faster than in any prior century over the last millennium, with acceleration since the late 1960s. The average rate of GMSL rise was 3.7 [3.2 to 4.2] mm per year from 2006 to 2018 (high confidence). The rate of MSL rise around Japan with the effects of VLM excluded was 3.4 [1.1 to 5.6] mm per year in the same period. These figures are comparable to those observed for GSML in recent years.

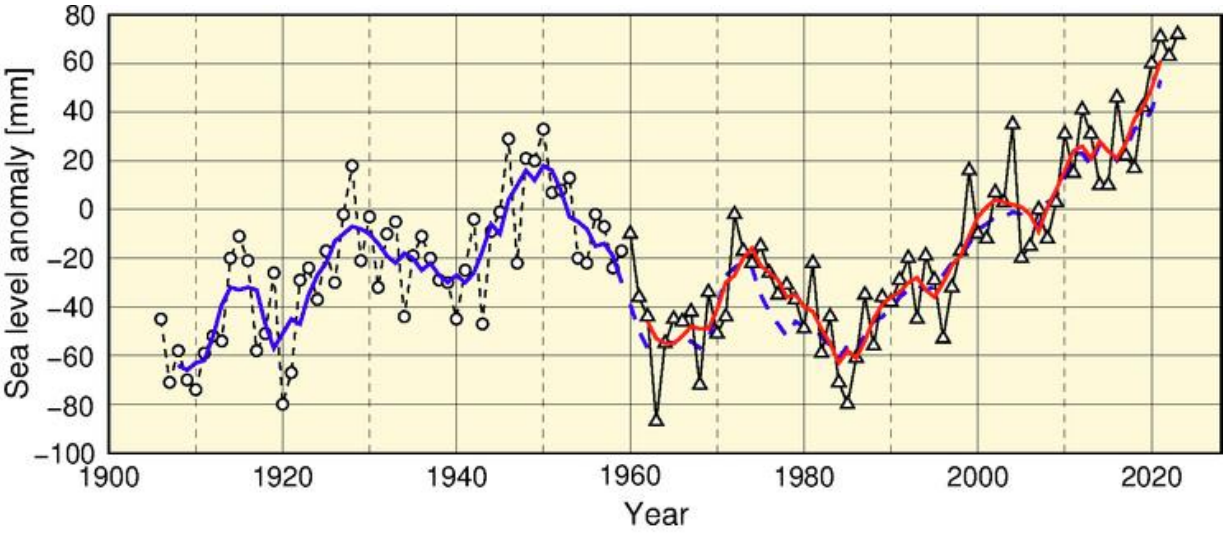

Figure 2.10-1 Time-series representation of annual MSL around Japan (1906 - 2023)

The blue line represents the five-year running mean of annual MSL anomalies averaged over four stations. The red line represents the same for 16 stations.[39]

---

[37] Sea levels around Japan are published on the JMA's website. https://www.data.jma.go.jp/kaiyou/english/sl_trend/sea_level_around_japan.html

[38] The values in square brackets in this section show the 90% uncertainty range.

[39] A map of the 4/16 tide gauge stations is available on the JMA website at https://www.data.jma.go.jp/kaiyou/db/tide/sl_area/sl_rgtrend.html

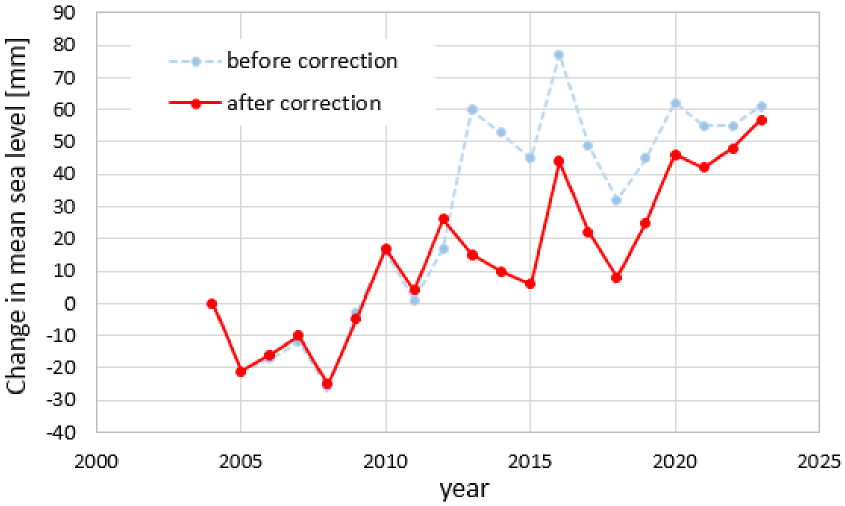

Figure 2.10-2 Changes in mean sea level around Japan with the effects of vertical land motion excluded (2004 – 2023)

Changes in MSL average among 13 tide gauges with GPS data[40]. The blue plots represent changes estimated with tide gauge records before correction, and the red plots represent changes after correction. MSL in 2004 is taken as 0 mm.

---

[40] A map of the 13 tide gauge stations with GPS data is available on the JMA website (Japanese only) at https://www.data.jma.go.jp/kaiyou/db/tide/sl_gcntrend/sl_gcntrend.html

2.11 Sea ice[41]

○ The sea ice extent in the Arctic Ocean is decreasing.

○ There has been no discernible trend in the Antarctic Ocean.

○ The maximum sea ice extent in the Sea of Okhotsk shows a decreasing trend of 0.055 × 10^6 km^2 per decade.

2.11.1 Sea ice in Arctic and Antarctic areas

Sea ice is formed in the Arctic and Antarctic. As the albedo (reflection coefficient) of sea ice is greater than that of the ocean surface, sea ice extent reductions caused by global warming result in more solar energy absorption at the surface, which in turn accelerates global warming. Sea ice also affects deep-ocean circulation because the expelled salt as it forms increases the salinity (and therefore the density) of the water below it causing the water to sink.

It is virtually certain that there has been a long-term trend of decrease in sea ice extent in the Arctic Ocean since 1979 when continuous monitoring of sea ice using satellite sensors with similar properties started (statistically significant at a confidence level of 99%). In particular, the reduction in the annual minimum extent is notable. The rate of decrease in the annual minimum up to 2023 was 0.086 × 10^6 km^2 per year. Meanwhile, there has been no discernible trend in the Antarctic Ocean[42]. The annual maximum, mean and minimum sea ice extent in 2023 were all record lows since records began in 1979.

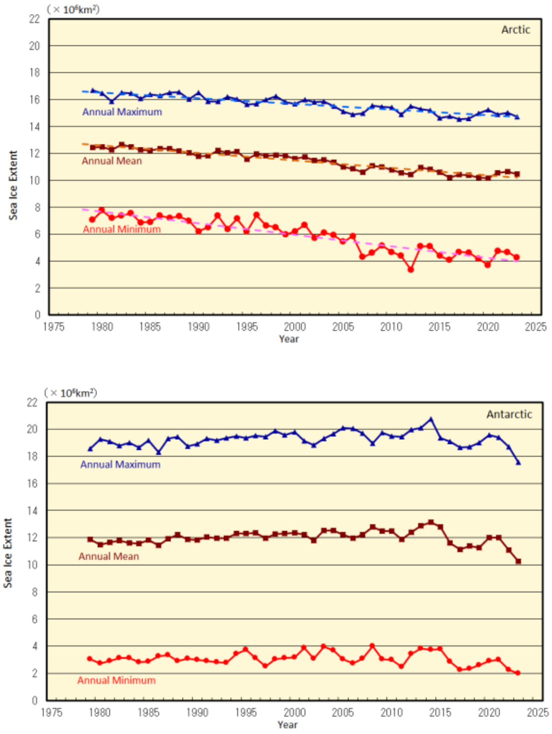

Figure 2.11-1 Time-series representations of annual maximum, mean and minimum sea ice extent in the Arctic Ocean (including the Sea of Okhotsk and the Bering Sea) (upper) and in the Antarctic Ocean (lower) from 1979 to 2023

The solid blue, brown and red lines indicate the annual maximum, mean and minimum sea ice extent, respectively. The dashed lines indicate the linear trends (statistically significant at the confidence level of 95%). Sea ice extents are calculated from brightness temperature data provided by NASA (the National Aeronautics and Space Administration) and NSIDC (the National Snow and Ice Data Center).

In 2023, the annual maximum Arctic sea ice extent was 14.72 × 10^6 km^2 on March 2. The extent subsequently decreased during spring and summer in the Northern Hemisphere and reached its annual

---

[41] Information on sea ice in the Arctic/Antarctic, and in the Sea of Okhotsk are published on JMA's website.
https://www.data.jma.go.jp /kaiyou/english/seaice_global/series_global_e.html (Arctic/Antarctic)
https://www.data.jma.go.jp /kaiyou/english/seaice_okhotsk/series_okhotsk_e.html (Sea of Okhotsk)

[42] It was reported in IPCC AR6 WG1 (2021) that there has been no significant trend in Antarctic sea ice area from 1979 to 2020 due to regionally opposing trends and large internal variability.

minimum of 4.25×10^6 km^2 on September 16. Meanwhile, the Antarctic sea ice extent was at its annual minimum of 1.98×10^6 km^2 on February 21, marking the lowest minimum since 1979. The extent subsequently increased during autumn and winter in the Southern Hemisphere and reached its annual maximum of 17.54×10^6 km^2 on September 7, also marking the lowest maximum since 1979 (Figures 2.11-2, 2.11-3).

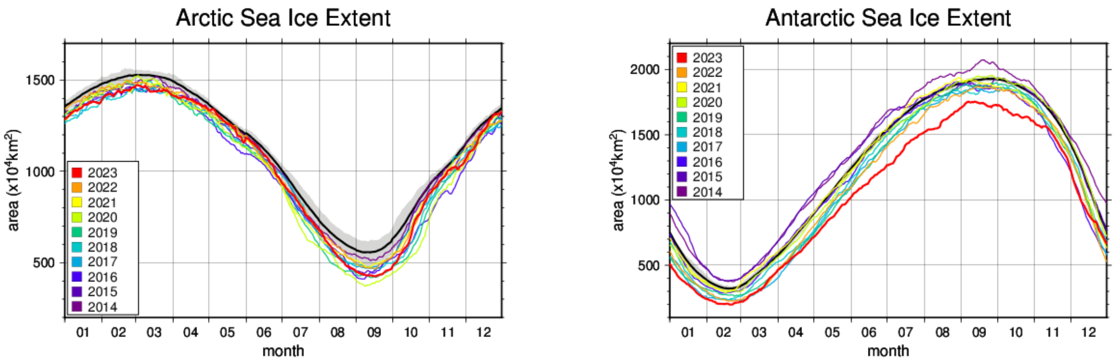

Figure 2.11-2 Annual variations of sea ice extent in the Arctic (left) and Antarctic (right) areas in 2023 (red line)
Black lines represent the normal, and shading represents the range of the normal.

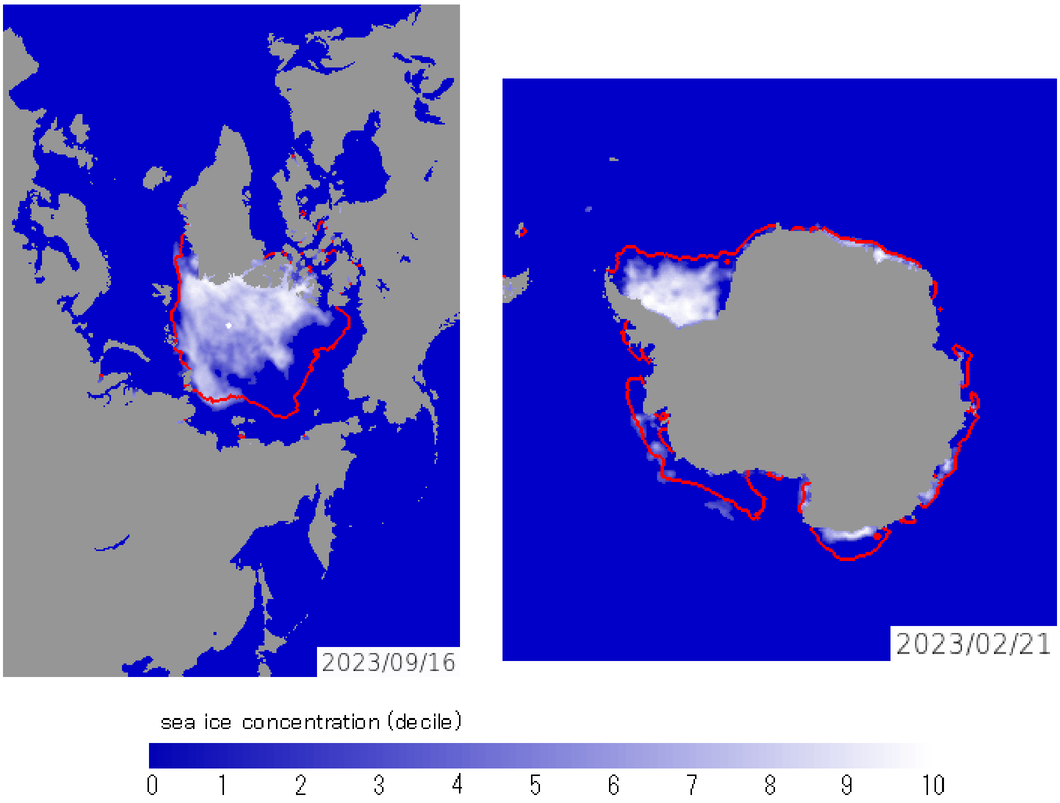

Figure 2.11-3 Annual minimum sea ice distribution for the Arctic and Antarctic
The figure on the left shows Arctic sea ice concentration on September 16 2023, and on the right is Antarctic sea ice concentration on February 21 2023. The red lines represent the normal sea ice edge for the relevant days.

2.11.2 Sea ice in the Sea of Okhotsk

The Sea of Okhotsk is the southernmost sea in the Northern Hemisphere where sea ice is observed across a wide area. The variation of the sea ice in the Sea of Okhotsk has effect on climate in coastal area facing the Sea of Okhotsk in Hokkaido and water quality of Oyashio.

The maximum[43] sea ice extent in the Sea of Okhotsk shows large interannual variations. However, it is virtually certain that it exhibited a long-term trend of decrease for the period from 1971 to 2023 (statistically significant at the confidence level of 99%). The maximum extent has decreased by 0.055 × 10^6 km^2 per decade (corresponding to 3.5% of the Sea of Okhotsk's total area).

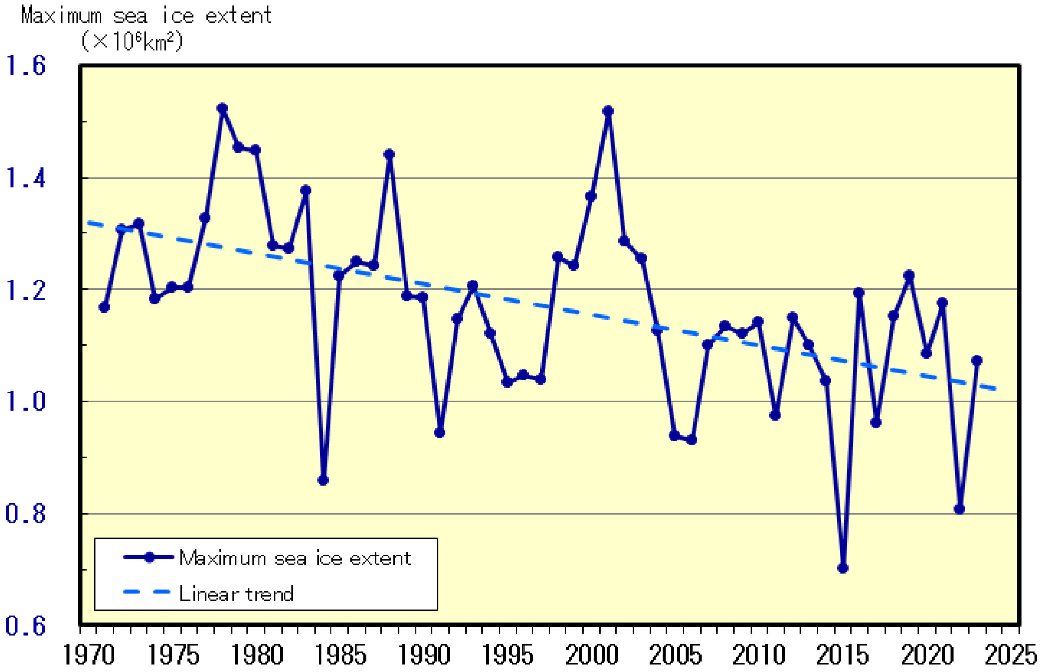

Figure 2.11-4 Time-series representations of maximum sea ice extent for the Sea of Okhotsk from 1971 to 2023

Dashed line indicates the linear trend.

---

[43] The maximum sea ice extent: It shows sea ice extent that sea ice was the most expanding of every five days in the winter.

2.12 Ocean carbon dioxide and ocean acidification

○ Concentrations of carbon dioxide in the air and in the oceans are increasing.
○ Anthropogenic carbon dioxide is absorbed into the ocean and accumulates there.
○ Oceanic acidity has increased due to accumulation of anthropogenic carbon dioxide.

2.12.1 Ocean carbon dioxide

(1) Ocean carbon dioxide in the western North Pacific

Based on data collected by JMA research vessels along the 137°E (3 – 34°N) and 165°E (5°S – 35°N) lines, oceanic and atmospheric $p\mathrm{CO}_2$ are increasing in the western North Pacific area (Figures 2.12-1, 2.12-2). The growth rates for oceanic and atmospheric $p\mathrm{CO}_2$ along the 137°E line from 1985 to 2023 were 1.5 – 2.1 and 1.8 – 2.0 µatm/year, respectively, while those along the 165°E line from 1996 to 2023 were 1.8 – 2.8 and 1.9 – 2.1 µatm/year, respectively.

The column inventory of ocean CO_2 was estimated using long-term time-series data on dissolved inorganic carbon from 1990s (Figure 2.12-3). The column inventory rates of ocean CO_2 between the sea surface and 27.2 σ_θ (approx. 1,000 m in depth) along 137°E, 165°E and 24°N are approximately 4 – 11 tC/km^2/year. The column inventory rates of ocean CO_2 around 20 – 30°N are higher than those at 10°N and 35°N.

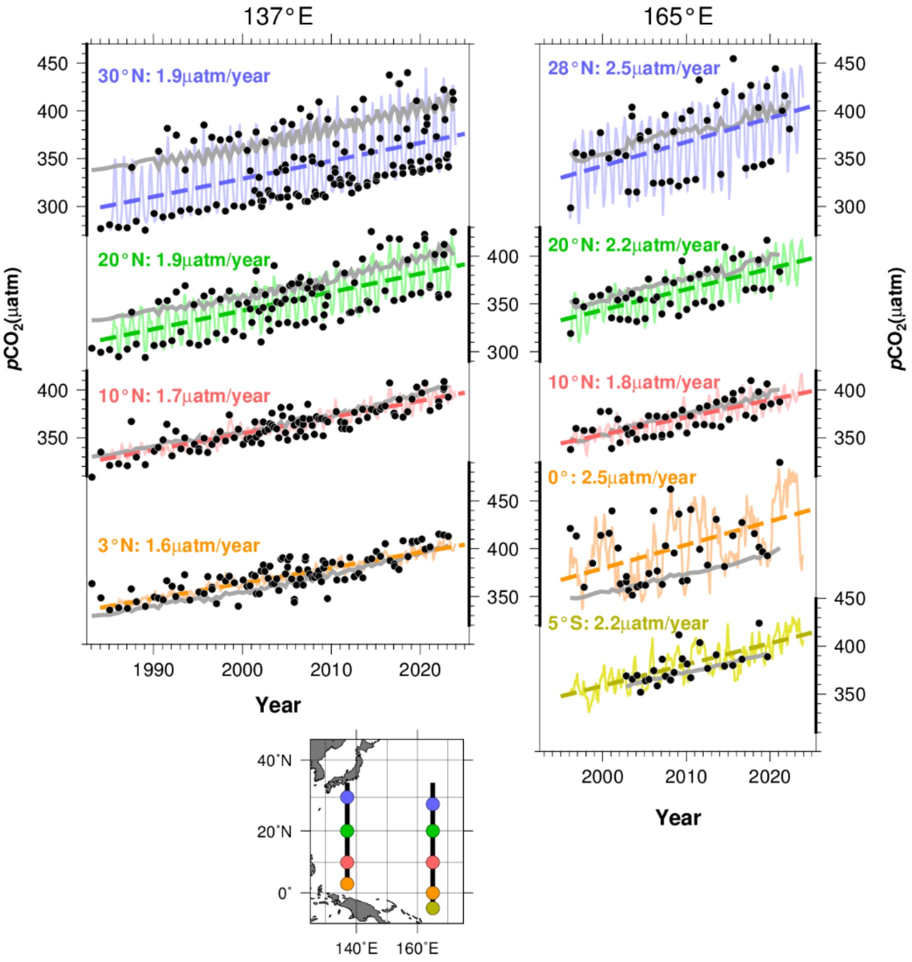

Figure 2.12-1 Annual changes in oceanic and atmospheric $p\mathrm{CO}_2$ along the 137°E (left) and the 165°E (right) lines
Black plots show oceanic $p\mathrm{CO}_2$ observation values. Solid lines represent monthly oceanic $p\mathrm{CO}_2$ values reconstructed using the method of Ishii et al. (2011), dashed lines show the long-term trend of oceanic $p\mathrm{CO}_2$, and gray lines indicate the observed values of atmospheric $p\mathrm{CO}_2$.

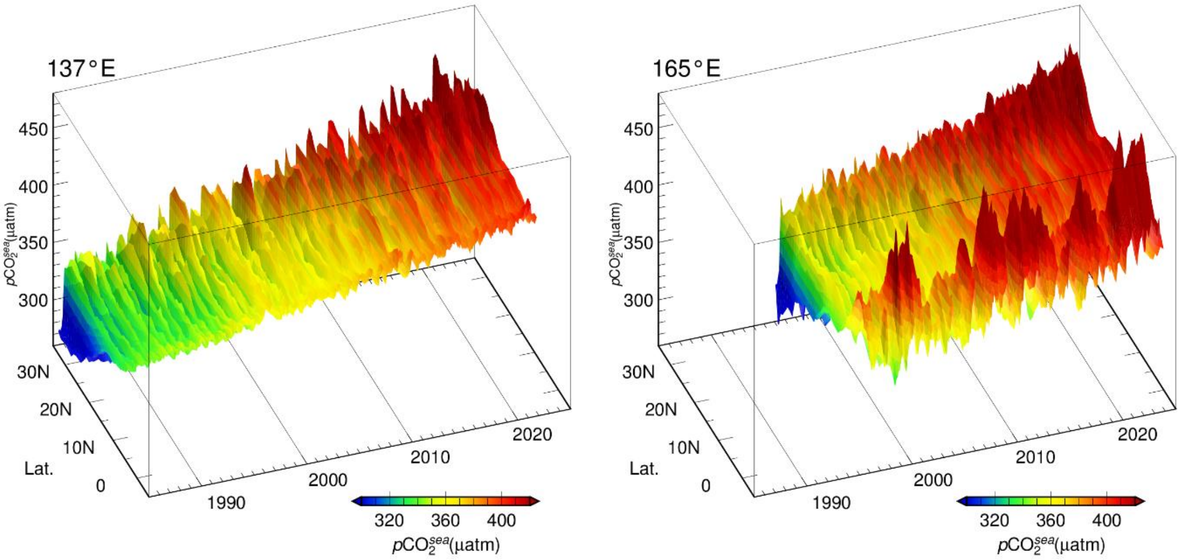

Figure 2.12-2 Time-latitude distribution of oceanic pCO_2 along the 137°E (left) and the 165°E (right) lines
Colors indicate reconstructed monthly oceanic pCO_2 value. The part on the left shows oceanic pCO_2 along the 137°E (3-34°N) since 1985 and the part on the right shows oceanic pCO_2 along the 165°E (5°S-35°N) since 1996.

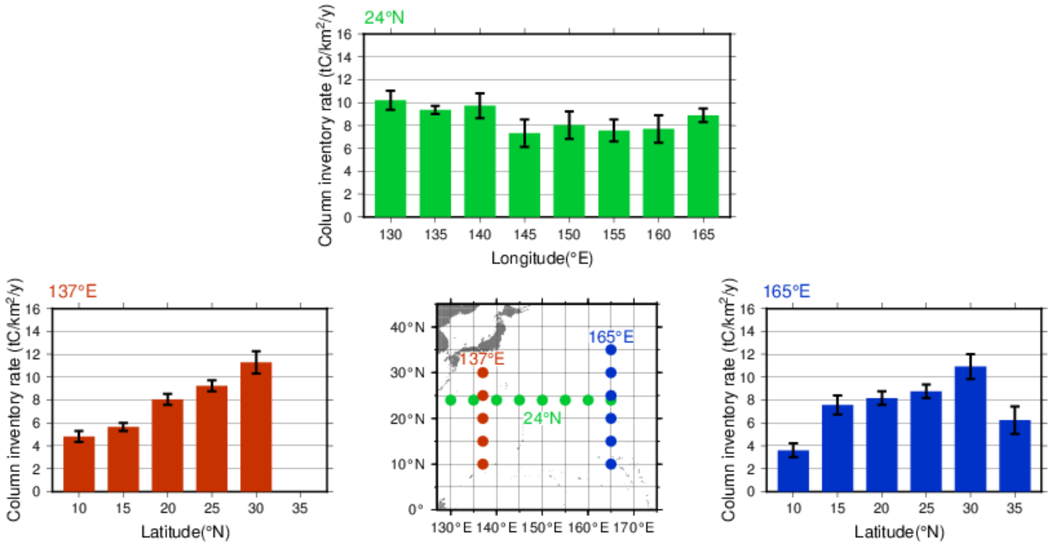

Figure 2.12-3 Changes in ocean CO_2 between the sea surface and 27.2 σ_θ (approx. 1,000 m in depth) along 137°E, 165°E and 24°N for the periods 1994 – 2023, 1992 – 2022 and 1992 – 2023, respectively
Error bars denote a 95% confidence level

(2) Global ocean carbon dioxide uptake

Analysis of observation data reveals relationships between surface ocean CO_2 concentrations and other oceanographic parameters such as sea surface temperature (SST), salinity and chlorophyll-a concentration, which differ by region. Global ocean CO_2 concentrations were estimated using datasets of such parameters based on these relationships, and CO_2 exchanges between the atmosphere and the ocean were calculated (Iida *et al.*, 2021). It was found that the ocean releases CO_2 into the atmosphere in equatorial regions and the northern Indian Ocean and absorbs CO_2 in other regions (Figure 2.12-4 (a)). Figure 2.12-4 (b) and (c) show monthly and annual variations in global ocean CO_2 uptake, respectively. The estimated mean annual global ocean CO_2 uptake during 1990 to 2022 was 2.1 GtC per year. The estimated annual global ocean CO_2 uptake has increased during the period.

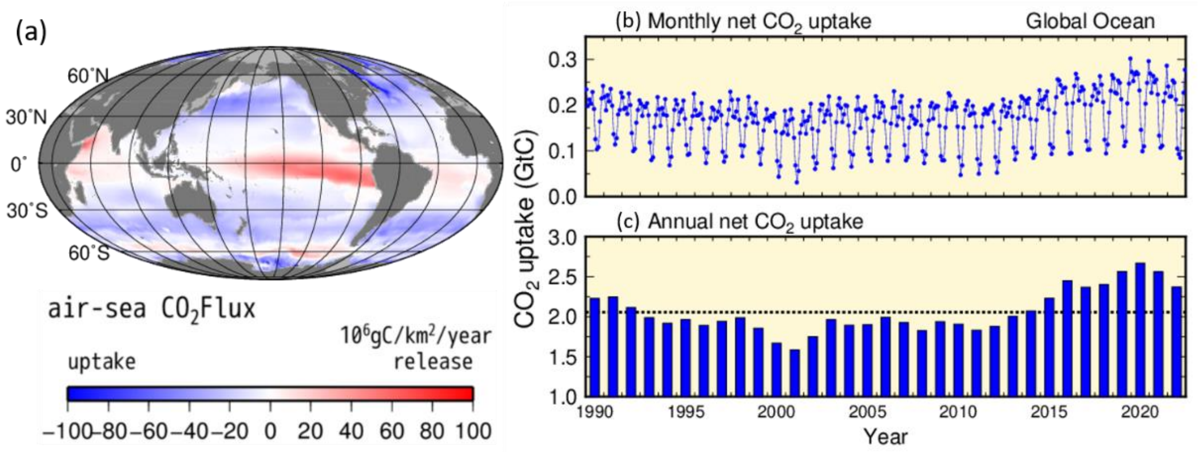

Figure 2.12-4 Distribution of global ocean CO_2 uptake/release for 2022 (a) and time-series representations of monthly (b) and annual (c) CO_2 uptake from 1990 to 2022

The blue/red area in the map on the left (a) indicates ocean uptake/release of CO_2 from/into the atmosphere. The grey area shows the border of the region analyzed. The dotted line in graph (c) shows the 2.1 GtC average for the period from 1990 to 2022.

2.12.2 Ocean acidification

(1) Ocean acidification around Japan

To monitor the long-term variability of ocean acidification, JMA has analyzed monthly sea surface pH values since 1998 based on data from its oceanographic observations and related database content. The results show a clear trend of in-situ pH decrease in seas around Japan ranging from 0.019 per decade around Kyushu and Okinawa and Hokkaido and east of Japan to 0.024 per decade in the Sea of Japan. The average trend in sea areas around Japan is 0.021 per decade. These values are similar to observed rates of pH decrease in worldwide open oceans as recorded in the IPCC special report (SROCC; IPCC, 2019).

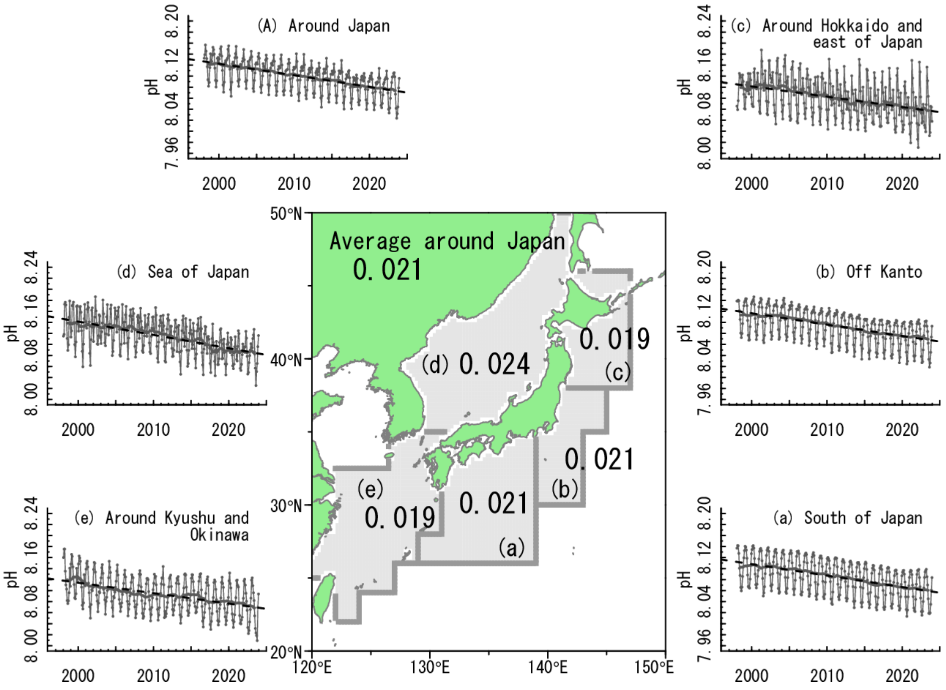

Figure 2.12-5 Long-term trends of pH in sea areas around Japan

Black points with lines, bold lines and dashed lines indicate average pH values, yearly running means and long-term trends in areas (a) to (e), and the average around Japan, respectively.

(2) Ocean acidification in the western North Pacific

JMA monitors long-term trends in surface and interior ocean pH along repeat hydrographic lines at 137°E and 165°E, and performs analysis to determine the average decrease in surface ocean pH throughout the Pacific using data on oceanic CO_2 concentration and related factors. The results clearly show a decreasing trend in surface ocean pH for the whole Pacific, and 0.014 to 0.022 and 0.016 to 0.028 per decade at individual stations on the 137°E and 165°E lines, respectively (Figures 2.12-6 and 2.12-7). Ocean interior pH along these lines also shows decreasing trends of 0.013 to 0.031 per decade (Figure 2.12-8) with higher rates in the northern than the southern subtropics due to greater accumulation of anthropogenic CO_2 in the former.

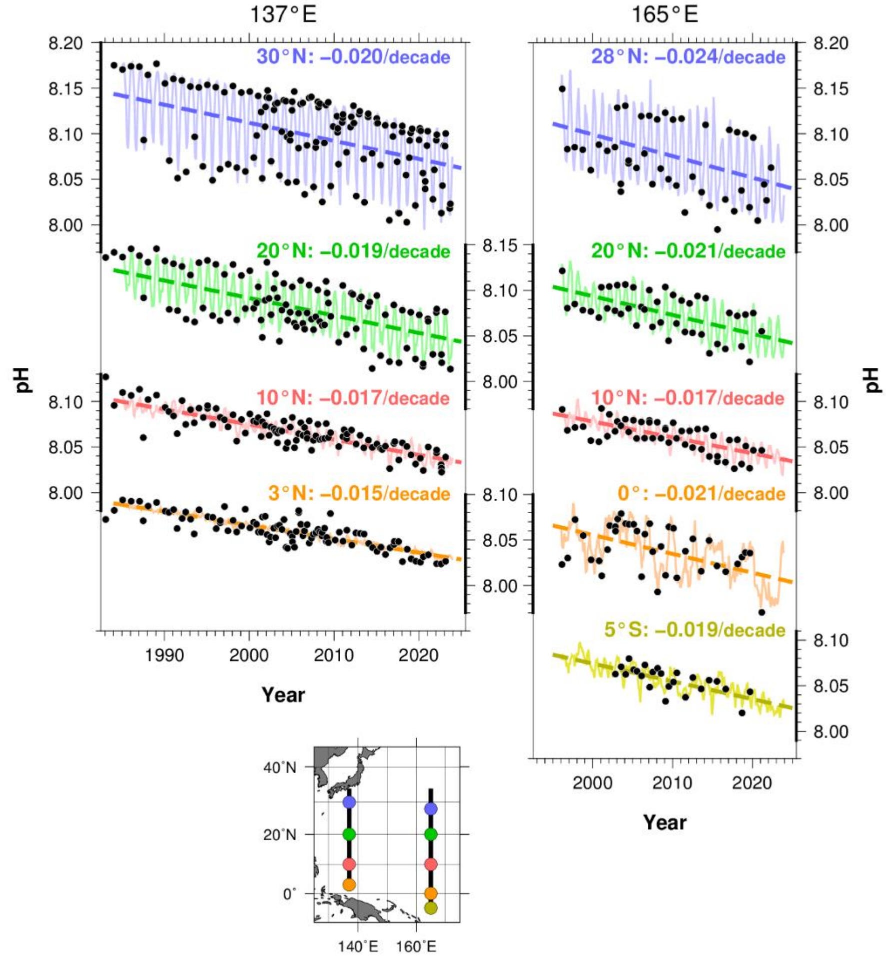

Figure 2.12-6 Long-term trends of pH at each latitude in JMA's repeat hydrographic lines at 137°E (left) and 165°E (right)

Black plots show pH observation values based on pCO_2 observation data. Solid lines represent monthly pH values reconstructed using the method of Ishii et al. (2011), dashed lines show the long-term trend of pH, and numbers indicate rates of change at each latitude.

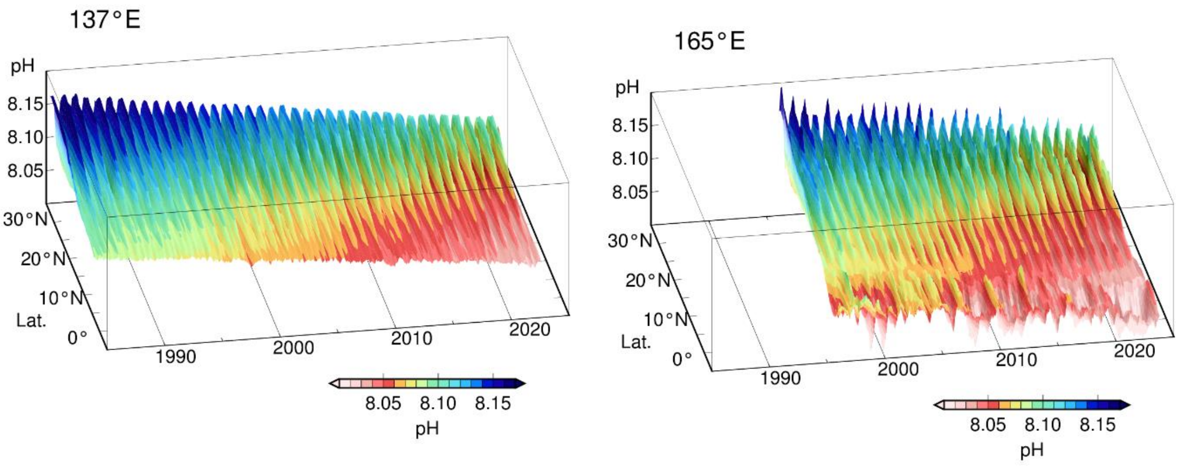

Figure 2.12-7 Time-latitude distribution of pH along the 137°E (left) and the 165°E (right) lines
Colors indicate reconstructed monthly pH values. The part on the left shows pH along 137°E (3-34°N) since 1985, and the part on the right shows pH along 165°E (5°S-35°N) since 1996.

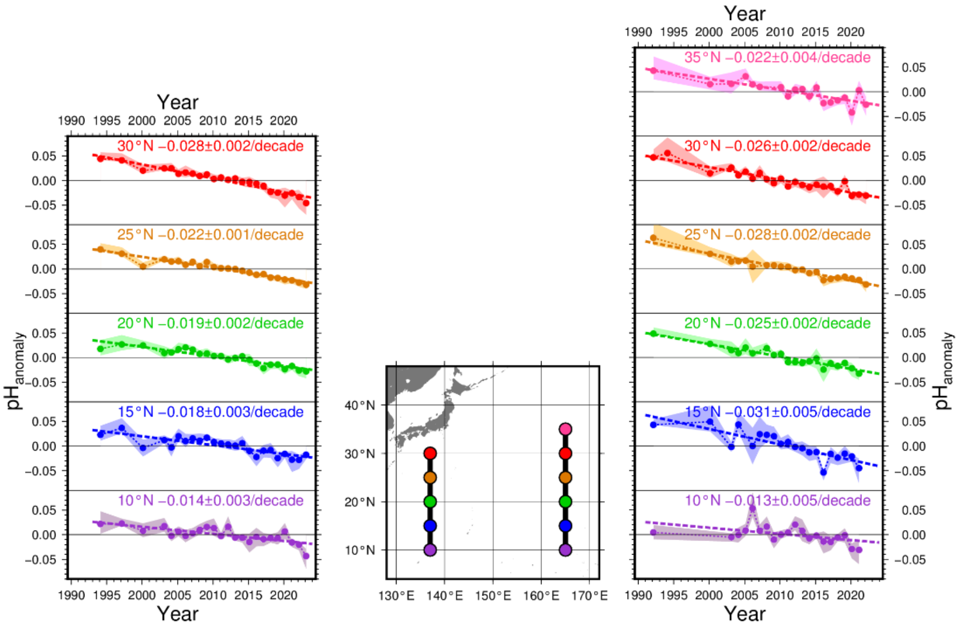

Figure 2.12-8 Long-term trends of pH between 25.0 σ_0 and 26.9 σ_0 (a depth range of about 150~800 m) along 137°E (left) and 165°E (right)
Plots show pH anomalies from averages for the whole period on the isopycnals at each latitude. The shaded areas and bold dotted lines represent the standard deviation range (±1 σ) and the long-term trend, respectively. The numbers indicate rates of change at each latitude.

(3) Ocean acidification in the global ocean

JMA has analyzed monthly sea surface pH values since 1990 using a global oceanographic observation database via the method outlined in 2.12-1 (2). The results show a clear trend of in-situ pH decrease at 0.019 per decade in the global ocean. The rates of decrease are 0.019, 0.018 and 0.020 pH per decade in the Pacific, the Atlantic and the Indian Ocean, respectively.

The pH in surface ocean waters varies by area due to differences in ocean circulation, biological activity and seasonal change. In the equatorial area, upwelling CO_2-rich seawater causes relatively low pH values. Subtropical (subpolar) areas show higher pH values than equatorial areas with seasonal changes of higher (lower) pH in winter and lower (higher) pH in summer.

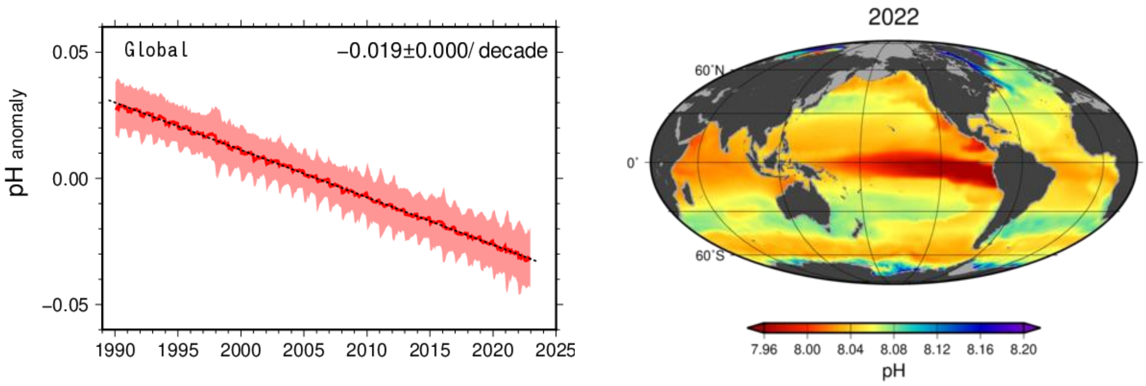

Figure 2.12-9 Long-term trend of surface ocean pH (left) and pH distribution in 2022 (right) in the global ocean
Left: Rate of pH change in the global ocean. The solid line is a time-series representation of the pH anomaly from the average from 1991 to 2020 in the global ocean. The shaded area and dotted line represent the standard deviation range (±1σ) and the long-term trend, respectively. The '±' symbol indicates a 95% confidence interval.
Right: Lower pH values are represented as warmer colors.

Explanatory note on detection of statistical significance in long-term trends

Meteorological observation data, including those relating to temperature and precipitation, are subject to large amplitude fluctuations due to the influence of atmospheric and oceanic dynamics on a broad spectrum of spatial and temporal scales. To examine the possible presence of long-term climate system trends associated with global warming in consideration of natural variability, raw climate data need to be converted into suitable statistical time-series representations and subjected to statistical testing in order to highlight the likelihood of systematic temporal trends that cannot be explained by random variability alone. When the results of such testing allow reasonable conclusion that random variability is unlikely to be the sole factor at work, a change is described as statistically significant.

In this report, the likelihood of a systematic long-term change existing in a time-series representation is based on the results of statistical significance testing performed at confidence levels of 99, 95 and 90%. The following terminology summary describes each level:

Level of confidence	Term
≥ 99%	**Virtually certain** to have increased/decreased (statistically significant at a confidence level of 99%)
≥ 95%	**Extremely likely** to have increased/decreased (statistically significant at a confidence level of 95%)
≥ 90%	**Very likely** to have increased/decreased (statistically significant at a confidence level of 90%)
Other than those above	No discernible trend

The following statistical methods are applied for the data used in this report:

i) For statistical variables whose annual fluctuation component can be assumed to follow normal distribution

For temperature anomalies, trend-removed annual variability data are expected to approximately follow normal distribution. T-testing is performed for statistical variables assumed to be normally distributed using a coefficient of correlation between years and values.

ii) For statistical variables whose annual fluctuation component cannot be assumed to follow normal distribution

The assumption of normality may not be applicable to frequency statistics regarding weather conditions, including those for extremely warm days, tropical nights and hourly precipitation amounts exceeding 50 mm. Accordingly, non-parametric testing, which does not depend on underlying assumptions about distribution, is applied to such variables.

It should be noted that statistical tests are in theory inevitably susceptible to the establishment of false conclusions even if the results indicate a statistically significant trend. Even outcomes indicating statistical significance at confidence levels of 90, 95 or 99% imply that there are small inherent probabilities of up to 10, 5 and 1%, respectively, of the significance being erroneously detected when in fact the observed long-term change occurred by mere random chance. Conversely, when a systematic long-term change actually exists, statistical testing may fail to detect the significance correctly. In general, test results are not considered highly stable if they are based on observation records that are temporally limited, influenced by large annual fluctuations/rare events or subject to change when new observations are added to a data sequence. Readers are encouraged to interpret the analytical results presented in the report appropriately with due note of these considerations.

Glossary

Aerosols

Aerosols are airborne solids or liquids in fine particle form. Their many types include particles of natural origin blown up from land/sea surfaces, anthropogenic particles and secondary aerosols formed from anthropogenic and biogenic precursors. In addition to absorbing and scattering sunlight, they also provide condensation nuclei for clouds. Particulate matter 2.5 (PM2.5) is the name given to aerosol particles measuring 2.5 micrometers or less in diameter (about 30 times thinner than a human hair), and is considered to have possible adverse effects on human health when inhaled.

Anthropogenic

Resulting from or produced by human activity.

Arctic Oscillation

The Arctic Oscillation (AO) is a major atmospheric circulation variation exhibiting an annular pattern of sea-level pressure anomalies in a seesaw fashion with one sign over the Arctic region and the opposite sign over the mid-latitudes. Its negative phase, which is characterized by positive and negative sea-level pressure anomalies over the Arctic region and the mid-latitudes, respectively, helps cold Arctic air move into the mid-latitudes. The positive phase, whose sea-level pressure anomaly pattern is reversed, keeps Arctic air over the Arctic region.

Extreme climate event

In general, an extreme climate event is recognized as an unusually severe or rare climate event creating disaster conditions or exerting significant socio-economic influence. The definition includes severe weather conditions covering periods ranging from only a few hours (such as heavy rain or strong wind) to several months (such as drought or cold summer conditions). JMA defines extreme climate events as those occurring once every 30 years or longer.

IPCC (Intergovernmental Panel on Climate Change)

The Intergovernmental Panel on Climate Change (IPCC) is an international organization established by the United Nations Environment Programme (UNEP) and the World Meteorological Organization (WMO) in 1988. It reviews and assesses scientific, technical and socio-economic information on climate change, the potential impacts of such change and related vulnerability, and options for adaptation and mitigation, in collaboration with scientists and experts on an international basis. The Panel's reports highlight common understanding of such information to support political matters such as treaty negotiations on global warming.

Kosa (Aeolian dust)

Kosa (Aeolian dust) is a meteorological phenomenon in which fine dust is blown up to an altitude of several thousand meters by cyclonic or other wind systems from deserts or cropland in semi-arid areas of the Asian continent, and is transported over long distances by westerly winds, resulting in haze or dustfall in downstream areas. It is often observed between March and June in Japan and makes the sky yellow and hazy. Heavy Kosa can affect transportation by obstructing visibility.

Monsoon

The term *monsoon* primarily refers to seasonally reversing winds, and by extension includes related seasonal rainfall change with wet and dry phases. Monsoon climate regions where seasonal winds prevail are found in numerous places around the world, with a major one located over a broad area from the Asian continent to northern Australia.

Normals

Normals represent climatic conditions at meteorological stations, and are used as a base to evaluate meteorological variables (e.g., temperature, precipitation and sunshine duration) and produce generalizations (e.g., cool summer, warm winter and dry/wet months) for particular periods. JMA uses averages for the most recent three decades (currently 1991 – 2020) as normals, which are updated every decade in line with WMO Technical Regulations.

Terms relating to surface temperature variations

El Niño/La Niña events: In an El Niño event, sea surface temperatures (SSTs) are higher than normal across a wide region from near the date line to the area off the coast of South America in the equatorial Pacific for about a year. In a La Niña event, SSTs are lower than normal in the same area. Both occur every few years, and are associated with frequent extreme climate conditions worldwide.

JMA recognizes the occurrence of an El Niño event when the five-month running mean of SST deviations from the climatological means (based on a sliding 30-year period averaged over the NINO.3 El Niño Monitoring Region (5ºN – 5ºS, 150ºW – 90ºW; Figure A)) remains +0.5°C or above for a period of six months or more. Similarly, a La Niña event is recognized when the corresponding figure is −0.5°C or below for the same area/period.

Figure B shows typical SST deviations from the normal during El Niño and La Niña events. The dark red and blue shading seen from the date line to the coast of South America indicates large deviations.

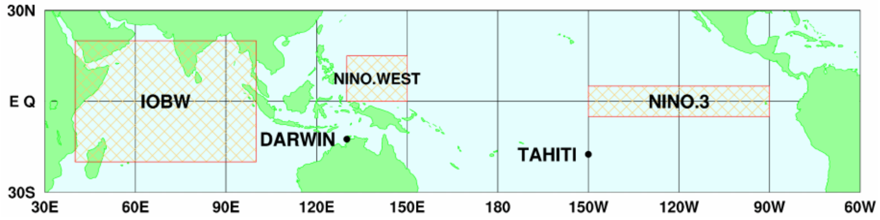

Figure A El Niño monitoring regions

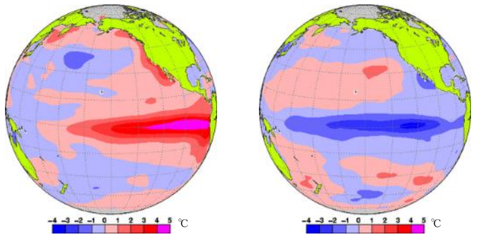

Figure B Left: monthly mean SST anomalies for El Niño (November 1997); right: for La Niña (December 1998)

Red and blue shading represents positive and negative SST deviations, respectively. Darker shading indicates larger deviations. The unit of temperature is degrees Celsius.

Southern Oscillation: El Niño and La Niña events are closely related to trade winds (easterlies blowing around the tropical Pacific), which tend to be weak during the former and strong during the latter. The strength of such winds is closely related to the sea level pressure difference between eastern and western parts of the Pacific. This pressure difference varies in a phenomenon known as the Southern Oscillation. El Niño/La Niña events and the Southern Oscillation are not independent of each other; they are different manifestations of the same phenomenon involving atmospheric and oceanic interaction, and are referred to as ENSO (El Niño – Southern Oscillation) for short.

Pacific Decadal Oscillation (PDO): A phenomenon in which variables in the atmosphere and oceans tend to co-vary with a period of more than ten years in the North Pacific. When sea surface temperatures are lower (higher) than their normals in the central part of the North Pacific, those in its part along the coast of North America are likely to be higher (lower) than their normals, and sea level pressures in the high latitudes of the North Pacific are likely to be lower (higher) than their normals. These atmospheric variations affect meteorological conditions in North America and elsewhere.

Indian Ocean Dipole mode (IOD) event: A phenomenon in which sea surface temperatures (SSTs) are below normal in the south eastern part of tropical Indian Ocean (off the Sumatra Island) and above normal in the western part during the northern hemisphere summer and autumn (June - November). This east-west contrast of SST anomaly pattern is called dipole mode. On the other hand, a phenomenon in which SSTs are above normal off the Sumatra Island and below normal in the western part is called negative IOD event. These phenomena affect the climate near Japan and Australia through the changes of atmospheric circulation caused by atmospheric active (inactive) convections over above (below) normal SST area.

Terms relating to the greenhouse effect

Greenhouse effect: The earth's atmosphere contains small amounts of greenhouse gases, which absorb a large part of the infrared radiation emitted from the earth's surface and re-emit it back, thereby warming the surface. This process is known as the greenhouse effect. Without it, the earth's average surface temperature of around 14°C would be approximately −19°C. Increased concentrations of greenhouse gases enhance the greenhouse effect, thereby producing higher surface temperatures. Major greenhouse gases include carbon dioxide, methane and nitrous oxide. Although water vapor has the strongest greenhouse effect, its main influencing factor is temperature rather than emissions relating to human activity. Water vapor is not usually regarded as a greenhouse gas in the context of global warming because it is considered a feedback factor rather than a forcing factor in climate change.

Carbon dioxide: Of all greenhouse gases, carbon dioxide (CO_2) is the most significant contributor to global warming. Since the start of the industrial era in the mid-18th century, related atmospheric concentrations have increased as a result of emissions associated with human activity such as fossil fuel combustion, cement production and land-use change (e.g., deforestation). Around half of all cumulative anthropogenic CO_2 emissions have remained in the atmosphere. The rest was removed from the atmosphere and stored in natural terrestrial ecosystems and oceans (IPCC, 2021).

Methane: Methane (CH_4) is the second most significant greenhouse gas after CO_2, and has a significant radiative effect around 27.9 times greater than that of CO_2 per unit mass. Around 40% of CH_4 released into the atmosphere is of natural origin (wetlands, termites, etc.), and around 60% is from human-related activity sources (ruminant animals, rice paddy fields, fossil fuel mining, landfill, biomass burning, etc.) (WMO, 2023). CH_4 has a short atmospheric lifetime (approx. 11.8 years) because it is primarily removed from the atmosphere via photochemical reaction with reactive and unstable hydroxyl (OH) radicals.

Nitrous oxide: Nitrous oxide (N_2O) is a significant greenhouse gas because of its large radiative effect per unit mass (about 273 times greater than that of CO_2) and its long lifetime (about 109 years) in the atmosphere. Around 57% of N_2O released into the atmosphere is of natural origin (oceans, soil, etc.), and around 43% is from human activity-related sources (biomass burning, nitrate fertilizers, various industrial processes, etc.) (WMO, 2023). It is photo-dissociated in the stratosphere by ultraviolet radiation.

Halocarbons: Halocarbons are generally carbon compounds containing halogens such as chlorine and bromine, many of which are powerful greenhouse gases whose atmospheric concentrations have increased rapidly since the second half of the 20th century due to artificial production. Although their atmospheric concentrations are only around a millionth those of CO_2, their greenhouse effect per unit mass is several thousand times greater. Chlorofluorocarbons (CFC-11, CFC-12 and CFC-113 among others), carbon tetrachloride, hydrochlorofluorocarbons (HCFCs), 1,1,1-trichloroethane, chloromethane, halons and bromomethane are greenhouse gases and ozone-depleting substances (ODSs). Hydrofluorocarbons (HFC-134a, HFC-152a, etc.) are also included in the definition.

Montreal Protocol: The Montreal Protocol on Substances that Deplete the Ozone Layer (a protocol to the Vienna Convention for the Protection of the Ozone Layer) is an international treaty designed to protect the ozone layer by phasing out the production of numerous substances believed to be responsible for ozone depletion. The treaty was opened for signatures in 1987 and came into force in 1989. Since then, it has undergone several revisions. Japan ratified the protocol in 1988.

ppm, ppb, ppt: In this report, greenhouse gas concentrations are described in terms of mole fractions in units of ppm/ppb/ppt, representing the numbers of molecules of the gas per million/billion/trillion molecules of dry air, respectively.

Terms relating to water masses

North Pacific Subtropical Mode Water (NPSTMW) area: A thermostad between the seasonal and main thermoclines. The NPSTMW area is considered to form in the surface mixed layer just south of the Kuroshio Extension as a result of huge heat loss in winter. It is defined as an area of 16 – 18-degree water at depths of 100 to 400 m at around 20 to 30°N along the 137°E line.

North Pacific Intermediate Water (NPIW) area: The NPIW area forms in the mixed region between the Kuroshio Extension and the Oyashio front. It is defined as water with a salinity level of 34.0 or less at a depth of around 800 m at around 20 to 30°N along the 137°E line.

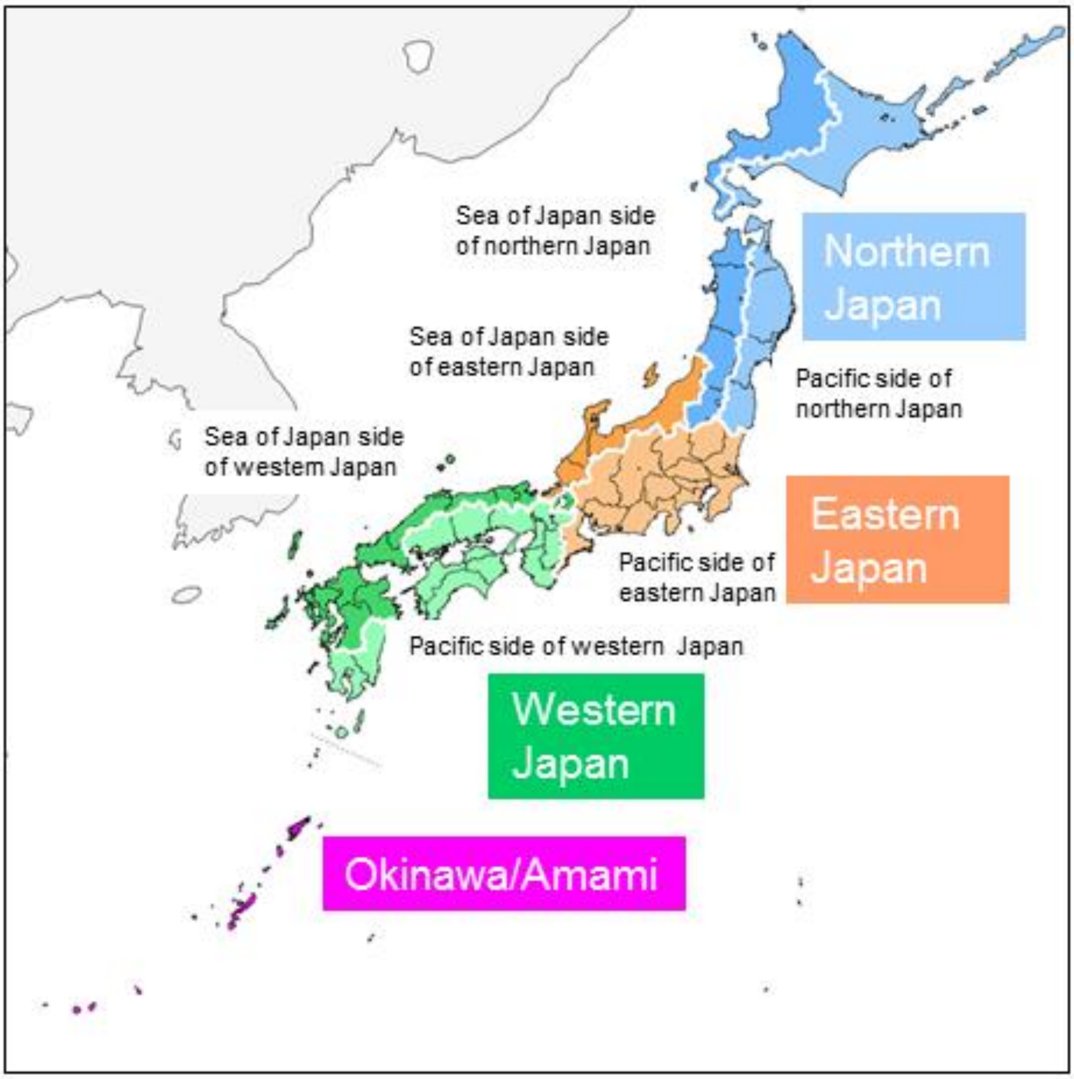

Names of Japanese regions used in this report

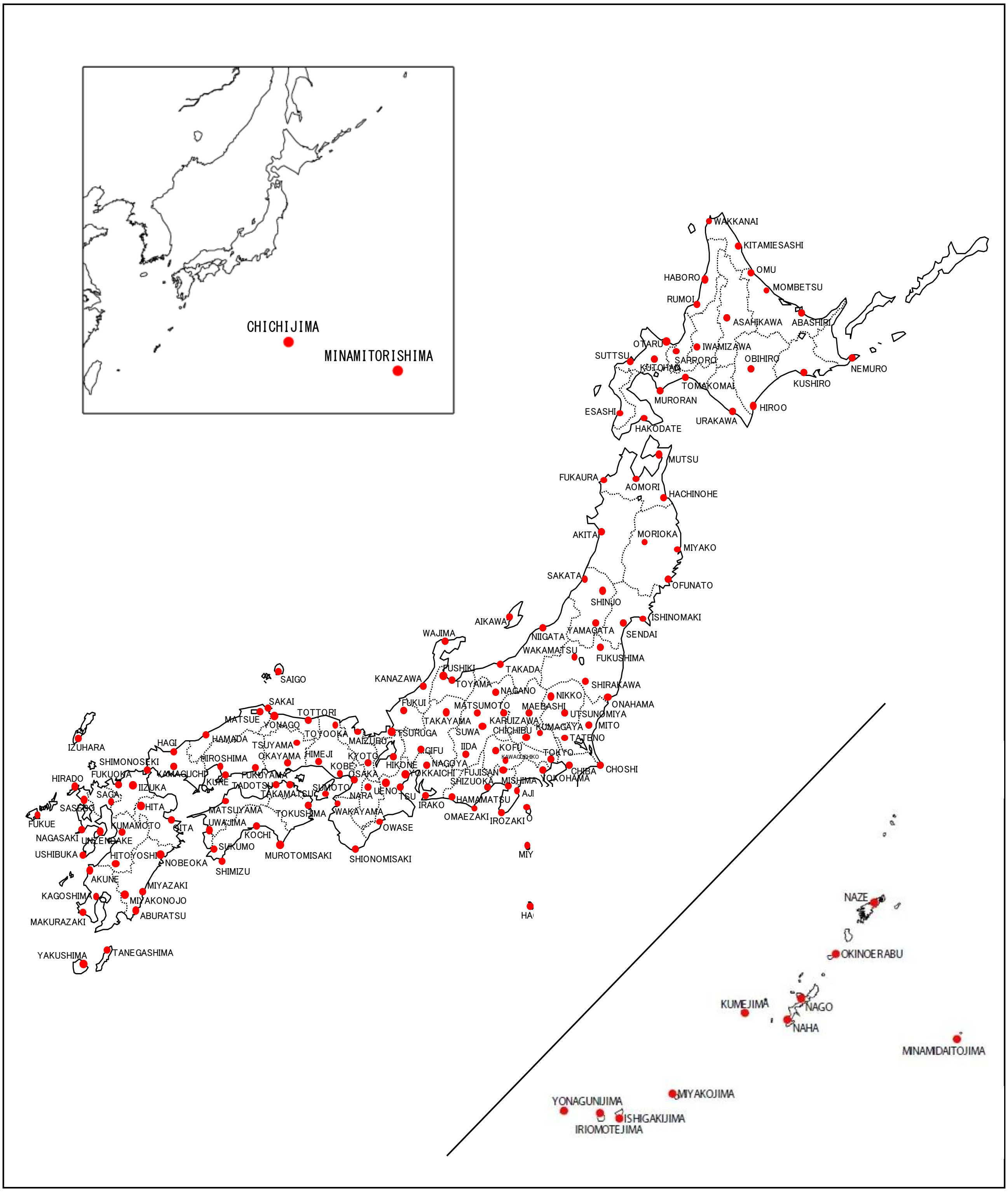

Distribution of surface meteorological observation stations in Japan

References

Chapter 1

EM-DAT: The OFDA/CRED International Disaster, Database – www.emdat.be – Université Catholique de Louvain – Brussels – Belgium

Kosaka, Y., S. Kobayashi, Y. Harada, C. Kobayashi, H. Naoe, K. Yoshimoto, M. Harada, N. Goto,J. Chiba, K. Miyaoka, R. Sekiguchi, M. Deushi, H. Kamahori, T. Nakaegawa; T. Y.Tanaka, T.Tokuhiro, Y. Sato, Y. Matsushita, and K. Onogi, 2024: The JRA 3Q reanalysis. J. Meteor. Soc. Japan, 102, https://doi.org/10.2151/jmsj.2024-004.

Chapter 2

Aono and Saito, 2010: Cherry blossom phenology and temperature reconstructions at Kyoto. http://atmenv.envi.osakafu-u.ac.jp/aono/kyophenotemp4/

Dettinger, M. D. and M. Ghil, 1998: Seasonal and interannual variations of atmospheric CO_2 and climate. Tellus, 50B, 1-24.

Friedlingstein, P., et al., 2023: Global Carbon Budget 2023, Earth Syst. Sci. Data, doi:10.5194/essd-15-5301-2023.

Hirahara, S., M. Ishii and Y. Fukuda, 2014: Centennial-scale sea surface temperature analysis and its uncertainty. J. Climate, 27, 57-75.

Iida, Y., et al., 2021: Global trends of ocean CO_2 sink and ocean acidification: an observation-based reconstruction of surface ocean inorganic carbon variables. J. Oceanogr., doi.org/10.1007/s10872-020-00571-5.

IPCC, 2021: Climate Change 2021: The Physical Science Basis. Contribution of Working Group I to the Sixth Assessment Report of the Intergovernmental Panel on Climate Change [Masson-Delmotte, V., P. Zhai, A. Pirani, S.L. Connors, C. Péan, S. Berger, N. Caud, Y. Chen, L. Goldfarb, M.I. Gomis, M. Huang, K. Leitzell, E. Lonnoy, J.B.R. Matthews, T.K. Maycock, T. Waterfield, O. Yelekçi, R. Yu, and B. Zhou (eds.)]. Cambridge University Press, Cambridge, United Kingdom and New York, NY, USA, 2391 pp. doi:10.1017/9781009157896.

Ishii, M., Y. Fukuda, H. Hirahara, S. Yasui, T. Suzuki, and K. Sato, 2017: Accuracy of Global Upper Ocean Heat Content Estimation Expected from Present Observational Data Sets. SOLA, Vol. 13, 163-167, doi:10.2151/sola.2017-030.

Keeling, C. D., et al., 1995: Interannual extremes in the rate of rise of atmospheric carbon dioxide since 1980. Nature, 375, 666-670.

Keeling, R. F., et al., 1996: Global and hemispheric CO_2 sinks deduced from changes in atmospheric O_2 concentration. Nature, 381, 218-221.

Kudo, R., et al., 2012: Aerosol impact on the brightening in Japan. J. Geophys. Res., 117(D07208), doi:10.1029/2011JD017158.

Le Quéré, C., et al., 2016: Global Carbon Budget 2016, Earth Syst. Sci. Data, 8, 605-649, doi:10.5194/essd-8-605-2016.

Mantua, N. J. and S. R. Hare, 2002: The Pacific Decadal Oscillation. J. Oceanogr., 58, 35−44, doi: 10.1023/A:1015820616384.

Montzka, S. A. et al., 2018: An unexpected and persistent increase in global emissions of ozone-depleting CFC-11, Nature, 557, 413-417, doi:10.1038/s41586-018-0106-2.

Montzka, S. A. et al., 2021: A decline in global CFC-11 emissions during 2018-2019. Nature, 590, 428-432, https://doi.org/10.1038/s41586-021-03260-5.

Niwa, Y., et al., 2014: Seasonal Variations of CO_2, CH_4, N_2O and CO in the Mid-Troposphere over the Western North Pacific Observed Using a C-130H Cargo Aircraft. J. Meteorol. Soc. Japan, 92(1), 50-70, doi:10.2151/jmsj.2014-104.

Norris, J. R., and M. Wild, 2009: Trends in aerosol radiative effects over China and Japan inferred from observed cloud cover, solar ‘‘dimming,’’ and solar ‘‘brightening,’’. J. Geophys. Res., 114(D00D15), doi:10.1029/2008JD011378.

Ohmura, A., 2009: Observed decadal variations in surface solar radiation and their causes. J. Geophys. Res., 114(D00D05), doi: 10.1029/2008JD011290.

Park, S., et al., 2021: A decline in emissions of CFC-11 and related chemicals from eastern China. Nature, 590, 433-437, https://doi.org/10.1038/s41586-021-03277-w.

Rayner, P. J., et al., 1999: Reconstructing the recent carbon cycle from atmospheric CO_2, $\delta^{13}C$ and O_2/N_2 observations. Tellus, 51B, 213-232.

Rigby, M., et al., 2019: Increase in CFC-11 emissions from eastern China based on atmospheric observations, Nature, 569, 546-550, doi:10.1038/s41586-019-1193-4.

Saito, T., et al., 2015: Extraordinary halocarbon emissions initiated by the 2011 Tohoku earthquake. Geophys. Res. Lett., 42, doi:10.1002/2014GL062814.

Sweeney, C., et al., 2015: Seasonal climatology of CO_2 across North America from aircraft measurements in the NOAA/ESRL Global Greenhouse Gas Reference Network, J. Geophys. Res. Atmos., 120, 5155-5190, doi:10.1002/2014JD022591.

Tsuboi, K., et al., 2013: Evaluation of a new JMA aircraft flask sampling system and laboratory trace gas analysis system. Atmos. Meas. Tech., 6, 1257–1270, doi:10.5194/amt-6-1257-2013.

Umezawa, T., et al., 2018: Seasonal evaluation of tropospheric CO_2 over the Asia-Pacific region observed by the CONTRAIL commercial airliner measurements, Atmos. Chem. Phys., 18, 14851-14866, doi:10.5194/acp-18-14851-2018.

WCRP, 2010: Summary Report from the Eleventh Baseline Surface Radiation Network (BSRN) Scientific Review and Workshop. WCRP Informal Report No. 08/2010, 21pp.

Wild, M., 2009: Global dimming and brightening: A review. J. Geophys. Res., 114(D00D16), doi:10.1029/2008JD011470.

Wild, M. and A. Ohmura, 2004: BSRN longwave downward radiation measurements combined with GCMs show promise for greenhouse detection studies. GEWEX news, 14, 4, 20 pp.

WMO, 2009: Technical report of global analysis method for major greenhouse gases by the World Data Center for Greenhouse Gases. GAW Report, 184, WMO/TD, 1473.

WMO, 2018a: Scientific assessment of ozone depletion: 2018. Global Ozone Research and Monitoring Project-Report, 58.

WMO, 2018b: WMO Greenhouse Gas Bulletin, 14.

WMO, 2023: WMO Greenhouse Gas Bulletin, 19. https://library.wmo.int/records/?refine[Serial][]=WMO+Greenhouse+Gas+Bulletin

WMO, 2024: WMO WDCGG DATA SUMMARY, WDCGG No.48, GAW Data Volume IV-Greenhouse Gases and Other Atmospheric Gases, published by the Japan Meteorological Agency in co-operation with World Meteorological Organization. Available at https://gaw.kishou.go.jp/publications/summary. (in preparation)